On the determination of the spatial energy balance of a megacity on the example of Cairo, Egypt

Inauguraldissertation

zur

Erlangung der Würde eines Doktors der Philosophie

vorgelegt der

Philosophisch-Naturwissenschaftlichen Fakultät

der Universität Basel

von

Corinne Myrtha Frey

aus Zürich

Basel, 2010

Genehmigt von der Philosophisch-Naturwissenschaftlichen Fakultät
auf Antrag von

Prof. Dr. Eberhard Parlow und Prof. Dr. rer. nat. Wilfried Endlicher

Basel, den 19.10.2010

Prof. Dr. Martin Spiess

ACKNOWLEDGEMENTS

This thesis would not have been possible without the support of many people. First of all, I am grateful to my supervisor, Prof. Dr. Eberhard Parlow, head of the Institute of Meteorology, Climatology, and Remote Sensing of the University of Basel. His trust in my own scientific abilities, his encouragements in the first phase of the dissertation, when it was very unsure, if the CAPAC field campaign in Cairo could be conducted and his guidance from the initial to the final level enabled me to successfully develop this thesis.

I would like to thank also our system administrator Günter Bing for the good and working EDV infrastructure. His door was always open for any questions and I appreciated his many useful advices in IDL programming.

I am grateful also to Dr. Irene Lehner, who gave valuable support in the writing of the logger programs during the preparation of the field campaign. The campaign would not have been possible without the active support of Dr. Roland Vogt and Hans-Rudolf Rüegg, be it in the preparation phase, the build-up or the dismounting of the stations in Cairo, for which I would like to thank.

Further I am grateful to Prof. Dr. Mohammed Magdy Wahab from the Astronomy Institute of Cairo University. Thanks to his persistence and fast communication, the field campaign in Cairo could be conducted despite of various political and social obstacles in Egypt. I would also like to show my gratitude to Maha Harhash from the same institute, who faithfully assisted me on the field campaign. Our long maintenance car trips in the famous Cairo traffic jams are unforgettable.

It is a pleasure to thank those how supported me in many ways: Dr. Gergely Rigo for enthusiastically introducing me into the field of remote sensing, Mathias Ritter, my roommate, for many discussions covering both scientific and non-scientific topics and all other persons who contributed in any respect during the completion of the project.

I would like to show my gratitude also to the Swiss National Science Foundation, who financed this thesis (grant number 200021-1094 and 200020–120080/1).

This thesis would not have been possible unless many persons gave me their support in private life. My mother Hildegard Limbeck and Lothar Limbeck were always there for me if I was in need of any help or comfort. My father Hans Frey has aroused my interest in nature science.

This thesis would not have been possible without the loving encouragement of my husband Jörg Frey. He motivated me to go on with the work after the birth of our daughter Isabella. His and my mothers' support enabled me to finish the thesis in time.

SUMMARY

This research deals with different aspects of the spatial urban energy balance on the example of the megacity Cairo, Egypt. The energy balance and its single terms were measured in situ during a field campaign in Cairo at three different locations (urban, suburban agricultural and suburban desert) from November 2007 to February 2008. The net radiation and the heat fluxes showed distinct variations between the three stations, representing part of the spatial diversity of the area. The net radiation was highest at the suburban-agricultural location, lowest values were recorded at the suburban-desert station. The urban station ranged in between. The soil heat flux was only measured at the two suburban sites and proved to be highly dependent on the storage term. While the urban and the suburban-desert station had comparable turbulent heat fluxes, the suburban-agricultural station stand out with a low sensible but very high latent heat flux. Cairo acted as a nocturnal heat island - comparing the urban with the two suburban stations. During the day however, the suburban-desert temperatures topped the urban temperatures.

The spatial diversity was also captured using various remote sensing approaches using ASTER satellite data. The strong heterogeneity of the area of interest proved to be the major challenge for the different approaches. The estimation of the net radiation was dependent on a accurate atmospheric correction, which was complicated by the heavy, but spatially varying air pollution over the megacity. The determination of the ground heat flux was done using empirical equations. Some of the used approaches proved to be applicable even in this extreme environment. One promising, as simple approach for the turbulent heat fluxes (S-SEBI: *Simplified Surface Energy Balance Index*) was not usable in the area due to observed high variations in surface temperatures in the desert. Two other approaches (LUMPS: *Local-Scale Urban Meteorological Parameterization Scheme* and ARM: *Aerodynamic Resistance Method*) could be used to deduct turbulent heat fluxes in a satisfactory range. However, the spatial analysis showed, that more research is needed to represent turbulent fluxes in such a heterogeneous area. Besides this, a small study on the estimation of aerodynamic resistance to heat using morphometric methods was conducted. The study showed, that the aerodynamic resistance to heat can be estimated successfully from a digital surface model, knowing surface specific empirical parameters.

Besides the energy balance research, also the CO_2 flux and concentrations were analysed. The CO_2 flux showed a clear weekly dependence on the traffic, but generally fluxes were low considering the strong emissions induced by the old cars and the heavy traffic of Cairo. This result might be due to the spatial distance of the measurement to the streets.

Two in-depth studies about the urban albedo were conducted additionally to the flux research, analysing the dependence of the satellite measured albedo on the sun’s position, atmospheric scattering, housing density and viewing angle.

CONTENTS

LIST OF FIGURES

LIST OF TABLES

1 Introduction

The surface energy budget is an important term in the climatological system with effects on biological, hydrological and geomorphological processes as it determines how the energy received from solar irradiation is distributed to other climatological terms. Areas with a high albedo for example reflect back a high amount of the solar irradiation, following that the available energy for heating the soil and the near-surface air layers or evaporating water from the surface is low. A change of the surface albedo has though a direct impact on the radiative forcing and therefore on the microclimate. Such changes can arise by natural processes or through human impact. The construction of cities is an example for such a human interference in the natural system. Impacts are found from the micro to the global scale. Therefore great importance is laid on the determination of the surface energy budget. ASTER data, featuring a high scale resolution (> 10 m and < 100 m), can give evidence on regional processes, like urban systems.

Megacities came into the focus of recent national and international political and social attention. More than half of the world's population lives now in urban regions and megacities are a consequence of this migration process. Through the increased spatial extent of such urban regions, megacities become relevant for the local and even regional climate (Raga et al. 2001, Tran et al. 2006). The chosen study area of this thesis is the fast growing megacity Cairo in the developing country Egypt. This area can be characterized by its high heterogeneity and strong contrasts in surface cover, ranging from small-scale agricultural farmlands, to the wadi systems in the eastern desert and various urban quarters with different housing density and greening.

Surface radiation and heat fluxes can be measured by various methods, in situ at the ground or remotely by aircraft or from space. Generally in situ measurements are considered more confidential and are therefore taken as reference data for the products of remotely sensed data ('ground truthing'). This procedure is legitimate; especially as many remotely sensed products are obtained by methods calibrated by in situ measurements.

In situ measurements have the advantage of being most accurate as surface energy balance terms generally are measured direct. Moreover, they are mostly not dependent on the influence of the composition of the atmosphere or the occurrence of clouds, as are remote sensing products. When climatological variables are measured, fixed installations are required and thereafter whole time series are produced. These time series can be representative for a broader area, when the surrounding is sufficient homogenous. In case of the eddy covariance technique – a method to measure turbulent exchange - the assumption of certain homogeneity is even a precondition. The disadvantage of in situ measurements however is that the extent of homogeneous surfaces is limited in most applications. Especially in urban areas, the heterogeneity is high and multiple parallel measurements were needed to characterize a bigger city. Other constraints are high costs of installation of the instruments and continuous maintenance of the stations. As the instruments normally need regular cleaning the personal cost of remote stations can be high.

Measurements from aircraft produce spatial data for a single over flight. The financial and planning effort is high and therefore such measurements are normally restricted to Cal/Val campaigns for satellite sensors. Finally, measurements from space produce spatial data and to a certain extent time series in dependence on the sensor's revisit time and scheduling priority policy. The costs for the development, construction and launch of a satellite are immense, but are usually not covered by the end users of the data (scientists, planers), but by the funding of state's space agencies. After launch, only the cost of maintaining the satellite and the running of the ground stations arise. According to the cost policy of the respective space agencies, the charge for the satellite data can vary considerably. NASA has a very user-friendly policy, allowing the scientific community to acquire data for a very low price or sometimes even free of charge without the

need of giving evidence of data use. The main advantage of satellite imagery is the spatial extent of the measurement, allowing the user to calculate parameters for a whole area at once. In return the temporal resolution may be heavily restricted, ranging from 15 minutes for geostationary satellites to unknown scheduled revisit times from commercial very high resolution sensors.

In the last decades a multitude of Earth Observation (EO) satellites were launched by international and national space agencies to assess and monitor numerous geological, hydrological, biological, climatological and even social processes. These sensors offer a wide range of different spectral, spatial and temporal resolutions and their capability is constantly improved. However, the lifetime of a sensor is restricted and continuity is not always guaranteed. The sensor used in this research (ASTER - Advanced Spaceborne Thermal Emission and Reflection Radiometer - , Abrams 2000) has reached its nominal mission lifetime of 6 years already in 2006 and data continuity is not guaranteed. The loss of ASTER will cause great damage to the scientific data user community, as ASTER is unique in the sense of its band combination of VNIR (Visible and Near InfraRed), SWIR (ShortWave InfraRed) and TIR (Thermal InfraRed) bands. The only currently operating satellite with comparable spectral bands is LANDSAT-7 (http://landsat.gsfc.nasa.gov/), whose scan line corrector (SLC) failed already in 2003, resulting in acquisitions only in SLC-off modus. The LANDSAT data continuity mission (http://ldcm.nasa.gov/) unfortunately lacks bands in the thermal region. Future alternatives to ASTER would be the HyspIRI (HYperSPectral InfraRed Imager) mission of NASA or the MISTIGRI (MIcroSatellite for Thermal Infrared GRound surface Imaging) mission of CNES (Centre National d'Etudes Spatiales), which are both still in the study phase (http://hyspiri.jpl.nasa.gov/science, Carcia-Moreno et al. 2009).

ASTER is intended to monitor land surface processes, ranging from volcano and hazard monitoring to vegetation and ecosystem dynamics and hydrological and geological applications. A main intention is also the land surface climatology. It contains the investigation of land surface parameters, like the albedo or the surface temperature, to "understand land-surface interaction and energy and moisture fluxes" (http://asterweb.jpl.nasa.gov/science.asp). Present thesis is placed in this context, working on different methods to estimate the surface energy budget mainly using ASTER data. The different approaches are thereby compared and evaluated on their performance.

The estimation of the surface energy budget is done in this thesis in situ and from space. The in situ data set thereby mainly serves for calibration and validation purposes. It is described in detail in chapter 2.1 ('Flux measurements in Cairo. Part 1: in situ measurements and their applicability for comparison with satellite data '). Chapter 2.2 elaborates on the possibilities of the estimation of the surface energy budget from space, using before mentioned ASTER data ('Flux measurements in Cairo. Part 2: On the determination of the spatial radiation and energy balance using ASTER satellite data'). The in situ data set is used for this research; hence chapter 2.1 is a precondition of chapter 2.2. Chapter 2.3 ('Flux measurements in Cairo. Part 3 - CO_2 fluxes and concentrations (co-authoring)') deals with two additional variables measured during the field campaign - the CO_2 fluxes and concentrations. Chapter 2.4 ('Determination of the aerodynamic resistance to heat using morphometric methods') is a side analysis of chapter 2.2, investigating the estimation of the aerodynamic resistance to heat from a digital surface model. The albedo is a very important term in the net radiation budget and following also in the whole energy budget. Therefore two separate chapters deal only with aspects of the measurement of the albedo in urban areas from space, namely the geometry (chapter 3.1) and the BRF (Bi-directional Reflectance Function) effects (chapter 3.2). The titles of the chapters are 'Geometry effect on the estimation of band reflectance in an urban area' and 'Measurement of multispectral BRF effects of the megacity Cairo, Egypt using CHRIS/PROBA data'.

This thesis follows the scheme of a cumulative dissertation. Chapter 2.1 and 3.1 are accepted publications in peer reviewed journals. Chapter 2.2 and 2.3 are submitted to a peer reviewed journal. Chapter 2.4 is submitted to the peer reviewed e-proceedings of the remote sensing association EARSeL and chapter 3.2 is published as a conference article. Introductory chapters (like this chapter and chapter 2 and 3) shall facilitate the reading of the thesis. In the last part (chapter 4) the whole work is summarized, giving a condensed set of conclusions of the single contributions. The single papers are thereby put into the broader context of the thesis addressed in this introduction. The introductory chapters and chapter 4 are printed single-column, the submitted and accepted papers are printed in two columns.

References

Abrams M. 2000. The Advanced Spaceborne Thermal Emission and Reflection Radiometer (ASTER): Data Products for the High Spatial Resolution Imager on NASA's Terra Platform. *International Journal of Remote Sensing* **21**: 847-859.

Raga GB, Castro T, Baumgardner D. 2001. The impact of megacity pollution on local climate and implications for the regional environment: Mexico City. *Atmospheric Environment* **35(10)**: 1805-1811.

Tran H, Uchihama D, Ochi S, Yasuoka Y. 2006. Assessment with satellite data of the urban heat island effects in Asia mega cities. *International Journal of Applied Earth Observation and Geoinformation* **8(1)**: 34-48.

2 Flux measurements in Cairo

In this chapter, the estimation of the surface energy balance from Cairo shall be presented two-fold. In chapter 2.1, the in situ measurements of the CAPAC (Climate and Air Pollution Analysis of Cairo) campaign at three different stations in Greater Cairo from November 2007 to February 2008 shall be introduced. All climatological variables measured during the campaign, except the CO_2 and PM_{10} measurements, are presented mainly as diurnal ensemble means, but also in other statistical terms for each station. In chapter 2.2 the different remote sensing approaches using ASTER satellite data and their resulting images are described. The images are analyzed firstly with regard to their agreement with the in situ measured data and secondly on their coarse spatial pattern. Chapter 2.3 portrays the CO_2 flux and concentration measurements given as a by-product of the turbulent flux measurements by the eddy covariance system. In this chapter the thesis author is co-authoring only. The PM_{10} measurements were analysed separately in a master thesis (Harhash 2009) and are not part of this thesis. Chapter 2.4 finally presents a study of the aerodynamic resistance to heat estimated using morphometric methods. The aerodynamic resistance is a term used by bulk transfer approaches for calculating the sensible heat flux as described in chapter 2.2. This chapter acts as an extension of chapter 2.2 by deepening the understanding of the bulk transfer approach.

The organization and preparation of the CAPAC field campaign was accompanied by many socio-political constraints. Many visits to Cairo were necessary to fix a collaboration with the two involved organizations 'Cairo University' and 'Egyptian Meteorological Authority' (EMA) by contract. The cooperation with Cairo University went well thanks to the great commitment of Prof. Dr. Mohammed Magdy Wahab. EMA played an ambivalent role, signalizing interest, but on the same time using several delaying tactics. This attitude resulted in a one year delay in the field campaign. Also during the campaign, we faced several country-related problems (corruption cases, inefficient hierarchy systems, several weeks of delay at the Egyptian custom, power failures, and other technical constraints). All these problems complicated the measurements and actually speak for the usefulness of a remote sensing approach, where no or only minimal ground contact is needed.

During the campaign several ASTER scenes were acquired. However, some of them were fully covered by clouds and therefore not usable for this research. Seven scenes acquired at four different dates were finally selected for this research. On three days all three stations were covered by each two scenes. The small data availability allows a direct error diagnostics in the comparison of the satellite images with the in situ data. However, it is not possible to deduct a proper statistics and the comparison remains on the level of a case study.

References

Harhash M. 2009. Origin and characteristics of some dust events in Cairo using Sigma-2 passive samplers. *Master thesis*. Cairo University, Egypt: 99.

2.1 Flux measurements in Cairo. Part 1: in situ measurements and their applicability for comparison with satellite data

Corinne M. Frey, Eberhard Parlow, Roland Vogt, Maha Harhash, Mohammad M. Abdel Wahab

Published in International Journal of Climatology. DOI: 10.1002/joc.2140

ABSTRACT: *Cairo Air Pollution and Climate (CAPAC) is dedicated to the understanding of the urban energy balance in Cairo, Egypt, through measurements from space and at ground stations. The in situ measurements will provide a focussed insight into three carefully chosen microclimates (urban, suburban-agriculture, and suburban-desert) and provide at the same time ground-truth data for satellite image analysis, which will expand the acquired knowledge into the spatial domain. In situ measurements were made during a field campaign in Greater Cairo from November 2007 to February 2008. In this study, the dataset of the CAPAC measurement campaign will be presented and analysed in terms of use for a remote sensing study. Measured variables complied with our expectations. The urban area featured a distinct nocturnal heat island. During the day the choice of reference station was responsible for the magnitude of the heat island. The diurnal cycle of radiative temperature at the suburban-desert station clearly exceeded the one at the urban station, thus the urban setting seemed to have a better heat storage than the suburban-desert. The stations also determined the partitioning of the turbulent heat fluxes. While in Cairo and at the suburban-desert station most of the available energy was partitioned into the sensible heat flux, the suburban-agricultural station maintained a high latent heat flux. The radiation and soil heat flux measurements proved to be applicable for comparison with remotely sensed data. However, the analysis of the turbulent heat fluxes showed that several constraints exist: measured fluxes tend to underestimate the actual flux and directional effects complicate the interpretation. An energy balance closure and footprint modelling is necessary to compare measured fluxes with satellite image retrieved products. Finally, turbulent fluxes are time averages, which is contrary to the remote sensing principle. Consequently, a direct use is problematic.*

2.1.1 Introduction

Placing in situ instruments into an urban environment to measure energy fluxes raises the question of representativeness. Although instruments can be put into the constant flux layer, a measurement finally stands only for the actual source area and can be compared directly only to areas with similar surface characteristics (Oke, 2007). To a lesser extent, the same is true for agricultural or natural areas. The urban surface can be described by different roughness elements like buildings, paved surfaces, their thermal and optical properties, the density of optional vegetation, and bare soil/sand coverage. The common heterogeneity of an urban landscape puts a constraint on the representativeness of in situ measurements carried out at a single place. To overcome this restriction, a multitude of towers would be needed to cover a wider area. This was done by Kanda et al. (2006), using five towers in a densely built-up area in Tokyo, Japan. He found that there is a remarkable spatial variability, especially in the morning sensible heat flux, which was related to the areal fraction of vegetation of the immediate environment of the measurement: a 200-m radius circle around each tower. The highest difference of their ensemble-averaged sensible heat flux was found to be about 50 Wm^{-2} shortly after noon. As their area of interest was still more or less homogeneous, comparing fluxes of different quarters of a city (e.g. comparing a dense with a less dense built–up area) might show an even higher variability. To account for this problem, one might want to use a technique that senses wider areas at the same time, e.g. remote sensing techniques. Using measurements from space, the whole of a megacity can easily be captured at once. However, no direct measurements of most variables of the energy balance are possible by satellite; therefore, there is intensive research into the estimation of the energy budget from space. Most studies have aimed at the investigation of natural or agricultural surfaces (Roerink et al., 2000; Jia et al., 2003; French et al., 2005; Li et al., 2008). However, Rigo and Parlow (2007) have modelled the ground heat flux of an urban area using remote sensing data, and Xu et al. (2008) have derived the whole energy budget for an urban surface using data from a high–resolution sensor mounted on a helicopter. Such methods allow a spatial investigation of fluxes of different urban surfaces, even in comparison with the outer environment. A further advantage is the easy access to remote areas where it is hardly possible to conduct in situ measurements due to geographical, political, or social reasons. Following this idea, we wondered whether it would be possible to derive the terms of the energy budget satisfactorily from remote sensing data over an urban surface of a city with non–optimal political and social conditions, preferably without using *in situ* instrumentation. To control this hypothesis results must be cross–checked with a set of *in situ* data and methods should probably be refined. Therefore, a control city featuring many different microclimates and interesting contrasts had to be selected. Existing algorithms for the derivation of heat fluxes can then be tested for their robustness and general practicability.

The city of Cairo, Egypt, was chosen because of its unique location: Situated in a hot and dry climate and nonetheless partly surrounded by agriculture, a variety of different rural and urban microclimates are evolving. This spatial heterogeneity asks for a process-oriented approach that accounts for the climatic differences in the spatial domain. Further, Cairo is one of the most heavily polluted megacities in the world. The pollution, originating from traffic and industries, is dangerous to human health and has a further impact on the radiation budget.

In the framework of Cairo Air Pollution and Climate (CAPAC), a measurement campaign was conducted from November 2007 to February 2008. At three different stations, all main components of the energy budget were measured continuously additionally to air temperature and humidity. A side aspect of the CAPAC campaign focused on the air pollution of the city. In situ measurements at different locations provided a first understanding of background and street-side concentrations of

coarse and fine particulate matter (PM). Further, very high-resolution CO_2 flux measurements complete the picture. In this paper, the setup of the three stations and the main characteristics of the measured variables (except PM and CO_2 data) will be presented. A short discussion of Cairo as an urban heat island (UHI) will be included. The analysis of PM and CO_2 is beyond the scope of this paper. Inherent to the technique of data capture from remote sensing platforms, satellite images provide top of the atmosphere radiances from a single very short integration time per unit area of the surface. Potential problems arising from the connection of in situ measurements to this kind of data will be discussed in the conclusions section (Chapter 2.1.5). The main conclusions of the whole energy balance study including the remote sensing analysis will appear in a forthcoming paper ('Flux Measurements in Cairo, Part 2'). The results of the CO_2 analysis will also be presented in a follow-up paper ('Flux Measurements in Cairo, Part 3').

2.1.2 Location and setup

Greater Cairo is the largest city in Egypt and on the African continent. Nearly one in five Egyptians lives in Greater Cairo. For centuries Cairo has been a leading city, dominating the social, economic, and political life of the region (Weeks et al., 2005). What is seen from space as one megacity is Greater Cairo, which consists of the governorate of Cairo on the east side of the River Nile, the governorate of Giza that lies along the west bank of the River Nile, and the southern tip of the governorate of Qalyubiyya (also known as the Northern City), which represents the northernmost fringe of Greater Cairo. However, the latter two governorates also incorporate many villages and other free-standing urban settlements (Sutton and Fahmi, 2001).

The city core consists of a densely built-up area, which was already partly developed in the 10th century AD. To the east and west, the city is surrounded by non-arable desert land. Partly to the south along the River Nile but especially to the north in the Nile Delta, prime agricultural land is found. Greater Cairo is a rapidly growing megacity. According to the Central Agency for Population, Mobilization, and Statistics (CAPMAS), Greater Cairo had an estimated population of 17'600'000 in 2006 (Fahmi and Sutton, 2007). Other sources estimate a population of about 20 million inhabitants (Schlink et al., 2007). Around Cairo new towns and settlements are being constructed to relieve the population pressure. The 10th Ramadan on the road to Ismailia is an example of these new towns (Sutton and Fahmi, 2001). A major factor boosting this suburbanization process was the construction of the ring road connecting Cairo's fringes to its centre.

From November 2007 to February 2008, a micrometeorological campaign was conducted in Greater Cairo to measure in situ surface energy fluxes. The purpose of these measurements was to deepen our understanding of the energy budget in a megacity like Cairo, obtain local knowledge of the area, and measure ground-truth data for the remote sensing-based energy balance study of Greater Cairo using Advanced Spaceborne Thermal Emission and Reflection Radiometer (ASTER, http://asterweb.jpl.nasa.gov/) data from NASA. For the duration of the campaign, three stations were maintained: an urban station in the district of Giza, a suburban-agricultural station in the area of Bahteem in the north of Greater Cairo, and a suburban-desert station close to 10th Ramadan City, northeast of the agglomeration of the megacity. Figure 1 shows a LANDSAT RGB composite depicting the locations of the three stations.

The urban station (30°01133.3911N, 31°12127.8111E) was located on the roof of a 15 m building in the campus of Cairo University (http://www.cu.edu.eg/english/), which belongs to the governorate of Giza, west of the River Nile. A 12 m mast was mounted on the roof of the building, which was situated in the most southern part of the campus and was taller than most of the other buildings. This resulted in a total measuring height of 27 m. The campus is a secured area with

massive three- to four-storey buildings, paved roads with cars, squares, footpaths, and planted greens. The campus is partly surrounded by roads with heavy traffic, but in the south and east some extended green areas are found. They consist of a sports ground, botanical testing fields of the university, a zoological garden, and a park. To the west and north of the campus, two areas of shabby blocks of flats separated by narrow alleys are found.

Figure 1 Location of the three stations in Greater Cairo. Background image: RGB-Landsat-7 scene from 11 November 2000. Colours are enhanced for easy visual interpretation.

The suburban-agricultural station (30° 08138.5811N, 31° 15125.2611E) was placed on an alfalfa field inside the meteorological station of Egyptian Meteorological Authority (EMA, http://www.nwp.gov.eg) in Bahteem town, an outskirt in the North of Cairo. Planted fields extended to the east and north of the station. To the south and west of the station, residential areas are found. Bahteem is one of the poorer quarters of Cairo, only a few streets are asphalted, and rubbish scattered around is a major problem. Some small and primitive glass, fertilizer, and ironworks factories are found.

The suburban-desert station (30°14144.0411N, 31°43108.6411E) was situated outside 10th Ramadan City, which was built into the desert. Around the station, which was also a measuring site of EMA, some new asphalt roads, compounds (mostly under construction), newer factories, and a planted green area in the east were found. But mostly the environment consisted of sandy surfaces. Figure 2 shows Google Earth cutouts depicting the surroundings of the three stations.

The purpose of selecting these three stations was to cover the three most dominant landscape features of the region: urban areas, agricultural fields, and desert. Therefore, the sites should be as representative as possible of each feature. However, Cairo is a highly diverse megacity with many different quarters. The extremely dense housing in poor quarters cannot be compared to the planned new cities at the rim of Cairo with their even streets and well kept villas or the spacious quarters of public buildings like the campus of Cairo University. The urban station, therefore, does not represent the whole megacity, but only gives an idea of the selected place, and certainly it can be used for comparison to the remotely sensed data. The same considerations are true for the agricultural station. Farming is mostly done as a family business, so commonly the fields are very small and crops are diversified (El-Khattib et al., 1996).

Beside the scientific demands, the selection of the sites was dominated by security and networking considerations. Egypt is a third world country, and therefore permanent protection of the stations was required. Furthermore, it was necessary to get permission from the authorities for the mounting of the stations. Therefore, the stations were mounted only on restricted sites on governmental ground. Cooperation with the two organizations (Cairo University and EMA) ensured a protected zone for the measurements.

Table I shows the characteristics of the three stations; Table II shows the instruments used and their descriptions.

Table I Station characteristics.

Station	Land use	Measurement height h (m)	Zero-plane displacement height d (m)	Altitude a.s.l. (m)
Cairo University	Urban	27 (temperature: 20)	15.3	22
Bahteem	Suburban-agricultural	1.9	0.1	17
10th Ramadan	Suburban-desert	1.9	0	154

Table II Instrument setup during CAPAC campaign.

Instrument	Instrument's description	Measured parameters	Cairo University	Bahteem	10th Ramadan
CNR1 by Kipp and Zonen	Four-component net radiometer	Shortwave radiation (incoming and outgoing) Longwave radiation (incoming and outgoing) Net radiation	Yes	Yes	Yes
CSAT3 by Campbell	Three-dimensional sonic anemometer	Wind direction and wind speed Sensible heat flux In combination with LI-7500: latent heat flux and CO_2 flux	Yes	Yes	Yes
LI-7500 by Licor	Open path infrared gas analyser	CO_2 and H_2O concentration In combination with LI-7500: latent heat flux and CO_2 flux	Yes	Yes	-
Krypton KH2O	Fast hygrometer	H_2O concentration In combination with LI-7500: latent heat flux	-	-	Yes
Psychrometer	Ventilated temperature measurement	Wet bulb and dry bulb temperature	Yes	Yes	Yes
PTB101b	Barometric pressure sensor	Pressure	Yes	-	-
CM22	Pyranometer	Shortwave radiation (reference)	Yes	-	-
CG4	Pyrgeometer	Longwave radiation (reference)	Yes	-	-
HP3	Soil heat plates	Soil heat flux (each station five pieces)	-	Yes	Yes
Probe 107	Soil thermistors	Soil temperatures (each station five pieces)	-	Yes	Yes
Sigma-2	Deposition by sedimentation on an adhesive foil	Coarse particulate matter (PM_{10}) >2.5 mm (urban three pieces)	Yes	Yes	Yes
MiniVS	Ventilated system sampling the PM2.5 fraction	$PM_{2.5}$	Yes	-	-

(a) **(b)** **(c)**

Figure 2 (a) Cairo University station, (b) Bahteem station, and (c) 10th Ramadan station (Images © 2009 Digital Globe, © 2009 GoogleEarth. View from 2 km height).

2.1.3 Methods

The basic equation for all surface energy balance studies is well known and can be expressed as:

$$Q^* = Q_s + Q_H + Q_{LE} \quad (1)$$

Where Q^* is the net radiation, Q_s is the soil heat flux, Q_H the turbulent sensible heat flux, and Q_{LE} the turbulent latent heat flux. The anthropogenic heat flux is included in the measurement and not listed separately. More recent research has shown that horizontal advection Q_A may play a significant role in the energy budget (Feigenwinter et al., 2008). Q_A should be added to Equation (1), especially as our measurement height is less than twice the building height. Unfortunately, it is not possible to measure this term with a standard eddy covariance tower (Nemitz, 2002; Foken, 2008). Equation (1) therefore assumes zero advection, as was done by Oke et al. (1999), Grimmond and Oke (2002), and Spronken-Smith (2002). In the following, basic equations and correction methods of each of these terms will be explained.

2.1.3.1 Net radiation

Net radiation was determined using the four-component radiometer CNR1 (Table II). Four domes measure separately the shortwave downwelling radiance ($K_{\downarrow}$), the shortwave upwelling radiance ($K_{\uparrow}$), the longwave downwelling radiance ($L_{\downarrow}$), and the longwave upwelling radiance ($L_{\uparrow}$). The net radiation Q^* is:

$$Q^* = K_{\downarrow} + K_{\uparrow} + L_{\downarrow} - L_{\uparrow} \quad (2)$$

The measurement by the two pyrgeometers on the CNR1 includes the thermal emission of the instrument. Therefore, it has to be added to the registered radiance, using the pyrgeometer temperature, which is measured with a Pt-100 inside the CNR1. Calibration constants were determined at the end of the campaign in a comparison experiment. All CNR1 were mounted side by side next to references CM22 and CG4 (Table II), which were calibrated at the World Radiation Centre (WRC) in Davos, Switzerland. The radiation values were stored as 1-min averages.

2.1.3.2 Soil heat flux

The soil heat flux Q_s was measured in two layers using three heat flux plates (HFPs) in the upper layer (5 cm) and two HFPs in a deeper layer (Table II). For the calculation of the energy balance, only the HFPs of the upper layer were used. In addition, thermocouples were buried at 5 cm to measure the soil temperature T_{soil}. Soil heat flux was calculated as:

$$Q_s = f \cdot Q_{s(z)} + Q_{s(0-z)} \quad (3)$$

where $Q_{s(z)}$ is the soil heat flux measured at the depth z, f is the Philips correction factor, and $Q_{s(0-z)}$ is the soil heat storage of the soil layer above z.

$$Q_{s(0-z)} = C_v \frac{dT_{soil}}{dt} \Delta z \quad (4)$$

C_v is the volumetric soil heat capacity ($Jm^{-3}K^{-1}$), which had to be estimated for the respective soils for this study. The used values were 2.5 × 1E6 for Bahteem and 1.5 × 1E6 for the 10th Ramadan station. The factor f of the Philip correction (Philip, 1961) was calculated using the geometrical measurements of the HFPs, as well as the thermal conductivity ($Wm^{-1}K^{-1}$), which also had to be estimated. The used values were 0.5 for Bahteem and 0.7 for the 10th Ramadan station. The constant value at Bahteem leads to a certain mistake, as its water content was not constant due to irrigation (Tsoar, 1990; Abu-Hamdeh and Reeder, 2000). There is some controversy about the Philip correction in the literature (Sauer et al., 2003), but for this analysis it was anticipated that the effect of omitting this correction would exceed the errors induced by the application of the Philip correction. Especially at the desert station, the thermal conductivity of the sand was assumed to differ considerably from the HFP's conductivity.

Using the soil temperatures of 5 cm depths misrepresents the storage heat flux substantially, as the temperature gradient is strongest in the top layers of the soil. In the morning, Q_s therefore showed a time lag behind the solar irradiation, which could be explained by the unaccounted warming of the uppermost layer of the soil. In the afternoon, though, Q_s was overestimated. To account for this, the radiative temperature from the CNR1 was introduced as an additional soil temperature. Therefore, dT_{soil} in equation (4) is a weighted mean of the two temperature differences of both the soil and the radiative temperature. The soil heat flux was also stored as 1-min averages.

2.1.3.3 Turbulent heat fluxes

Turbulent heat fluxes were measured using an eddy covariance system coupling a sonic anemometer (CSAT3) with an open path infrared gas analyser (LI-7500) at both Cairo University and Bahteem (Table II). At 10th Ramadan, a fast hygrometer (KH2O) replaced the open path infrared gas analyser. The measurement rate was 20 Hz. Raw fluxes were then calculated online on a 30- min basis.

Sensible and latent heat fluxes were calculated from:

$$Q_H = \rho_a \, c_p \, \overline{wT} \quad (5)$$

$$Q_{LE} = \rho_a \, \lambda \, \overline{wq} \quad (6)$$

where ρ_a is the density of air, c_p is the specific heat of air, λ is the latent heat of vaporization of water, and w', T', and q' are the fluctuations in vertical velocity, temperature, and water vapour mixing ratio respectively.

For several reasons, it is not possible to measure $\overline{wT}$ and $\overline{wq}$ directly. Therefore a series of four different corrections need to be applied:

The Schotanus correction accounts for the influence of humidity on the sonic temperature T (Kaimal & Gaynor 1991, Oncley et al. 2007, Schotanus et al. 1983). The Schotanus correction was applied automatically online by the CSAT3 for the sonic data of all three stations.

The krypton hygrometer KH2O is a highly sensitive hygrometer that measures rapid fluctuations in atmospheric water vapour using two absorption bands in the ultraviolet region. A correction for the absorption of ultraviolet light by oxygen was necessary (Van Dijk et al. 2003). This correction of the latent heat flux needed to be applied only at 10th Ramadan and was usually very small for the CAPAC campaign (see also Oncley et al. 2007).

Further, the WPL correction (Webb et al. 1980), which compensates for the influence of the fluctuations in temperature and water vapour on the vertical flux of water vapour density, was applied for all three stations.

Eddy covariance systems attenuate the true turbulent signals at very high and low frequencies. Limitations in sensor response, path-length averaging, sensor separation, and signal processing lead to a loss of information. Moore (1986) has presented a set of spectral transfer functions, which are relatively comprehensive. However, they require a priori assumptions about the cospectral shape. In case actual cospectra resemble the assumed one, this approach provides useful correction factors (Massman and Lee, 2002). Although in the meantime some other methods have been presented (Massman and Lee, 2002; Spank and Bernhofer, 2008), in this study the traditional transfer functions of Moore for sensor separation and sensor line-averaging were used. All these corrections are conventional and no further research on new correction methodologies was pursued, as the main interest of this study was to provide background information on the energy balance of Cairo for the subsequent remote sensing investigation.

All measured data were further checked for erroneous values resulting from the regular maintenances, occasional rain events, and insects. A despiking algorithm took care of any other unknown events. Missing values were interpolated according to the following rule: In time-series of 1-minute averages, a maximum of up to 30 continuous missing values were replaced; in 30-minute averages, the number of allowed continuous missing values was 2. This rule left a few periods without valid data; these values were set to a missing value.

The calculation of the ensemble averages in this study includes these missing values. At Cairo University, missing values of the 30-minute averages accounted for 10% of all values. At Bahteem, however, 52% of all values were missing. This high number is mainly because of a high proportion of missing values during the night. Between the hours of 06:00 and 16:30, the percentage is 19 %. At 10th Ramadan, missing values accounted for 23%. Missing values are distributed evenly. It is anticipated that they do not have a significant influence on the findings (excluding nocturnal fluxes at Bahteem).

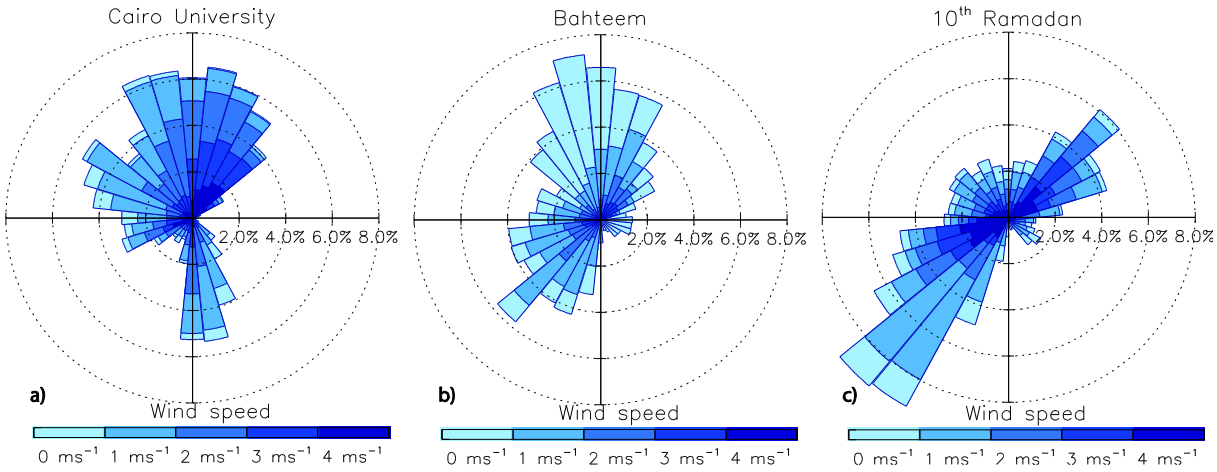

Figure 3 Wind roses for (a) Cairo University, (b) Bahteem, and (c) 10th Ramadan station.

2.1.4 Results

The following gives a brief overview discussing the measured terms of the energy balance one by one. The main focus is on the comparison of the three stations.

2.1.4.1 Wind speed and direction

Both wind speed and direction were recorded as 30-min averages. Wind speed showed a clear diurnal course at all three stations, with high values during the day and low values during the night. The 10th Ramadan showed higher wind speeds than Bahteem during day and night. The maximum ensemble-average wind speeds of the whole duration of the campaign were 4.2 ms^{-1} for 10th Ramadan and 2.6 ms^{-1} for Bahteem. As the measurement was at a higher level at Cairo University than at the other two stations, it is problematic to compare these values. However, the maximum ensemble-average wind speed at Cairo University was 3.6 ms^{-1}. Two dominant directions were observed: a northern and a southern direction, whereas in 10th Ramadan the directions are rather northeast and southwest and in Bahteem they are north and southwest (Figure 3). The southwesterly winds are mainly apparent in winter and spring. They are called 'Khamasin winds' and are often associated with dust storms (Favez et al., 2008). Such a storm occurred from 29 to 30 January 2008, when a maximum wind speed of 10 ms^{-1} was measured. This storm subsequently corrupted the measurements, as the instruments got very dirty. Generally, wind direction did not follow any diurnal course when blowing from the northern sector. However, during 'Khamasin' days, the wind direction followed a clear diurnal pattern with a slight west shift in the later afternoon. Figure 3 shows wind direction and speed for the three stations.

2.1.4.2 Air temperature

Air temperatures showed clear diurnal cycles at all stations and decreased from November until the end of January to rise again in February. The mean temperature at Cairo University during the campaign was 14.9°C, while the maximum ensemble-average temperature was 19.3°C and the minimum ensemble-average temperature was 9.6°C.

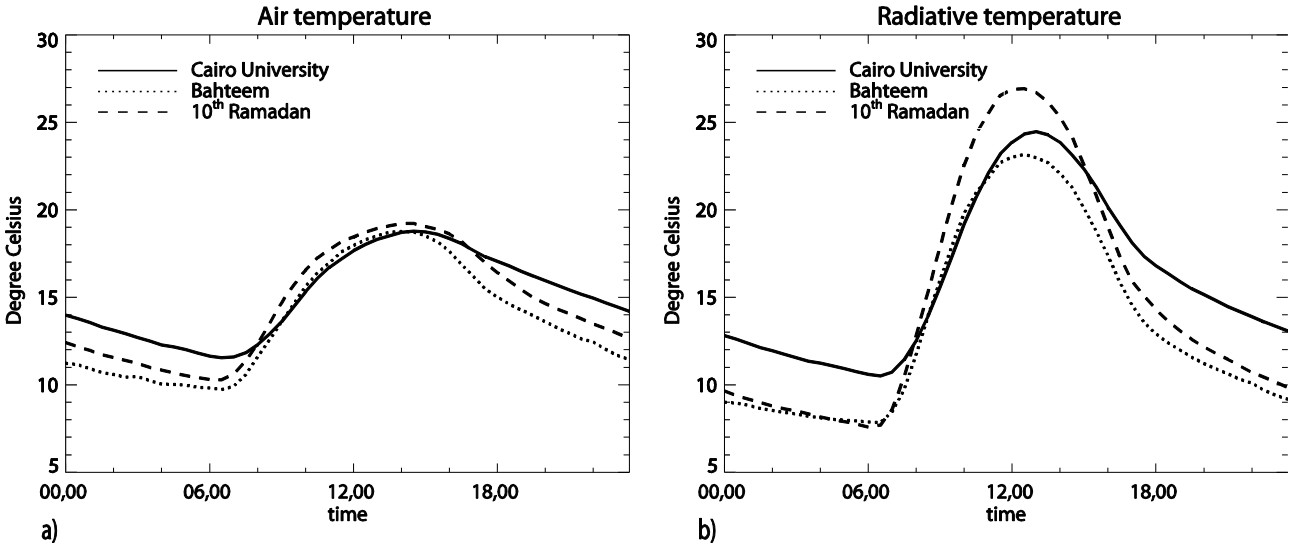

Figure 4 (a) Air temperature and (b) radiative temperature at Cairo University, Bahteem, and 10th Ramadan station: ensemble averages for the period 20 November 2007 - 20 February 2008

The mean maximum temperature (mean of the daily maximum) at Cairo University was 19.2°C, and the mean minimum temperature (mean of the daily minimum) was 10.9°C. These values are characteristic for a hot desert climate (the annual mean temperature is over 18°C and there is only a little precipitation, which mostly falls in the winter months). Cairo features a typical nocturnal heat island, as was found by Robaa (2003). To cancel out the topographic effect on temperature, in the following temperatures were corrected for their height using simply the dry-adiabatic temperature gradient (0.00981 Km^{-1}). This correction, however, did not account for the fact that air temperatures at Cairo University were measured at 20 m (5 m above the roof), while the other two measurements were made at only 1.9 m. According to Kanda et al. (2005), a distinct gradient exists in the street canyon, even if maximum temperatures do not always occur at the same height. For this study, an average deviation of 1 K between the tower measurement and the temperatures at ground was estimated (not included in the data).

An unambiguous heat island study should also include topographic wind effects. However, this would reach beyond the scope of this paper. Figure 4 (a) shows the ensemble-average air temperatures of the three stations.

Air temperatures were higher at Cairo University than in Bahteem and 10th Ramadan during the whole night. The daily mean maximum difference between Cairo University and Bahteem was 5.0°C, and that between Cairo University and 10th Ramadan was 3.2°C (not shown in Figure 4 (a)). These differences, together with Figure 4 (a), document the nocturnal heat island of Cairo. In the morning, urban temperatures did not increase as much as the others; at noon the urban temperatures were lowest. Compared to 10th Ramadan, even a midday cool island seemed to evolve. The subsequent cooling in the evening was strongest in Bahteem, and lowest at Cairo University, which led to the re-evolving nocturnal heat island. The coolest temperatures were found in Bahteem during the night.

UHI studies are conducted using in situ measurements of air temperature (Chow and Roth, 2006; Garcia-Cueto et al., 2007; Parlow, 2007; Gaffin et al., 2008), but also using thermal remote sensing images (Hung et al., 2006; Jusuf et al., 2007; Stathopoulou and Cartalis, 2007; Frey et al., 2007). Figure 4 (a) and (b) shows that the results of these studies should not be compared directly, as air and radiative temperatures vary in behaviour and magnitude. Voogt and Oke (2003) therefore used the terms UHI and surface urban heat island (SUHI) for the respective case. During the night, the difference between the two temperatures is not so obvious. Bahteem and 10th Ramadan cooled to the same radiative temperature, while Cairo University featured considerably higher radiative temperatures (= nocturnal SUHI). However, during the day, Cairo University had higher radiative temperatures than Bahteem, but clearly cooler radiative temperatures than 10th Ramadan.

The strong heating during the day and cooling during the night of the desert surface appears here in contrast to the urban surface, which seemed to store the heat more efficiently in the buildings. A reason for the lower daytime radiative temperatures in Bahteem compared to its relatively higher daytime air temperatures was the wetness of the soil. Before irrigation events, surface temperatures in Bahteem might even exceed those at Cairo University. Nevertheless, after the irrigation, Bahteem's daytime radiative temperatures dropped considerably. Overall, during the day radiative temperatures were higher than the air temperatures, while at night, they were slightly cooler.

The conversion from radiative to brightness temperatures would slightly enhance the differences between Bahteem and the other two stations, due to the lower estimated emissivity of sand and urban construction materials. To quantitatively characterize the UHI of Cairo, mean, mean maximum, and mean minimum differences (MD, MD_{max}, and MD_{min}) as well as standard deviations between Cairo University and the two suburban sites were calculated for day and night

hours from air and radiative temperatures. Day was defined as the time between 06:00 and 17:00 (local time, approximate sunrise to sunset) and night as the time from 17:00 to 06:00.

Table III shows that Cairo functioned as a heat island not only in the night but also during the day, compared to Bahteem station, when averaged over these time intervals. However, 10th Ramadan station was hotter during the day. This result was expected, as 10th Ramadan station is located in the desert, where almost no latent heat flux occurred and most available energy served to heat up the soil and the air. While both the air and radiative temperatures show the same patterns, the magnitudes of the radiative temperatures are much higher. The comparison shows further that the definition of an UHI/SUHI depends considerably on the reference station in the environment (see also Grimmond et al., 1993).

The Cairo nocturnal heat island was not a permanent feature, but depended on the wind situation. Bahteem and 10th Ramadan featured lower air temperatures than Cairo University, particularly when the main wind direction was north-northeast to north-northwest. On such occasions, wind speed was low. On the contrary, Bahteem and sometimes even 10th Ramadan air temperatures might equal Cairo University temperatures, when the strong south to southwest winds were blowing. It seemed that the whole UHI of Cairo was drifting in a north-northeast direction.

Figure 5 shows the air temperatures from the three stations for 3 days along with the wind speeds. Obviously, on the first two nights, temperatures were very similar due to strong winds turning to the south, while on the third night temperatures were much cooler in Bahteem and 10th Ramadan compared with Cairo University, while light northern winds prevailed.

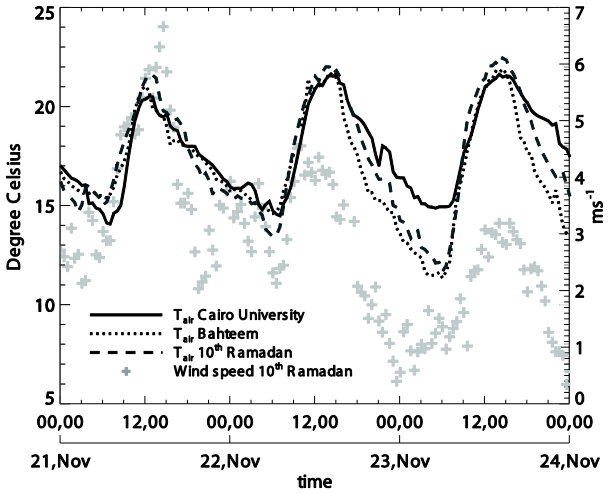

Figure 5 Typical situation of adjusted air temperatures in relation to the wind speed.

Table III Daytime and nocturnal mean differences (MD), mean maximum differences (MD_{max}), and mean minimum differences (MD_{min}) and the standard deviations respectively; air (T_{air}) and radiative temperatures (T_{rad}).

	Cairo University - Bahteem		Cairo University - 10th Ramadan	
	T_{air}	T_{rad}	T_{air}	T_{rad}
Daytime *MD/STDEV*	0.36/1.53	1.31/2.22	-0.35/1.28	-0.99/2.86
Nocturnal *MD/STDEV*	2.35/2.10	3.62/1.84	1.30/1.01	2.97/1.28
Daytime MD_{max}/*STDEV*	3.93/1.97	5.18/1.67	2.59/1.12	4.02/1.33
Nocturnal MD_{max}/*STDEV*	5.00 /1.99	5.26/1.66	3.11/0.97	4.32/0.94
Daytime MD_{min}/*STDEV*	-1.99/1.10	-2.39/1.67	-2.65/1.34	-6.04/2.32
Nocturnal MD_{min}/*STDEV*	0.12/1.55	1.70/1.47	-0.39/0.61	1.05/1.35

2.1.4.3 Radiation fluxes

The measurement of solar radiation $K_{\downarrow}$ indicated a positive gradient in atmospheric transmissivity from the city to the urban fringe and beyond, as was found by Shaltout et al. (2000) and Robaa (2009). At Cairo University, the smallest $K_{\downarrow}$ values were measured, which can be explained by the strong air pollution in Cairo. At Bahteem, $K_{\downarrow}$ was only slightly higher, which might be due to air pollution on one hand and high levels of dispersed dust from the commonly unpaved roads on the other hand. The 10th Ramadan station showed the highest $K_{\downarrow}$ (Figure 6). The ensemble-average difference between $K_{\downarrow}$ from 11:30 to 12:30 at Cairo University and 10th Ramadan station was -62.0 Wm^{-2}, including all weather situations.

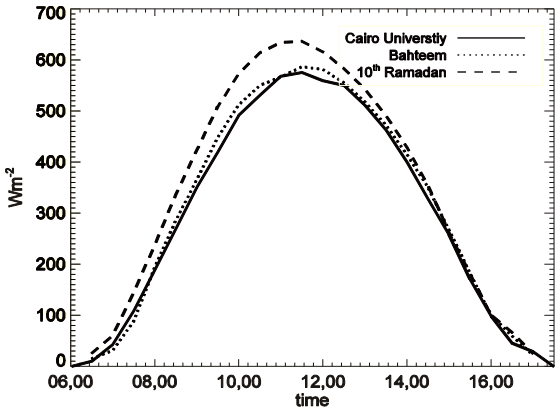

Figure 6 Solar irradiation at the three stations: ensemble averages for the period 20 November 2007 - 20 February 2008.

The difference between Cairo University and Bahteem at the same time of day was only -16.6 Wm^{-2}. Wind direction did not influence these differences. The lower slope of Cairo University and Bahteem in the morning is also noticeable, and might be due to the morning fog in Cairo, which sometimes occurs during the winter months.

Shortwave reflectance is dependent on the albedo α. The albedo was derived using $\alpha = K_{\uparrow}/K_{\downarrow}$ from the times 11:00 to 13:00 only, as the ratios showed the typical bowl shape. The α value was not constant, but altered with time. A first rise in α at Cairo University was due to the clearing activities on the roof at the beginning of the campaign. They ended on 6 December 2007. Further, α was mainly influenced by rain events and by the rate of drying afterwards. The low runaway values of Cairo University and 10th Ramadan coincide with rain events, which were experienced by the first author herself. In the case of Bahteem station, important drops were due to the irrigation events that took place on 20 November 2007, 6 December 2007, 17 January 2008, and 11 February 2008. All of them clearly show up in the data (Figure 7). Apart from these short alterations of α, there was a decreasing trend at Cairo University and 10th Ramadan over the whole period. A reason might be the rising humidity of the ground, as rain events started only in November after the hot and dry summer season, so the ground was extremely dry at the beginning of the measurements. Generally, different sun elevation angles can change measured urban α values (Christen and Vogt, 2004). However, the decreasing trend after the winter solstice does not support this explanation. Another reason might be a changing phenology in the green areas of the campus. Further oscillations, especially at Cairo University, could not be explained.

The longwave downwards radiation $L_{\downarrow}$ showed a similar pattern to the air temperature, and the differences are mainly influenced by the UHI effect. During the day, the differences were very small (<2.5 Wm^{-2} from 11:30 to 12:30); in the night, mean differences were a little higher (<9.2 Wm^{-2} from 20:00 to 06:00). Longwave upward radiation $L_{\uparrow}$ showed similar behaviour to the radiative temperature. Figure 8 shows that Q^* was highest at Bahteem station, where the surface albedo was lowest. Cairo University had only slightly higher values than 10th Ramadan station, which might be due to the albedo. During the night, Cairo University had the lowest Q^*, which was due to the high surface temperatures and consequential high longwave emission. Bahteem and 10th Ramadan were also slightly negative during the night.

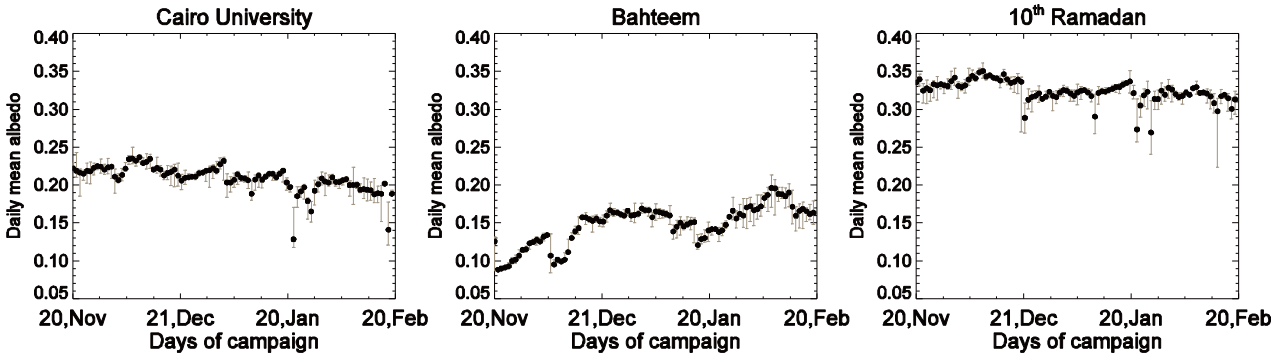

Figure 7 Albedo values at Cairo University, Bahteem, and 10th Ramadan. The black points are the daytime mean values from 11:00 to 13:00; the error bars show the maximum and minimum values measured in the same period.

2.1.4.4 Soil heat flux

The soil heat flux Q_s of Cairo University was not measured directly. Owing to the non-closure of the energy balance at Bahteem and 10th Ramadan (vide infra), it would be error prone if only the residual was used, and therefore it is not shown here. Q_s of 10th Ramadan took a considerable amount of Q^* during the day. From 09:00 to 15:00, it took about 37% of Q^* on average. The maximum of the ensemble average was 158 Wm^{-2} at 10:05. For Bahteem, this relation was smaller: during the same time span, Q_s took about 13% of Q*. The maximum of the ensemble-average was 69 Wm^{-2} at 11:11.

The storage term $Q_{s(0-z)}$ accounted for a considerable part of Q_s . Its average ensemble values peaked at 68 Wm^{-2} in Bahteem at 09:55 and at 117 Wm^{-2} in 10th Ramadan at 10:05, which is 122 and 74% of Q_s, respectively. $Q_{s(0-z)}$ exceeded the original heat flux considerably from morning until early afternoon. Similar magnitudes of the storage term were measured by Ochsner et al. (2007). Omitting the storage term would lead to an extreme underestimation of Q_s at the two stations and further decrease the energy balance closure. In the afternoon, the storage term quickly became negative with a daily minimum and remained negative until the morning. The minimum ensemble-average value of the storage term was -41 Wm^{-2} at 17:08 in Bahteem and -70 Wm^{-2} at 16:29 in 10th Ramadan. $Q_{s(0-z)}$ showed a strong statistical spread, due to the high fluctuations of the surface radiative temperature. Figure 8 shows the ensemble-average Q^* at the three stations and the ensemble-average Q_s at Bahteem and 10th Ramadan for the period 20 November 2007 to 20 February 2008.

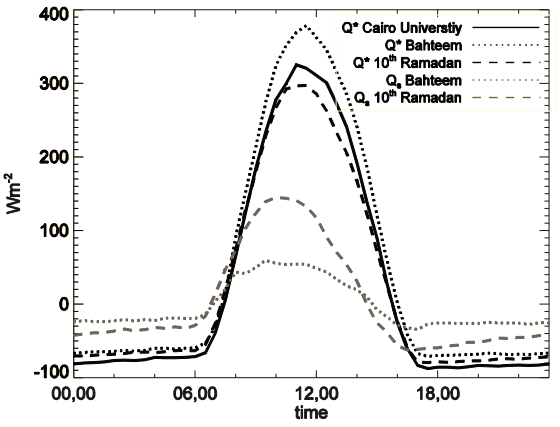

Figure 8 Ensemble-average Q* and Q_s at the three stations for the period 20 November 2007 - 20 February 2008

2.1.4.5 Turbulent fluxes

During the day, unstable conditions (expressed by $z/L < 0$) were the normal case at all three stations, while z is the measurement height and L is the Monin-Obukhov length. On average, daytime z/L was significantly lower at Cairo University than in Bahteem or 10th Ramadan. During the night, stable conditions ($z/L > 0$) prevailed at all three stations.

The turbulent fluxes showed a great variability during the whole campaign. But a common pattern reigns during the whole time: At Cairo University and 10th Ramadan, the available energy was mainly going into Q_H, whereas in Bahteem most energy was fed into Q_{LE}. At 10th Ramadan station, Q_{LE} was generally very low. Still, on some occasions a strong Q_{LE} was recorded. These values were very likely connected with rain events. Unfortunately, no rain data were available, but especially in the second half of the campaign, it was likely that short duration and small-scale rain events occurred, as experienced by the first author. Also at Cairo University, a low average Q_{LE} was found, despite the green areas neighbouring the campus. During the night, the ensemble-average Q_H at Cairo University and 10th Ramadan was slightly negative, while at Bahteem it became clearly negative down to -32 Wm^{-2} shortly after sunset. This strong negative Q_H at Bahteem did not show up every night, but often did so in southwest wind situations with high wind speed. The magnitude was strongly dependent on the latter: the higher the wind speed, the more negative Q_H. However, even during nights with very low wind speeds, Q_H remained mostly slightly negative. Owing to the high percentage of missing values in Bahteem during the night, these findings may not represent the whole duration of the campaign. Nevertheless, Spronken-Smith (2002) found a similar negative Q_H after sunset in winter. The nocturnal negative Q_H at Cairo University is not in agreement with the findings of Oke et al. (1999) and Christen and Vogt (2004), who found a positive nocturnal Q_H in Mexico City, and in Basel, Switzerland. Although heat release is strong during the night at the urban site, it was not enough to maintain a positive Q_H. Figure 9 shows ensemble-average Q_H and Q_{LE} at the three stations.

Q_{LE} in cities is known to be driven by the fraction of vegetation of the surface (Christen and Vogt, 2004; Moriwaki and Kanda, 2004). As all stations show a considerable heterogeneity in the closer environment, it is expected that fluxes show certain directionality.

To control this hypothesis, the surroundings of each station were divided into two sectors. The limiting factor was whether there were vegetated areas or not. The data of each station were then divided into two groups according to the wind direction. The limiting angles of attack for the vegetated sector of each station were as follows (clockwise rotation): Cairo University: 40° – 260°, Bahteem: 270° – 180°, 10th Ramadan: 30° – 190°.

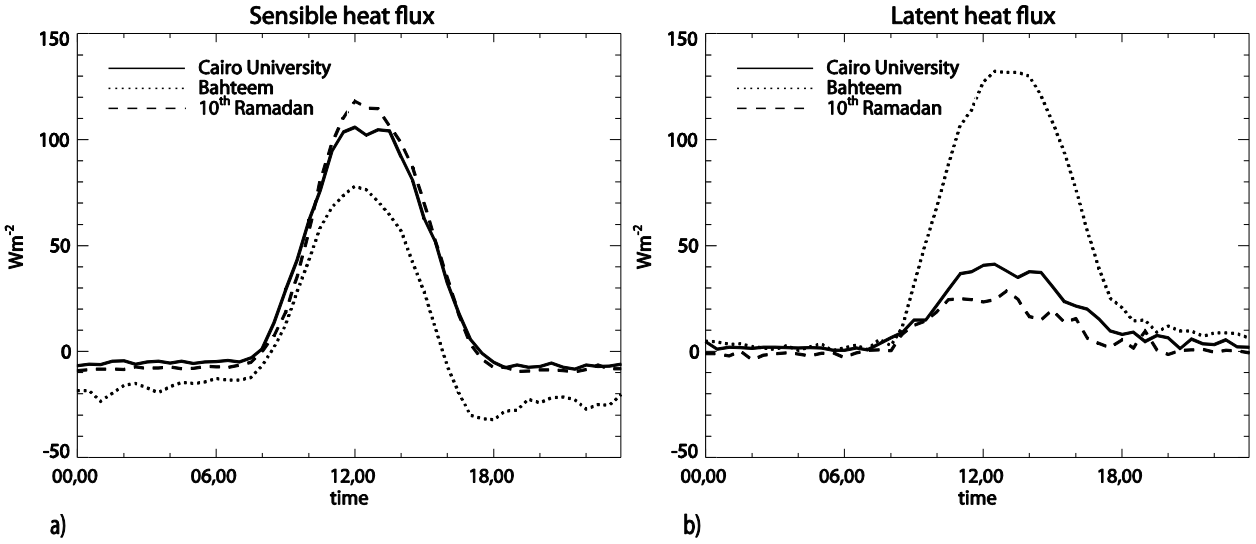

Figure 9 Ensemble-average (a) sensible and (b) latent heat flux at the three stations for the period 20 November 2007 - 20 February 2008 (note: positive fluxes indicate a flux away from the surface, negative values indicate a flux towards the surface).

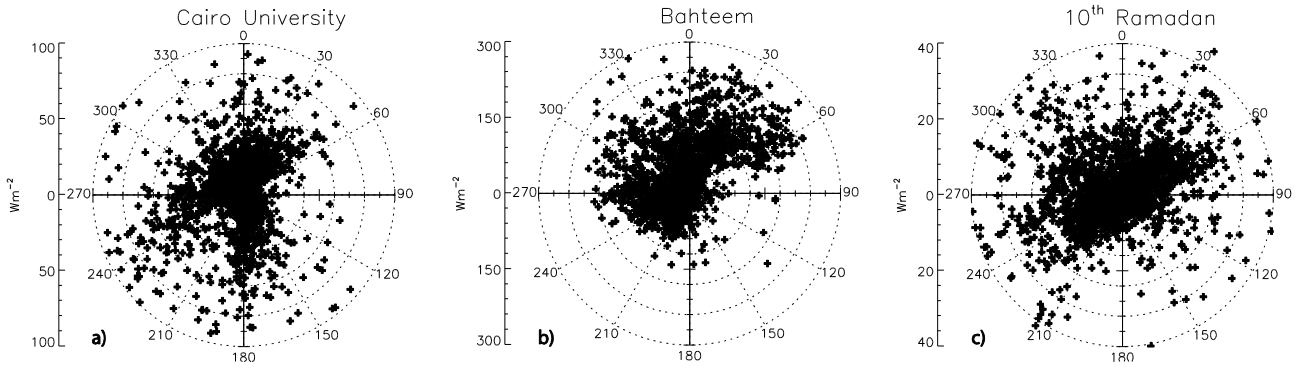

Figure 10 Latent heat flux (Q_{LE}) at (a) Cairo University, (b) Bahteem, and (c) 10th Ramadan stations according to the wind direction. Note that the dimensions of the axes are not equal. Only positive fluxes are given.

Mean daytime (06:00 – 16:30) fluxes were calculated over the whole period. The highest directionality showed Q_{LE} at Bahteem station. Average daytime Q_{LE} was found to be 100.5 Wm^{-2} in the vegetated sector, whereas the non-vegetated sector showed only an average flux of 50.0 Wm^{-2}. The high fluxes came predominantly from the northeastern sector, where winds crossed agricultural fields. Southwesterly winds blew over the suburbs of Bahteem, the non-vegetated sector; consequentially Q_{LE} was low (Figure 10). Q_H did show only a small directional difference. At Cairo University, a small influence of the fields to the south or of the gardens to the east could be detected in Q_{LE}, with a difference of 11.9 Wm^{-2}. But this vegetated sector produced not only a higher Q_{LE} but also a higher Q_H (difference of 16.8 Wm^{-2}). At 10th Ramadan, the tower was located south-west of a small wooden garden belonging to a compound within a distance of 350 m. In the south, a roundabout with irrigated beets was found. Surprisingly, no influence of this planting was found at all in the data. The vegetated sector even showed a lower ensemble-average Q_{LE}. However, the vegetated areas at this location were small and species were mostly xerophilous (Table IV). Q_{LE} in relation to the wind direction is shown in Figure 10.

The Bowen ratio $ß = Q_H/Q_{LE}$ was positive for all three stations during the day. The ß value started to rise in the morning and reached its peak in the afternoon at Cairo University and 10th Ramadan. The maximum ensemble-average ß peaked at ß = 11.0 at 15:00 in 10th Ramadan, while it reached ß = 4.4 at 14:30 in Cairo University. In contrary, in Bahteem a weak peak occurred already in the morning (maximum ensemble-average ß = 0.8) and ß decreased during the day continuously. This disparity could be attributed to the humidity in the air and soil.

Table IV. Mean Q_H and Q_{LE} according to the vegetated and non-vegetated sectors

	Q_H [Wm^{-2}]		Q_{LE} [Wm^{-2}]	
	Vegetated	***Non-vegetated***	***Vegetated***	***Non-vegetated***
Cairo University	65.3	48.5	31.3	19.4
Bahteem	31.3	35.1	100.5	50.0
10th Ramadan	59.1	55.1	12.5	15.7

At Cairo University and 10th Ramadan, only a small latent heat flux was measured. Most available water was evaporated until the afternoon, forcing ß to rise. In Bahteem, the evaporation occurred from the crop during the whole day, so ß did not rise more. Daytime mean Bowen ratios were ß = 1.9 for Cairo University, ß = 0.1 for Bahteem, and ß = 6.7 for 10th Ramadan station (06:00 – 16:30). The ß value showed the same dependence on the wind direction as Q_{LE}. The ß values found in this study are comparable to values in the literature. Spronken-Smith (2002) found summer daytime ß for Christchurch from 1.29 to 2.11. Moriwaki and Kanda (2004) found daytime ß of a residential area in Tokio in the range of 1.29 – 5.0, depending on the season. Christen and Vogt (2004) found daytime urban ß close to ß = 2, and Grimmond and Oke (1995) reported daytime values of ß = 0.78 – 1.83 in four US cities, with a clear gradient of the water availability in the city. Oke et al. (1999) found the Bowen ratios of Mexico city to be between ß = 4 and 12, which is more similar to our desert conditions.

The Bowen ratios at Cairo University and 10th Ramadan showed a considerable statistical spread. The daytime mean standard deviations of the ensemble averages were 14.7 for Cairo University and 23.1 for 10th Ramadan. In Bahteem, this value was 4.9. Grimmond et al. (1993) found daytime ß to be more constant at rural sites than at urban sites. This observation can be confirmed only for Bahteem and Cairo University. The 10th Ramadan, also a rural site (albeit desert), showed an even higher diversity than Cairo University.

2.1.4.6 Energy balance closure

At Cairo University, the soil heat flux was not measured, so no closure could be determined. At Bahteem and 10th Ramadan, the energy balance was not closed. While the residual was slightly negative during the night, it reached considerable dimensions during the day, especially in Bahteem, where the maximum of the ensemble-average residuum was 148 Wm^{-2}, which is 45% of Q^* at that time. At 10th Ramadan, the maximum ensemble-average residuum was 57 Wm^{-2}, which is 20% of Q*. Figure 11 shows the ensemble-average residual at Bahteem and 10th Ramadan. No final explanation for these high residuals could be found. According to Foken (2008), measuring errors of the terms of the energy balance, including storage terms, do not explain such big daytime residuals if measurements are done carefully. As a result of the EBEX campaign, Oncley et al. (2007) found advection to be a major reason for afternoon residuals, which are assumed to be zero in Equation (1). Foken (2008) goes further and assumes that the closure problem is generally a scale problem, as the eddy covariance measurements only include the turbulent exchange of smaller eddies. But larger eddies seem to have a major influence on exchange processes in a heterogeneous landscape. So a closure is only possible on a landscape scale. However, fluxes in a totally uniform landscape, like a desert or a uniform bush land, should not be influenced by larger eddies. This hypothesis is partly supported by the data of 10th Ramadan, where the residual is lower than that of Bahteem. But as Figure 1 shows, 10th Ramadan is also homogeneous, but in the microscale. The outer surroundings include several buildings, factories, some trees, and street lamps. Further, the residual shows directionality. When north-easterly winds prevail in Bahteem, the residual is considerably smaller than in south-western wind situations. The daytime (06:00–16:30) mean ensemble-average residual for the vegetated sector (see Chapter 2.1.3.3) of Bahteem is 40.4 Wm^{-2}; for the non-vegetated sector it is double: 91.3 Wm^{-2}. This can be explained by the higher heterogeneity farther into the south-western sector, where the surface is mainly urban. The 10th Ramadan station also shows a slight directionality, but here the difference between the two daytime means is only 10.5 Wm^{-2}, with the non-vegetated sector (open desert) having the lower residual.

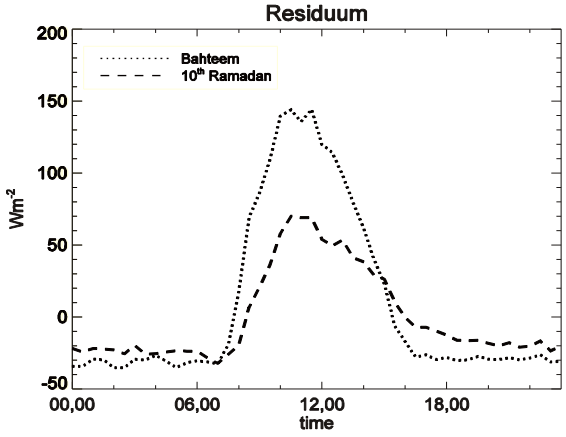

Figure 11 Ensemble-average energy balance residual at the two stations for the period 20 November 2007 – 20 February 2008.

2.1.5 Conclusions

In the framework of CAPAC, a micrometeorological field campaign was conducted in Greater Cairo from November 2007 to February 2008. All key variables of the energy balance were measured using standard eddy covariance instrumentation in three typical microclimates: an urban, a suburban-agricultural, and a suburban-desert station. The terms of the energy balance will be compared to the output of a remote sensing study. Hence, following the results of this study will be related to some aspects of remote sensing.

Cairo features a nocturnal heat island with higher air and radiative surface temperatures in the city than in the suburban stations. In south to southwest wind situations when wind speed was high, the nocturnal differences disappeared; the UHI seemed to be shifted to north. The results also highlight the fact that findings from radiative temperatures, as used in remote sensing studies, differ significantly from findings from studies using air temperature. The urban setting better stored heat than the suburban-desert soil. This was expressed by the lower magnitude of the diurnal cycle of radiative temperature at the urban station compared with the suburban-desert station.

Net radiation of the suburban-agricultural station was highest, while the suburban-desert station had the lowest values. The main factor determining these differences was the surface albedo. The latter variable was not constant over time, but changed due to several reasons. Therefore, it is suggested that surface albedo should be updated regularly when doing remote sensing studies of the area. Daytime irradiation showed a gradient away from the city, most probably due to air pollution. It follows that the atmospheric properties change over space significantly. So, a single radiosonde ascent is not sufficient to accurately describe the composition of the atmosphere in such an environment. This fact must be considered when modelling, for example, solar irradiation in the spatial domain for remote sensing studies. Longwave incident radiation did show nocturnal differences due to the urban heat island. However, the magnitude of these differences was fairly small (<9.2 Wm^{-2}) which falls into the measurement accuracy. All terms of the net radiation could be determined with sufficient accuracy and can be directly used for the comparison study with remote sensing or modelled data, whereas scaling issues of the respective pixels must be accounted for. The findings for the soil heat flux were similar. The soil heat flux was estimated using two terms: the soil heat flux at depth z and the heat storage above z. The storage term proved to be a major contributor and omitting it would lead to a considerable underestimation of the soil heat flux. However, the storage term also showed extreme short-term fluctuations originating from rapid radiative surface temperature changes. Thus, the radiative temperatures of a satellite image might depict a condition, which is not necessarily representative of a longer period (e.g. 30 min).

The analysis of the turbulent heat fluxes showed that at the urban and the suburban-desert station the main part of the available energy was going into the sensible heat flux, while at the suburban-agricultural station the latent heat flux was

dominating. Several constraints were found in using the in situ measured turbulent flux data for the remote sensing analysis. The lack of a correct determination of the turbulent heat fluxes with a sufficient closure limits the applicability of these data to comparison studies with remote sensing data. The influence of large-scale eddies is as yet unsolved and puts a major restriction on the use of these data. As stated earlier, the purpose of these measurements was to measure ground-truth data for a remote sensing-based energy balance study. The non-closure of the energy balance and a very probable underestimation of the turbulent fluxes limit the direct usage of the in situ flux data for input in models later applied to remote sensing data. A simple redistribution of the residual to the sensible and latent heat flux according to the Bowen ratio (Twine et al., 2000) is a first approach, but remains problematic, as the ratio might be different for large eddies (Foken, 2008).

Important for the comparison with remote sensing data is the directionality found in the flux data. As turbulent fluxes were strongly influenced by their source area, especially in Bahteem, it is straightforward to define this source area in the remote sensing image for further flux comparison (Li et al., 2008). This of course assumes knowledge of the wind speed and direction. So, wind speed and direction are indispensable variables in heterogeneous surfaces.

The high daytime temporal variation of the partition of the turbulent fluxes does not allow a methodology to be applied that uses a constant Bowen ratio or equivalent. This is another major restriction, as the Bowen ratio would allow only one turbulent heat flux to be determined.

Finally, fluxes measured with the eddy covariance technique are always time averages, in our case 30-minute averages, while remote sensing images are observations done in a very short time frame. The in situ measured fluxes are affected by changes in surface variables like surface temperature during the averaging period. However, the use of remote sensing images will not incorporate these changes.

A sound methodology for comparing fluxes retrieved from satellite images with in situ measured fluxes incorporating all these constraints is outstanding and the subject of ongoing research.

2.1.6 Acknowledgements

This work was supported by the Swiss National Science Foundation (grant number 200021-1094).

2.1.7 References

Abu-Hamdeh NH, Reeder RC. 2000. Soil thermal conductivity. Effects of density, moisture, salt concentration, and organic matter. *Soil Science Society of America Journal* **64**: 1285–1290.

Chow WTL, Roth M. 2006. Temporal dynamics of the urban heat island of Singapore. *International Journal of Climatology* **26**: 2243–2260.

Christen A, Vogt R. 2004. Energy and radiation balance of a central European city. *International Journal of Climatology* **24**: 1395–1421.

El-Khattib HM, El-Mowelhi NM, Hawela F. 1996. Monitoring land cover of the desert fringes of the eastern Nile Delta, Egypt. *Geoscience and Remote Sensing Symposium, 1996 (IGARSS '96). Remote Sensing for a Sustainable Future* **3**: 1756–1758.

Fahmi W, Sutton K. 2007. Greater Cairo's housing crisis: contested spaces from inner city areas to new communities. *Cities* **25**: 277–297.

Favez O, Cachier H, Sciare J, Alfaro SC, El-Araby TM, Harhash MA, Abdelwahab MM. 2008. Seasonality of major aerosol species and their transformations in Cairo megacity. *Atmospheric Environment* **42**: 1502–1516.

Feigenwinter C, Bernhofer C, Eichelmann U, Heinesch B, Hertel M, Janous D, Kolle O, Lagergren F, Lindroth A, Minerbi S, Moderow U, Mölder M, Montagnani L, Queck R, Rebmann C, Vestin P, Yernaux M, Zeri M, Ziegler W, Aubinet M. 2008. Comparison of horizontal and vertical advective CO_2 fluxes at three forest sites. *Agricultural and Forest Meteorology* **148**: 12–24.

Foken T. 2008. The energy balance closure problem: an overview. *Ecological Applications* **18**: 1351–1367.

French AN, Jacob F, Anderson MC, Kustas WP, Timmermans W, Gieske A, Su Z, McCabe MF, Li F, Prueger J, Brunsell N.

2005. Surface energy fluxes with the advanced spaceborne thermal emission and reflection radiometer (ASTER) at the Iowa 2002 SMACEX site (USA). *Remote Sensing of Environment* **99**: 55–65.

Frey C, Rigo G, Parlow E. 2007. Urban radiation balance of two coastal cities in a hot and dry environment. *International Journal of Remote Sensing* **28**: 2695–2712.

Gaffin SR, Rosenzweig C, Khanbilvardi R, Parshall L, Mahani S, Glickman H, Goldberg R, Blake R, Slosberg RB, Hillel D. 2008. Variations in New York city's urban heat island strength over time and space. *Theoretical and Applied Climatology* **94**: 1–11.

Garcia-Cueto OR, Jauregui-Ostos E, Toudert D, Tejeda-Martinez A. 2007. Detection of the urban heat island in Mexicali, B.C., Mexico and its relationship with land use. *Atmosfera* **20**: 111–131.

Grimmond CSB, Oke TR. 1995. Comparison of heat fluxes from summertime observations in the suburbs of four North American cities. *Journal of Applied Meteorology* **34**: 873–889.

Grimmond CSB, Oke TR 2002. Turbulent heat fluxes in urban areas: observations and a local–scale urban meteorological parameterization scheme (LUMPS). *Journal of Applied Meteorology* **41**: 792–810.

Grimmond CSB, Oke TR, Cleugh HA. 1993. "The role of "rural" in comparisons of observed suburban-rural flux differences", *International Association of Scientific Hydrology* **212**, 165–174.

Hung T, Uchihama D, Ochi S, Yasuoka Y. 2006. Assessment with satellite data of the urban heat island effects in Asian mega cities. *International Journal of Applied Earth Observation and Geoinformation* **8**: 34–48.

Jia L, Su Z, van den Hurk B, Menenti M, Moene AF, de Bruin HAR, Baselga Yrisarry JJ, Ibanez M, Cuesta A. 2003. Estimation of sensible heat flux using the Surface Energy Balance System (SEBS) and ATSR measurements. *Physics and Chemistry of the Earth* **28**: 75–88.

Jusuf SK, Wong NH, Hagen E, Anggoro R, Hong Y. 2007. The influence of land use on the urban heat island in Singapore. *Habitat International* **31**: 232–242.

Kaimal JC, Gaynor JE. 1991. Another look at sonic thermometry. *Boundary-Layer Meteorology* **56**: 401–410.

Kanda M, Moriwaki R, Kimoto Y. 2005. Temperature profiles within and above an urban canopy. *Boundary-Layer Meteorology* **115**: 499–506.

Kanda M, Moriwaki R, Kasamatsu F. 2006. Spatial variability of both turbulent fluxes and temperature profiles in an urban roughness layer. *Boundary-Layer Meteorology* **121**: 339–350.

Li F, Kustas WP, Anderson MC, Prueger JH, Scott RL. 2008. Effect of remote sensing spatial resolution on interpreting tower-based flux observations. *Remote Sensing of Environment* **112**: 337–349.

Massman WJ, Lee X. 2002. Eddy covariance flux corrections and uncertainties in long-term studies of carbon and energy exchanges. *Agricultural and Forest Meteorology* **113**: 121–144.

Moore CJ. 1986. Frequency response corrections for eddy correlation systems. *Boundary-Layer Meteorology* **37**: 17–35.

Moriwaki R, Kanda M. 2004. Seasonal and diurnal fluxes of radiation, heat, water vapor, and carbon dioxide over a suburban area. *Journal of Applied Meteorology* **43**: 1700–1710.

Nemitz E, Hargreaves KJ, McDonald AG, Dorsey JR, Fowler D. 2002. Micrometeorological measurements of the urban heat budget and CO_2 emissions on a city scale. *Environmental Science & Technology* **36**: 3139–3146.

Ochsner TE, Sauer TJ, Horton R. 2007. Soil heat storage measurements in energy balance studies. *Agronomy Journal* **99**: 311–319.

Oke TR. 2007. Siting and exposure of meteorological instruments at urban sites. In Borrego C, Norman A-L (eds). *Air Pollution Modeling and its Application XVII,* Springer: New York, USA; 615–632.

Oke TR, Spronken-Smith RA, Jauregui E, Grimmond CSB. 1999. The energy balance of central Mexico City during the dry season. *Atmospheric Environment* **33**: 3919–3930.

Oncley SP, Foken T, Vogt R, Kohsiek W, de Bruin H, Bernhofer C, Christen A, Grantz D, Lehner E, Liebethal C, Liu HP, Mauder M, Pitacco A, Ribeiro L, Weidinger T. 2007. The energy balance experiment EBEX-2000. Part I: overview and energy balance. *Boundary-Layer Meteorology* **123**: 1–28.

Parlow E. 2007. Stadtklima. In Gebhardt H, Glaser R, Radtke U, Reuber P (eds). *Geographie. Physische Geographie und Humangeographie*, Elsevier Publishers: München; 56–60.

Philip JR. 1961. The theory of heat flux meters. *Journal of Geophysical Research* **66**: 571–579.

Rigo G, Parlow E. 2007. Modelling the ground heat flux of an urban area using remote sensing data. *Theoretical and Applied Climatology* **90**: 185–199.

Robaa SM. 2003. Urban-suburban/rural differences over Greater Cairo, Egypt. *Atmosfera* **16**: 157–171.

Robaa SM. 2009. Urban-rural solar radiation loss in the atmosphere of Greater Cairo region, Egypt. *Energy Conversion and Management* **50**: 194–202.

Roerink GJ, Su Z, Menenti M. 2000. S-SEBI: a simple remote sensing algorithm to estimate the surface energy balance. *Physics and Chemistry of the Earth (B)* **25**: 147–157.

Sauer TJ, Meek DW, Ochsner TE, Harris AR, Horton R. 2003. Errors in heat flux measurement by flux plates of contrasting design and thermal conductivity. *Vadose Zone Journal* **2**: 580–588.

Schlink U, Rehwagen M, Richter M, Herbarth O. 2007. Environmental security in urban areas. Health-relevant VOC exposure in the Greater Cairo Area, Egypt. In Linkov I, Wenning RJ, Kiker GA (eds). *Managing Critical Infrastructure Risks: Decision Tools and Applications for Port Security*, Springer: Dordrecht, 423–434.

Schotanus P, Nieuwstadt FTM, De Bruin HAR. 1983. Temperature measurement with a sonic anemometer and its application to heat and moisture fluctuations. Boundary-*Layer Meteorology* **26**: 81–93.

Shaltout MAM, Tadros MTY, El-Metwally M. 2000. Studying the extinction coefficient due to aerosol particles at different spectral bands in some regions at great Cairo. *Renewable Energy* **19**: 597–615.

Spank U, Bernhofer C. 2008. Another simple method of spectral correction to obtain robust eddy-covariance results. *Boundary-Layer Meteorology* **128**: 403–422.

Spronken-Smith RA. 2002. Comparison of summer- and winter-time suburban energy fluxes in Christchurch, New Zealand. *International Journal of Climatology* **22**: 979–992.

Stathopoulou M, Cartalis C. 2007. Daytime urban heat islands from Landsat ETM+ and Corine land cover data: an application to major cities in Greece. *Solar Energy* **81**: 358–368.

Sutton K, Fahmi W. 2001. Cairo's urban growth and strategic master plans in the light of Egypt's 1996 population census results. *Cities* **18**: 135–149.

Tsoar H. 1990. The ecological background, deterioration and reclamation of desert dune sand. *Agriculture, Ecosystems and Environment* **33**: 147–170.

Twine TE, Kustas WP, Norman JM, Cook DR, Houser PR, Meyers TP, Prueger JH, Starks PJ, Wesely ML. 2000. Correcting eddy-covariance flux underestimates over a grassland. *Agricultural and Forest Meteorology* **103**: 279–300.

Van Dijk A, Kohsiek W, de Bruin HAR. 2003. Oxygen sensitivity of krypton and Lyman-a hygrometers. *Journal of Atmospheric and Oceanic Technology* **20**: 143–151.

Voogt JA, Oke TR. 2003. Thermal remote sensing of urban areas. *Remote Sensing of Environment* **86**: 370–384.

Webb EK, Pearman GI, Leuning R. 1980. Correction of flux measurements for density effects due to heat and water vapour transfer. *Quarterly Journal of Royal Meteorological Society* **106**: 85–100.

Weeks JR, Larson D, Fugate D. 2005. Patterns of land use as assessed by satellite imagery: an application to Cairo, Egypt. In Entwisle B, Rindfuss R, Stern P (eds). *Population, Land Use, Environment: Research Directions*, National Academy Press: Washington, DC.

Xu W, Wooster MJ, Grimmond CSB. 2008. Modelling of urban sensible heat flux at multiple scales: a demonstration using airborne hyperspectral imagery of Shanghai and a temperature-emissivity separation approach. *Remote Sensing of Environment* **112**: 3493-3510.

2.2 Flux measurements in Cairo. Part 2: On the determination of the spatial radiation and energy balance using ASTER satellite data

Corinne M. Frey, Eberhard Parlow

Submitted to International Journal of Climatology

ABSTRACT: *The determination of the spatial energy budget using remote sensing images is a practicable approach, especially in areas, where in situ measurements are rare or not available at all. This study highlights the possibilities and constraints of determining spatial surface radiation and land heat fluxes in a heterogeneous urban area and its agricultural and natural surroundings. Net radiation was determined using ASTER satellite data and MODTRAN radiative transfer calculations. The soil heat flux was estimated with several empirical methods using various radiative terms and vegetation indices. The turbulent heat fluxes finally were determined threefold with the LUMPS (Local-Scale Urban Meteorological Parameterization Scheme), the ARM (Aerodynamic Resistance Method) and the S-SEBI (Simplified Surface Energy Balance Index) method. The performance of the atmospheric correction was found to be crucial for the estimation of the radiation balance and thereafter the heat fluxes. The soil heat flux could be modelled satisfactorily with three of the applied approaches. The other approaches failed in producing acceptable soil heat fluxes. The LUMPS method for the turbulent fluxes, appeals by its simplicity. However, a correct spatial estimation of associated parameters is not yet solved. The ARM method delivered the best results for the turbulent fluxes, considering not only the comparison with measurement data but also the spatial distribution in the images. The S-SEBI approach finally proved to be unusable due to a high variability of surface temperatures in the desert.*

2.2.1 Introduction

In the last decade many studies tried to estimate land surface fluxes from remote sensing images. The motivation for such work is to overcome the problem of spatial representativeness of single in situ measurements in an area or to by-pass the lack of available measurements at all. A successful methodology would be extremely helpful for example for the determination of surface energy fluxes from remote areas, where it is difficult or even impossible to set up in situ measurements because of geographical, political, infrastructural, or social reasons as well.

The goal of this study was to show, if it is possible to determine the whole energy budget from ASTER satellite images for single dates of a remote area featuring very contrasting surface covers; using as few in situ measurements as possible. For this a megacity was selected, consisting of many different quarters and located in a natural environment with a variety of different landscapes.

From literature, three groups of methods for the estimation of turbulent heat fluxes could be discriminated. They can be summarized as a) Bulk transfer approaches, b) extreme pixel approaches, and c) the LUMPS-scheme. The three groups will be touched on in the following.

The bulk transfer approach uses remotely sensed surface temperatures together with the estimation of air temperature, net radiation, and soil heat flux to derive the turbulent heat fluxes. The approach focuses on the determination of the resistance to heat transfer r_{ah}. The estimation of the single terms is sometimes problematic. The term r_{ah} for example is a function of surface roughness, wind speed, and stability (Verma 1989, Kustas et al. 1989) and is expressed by the roughness lengths and the stability correction function. It inherently shows a high variability over heterogeneous surfaces like urban areas. Several approaches using morphometric methods have been introduced (Grimmond & Oke 1999) to account for this problem. Also the estimation of net radiation can be tricky due to shading effects and multiple scattering of radiation by high rise buildings. Nonetheless several studies have used this method to simply derive urban sensible heat fluxes or the whole energy budget. In some cases fairly good results were achieved, however other studies reported larger uncertainties and errors in the results (Voogt & Grimmond 2000, Offerle 2003, Xu et al. 2008). In this paper a similar bulk transfer approach is used as described in Xu et al. 2008, henceforward referred to as Aerodynamic Resistance Method (ARM).

The second group of methods, the extreme pixel approaches, uses extreme wet and dry pixels rendered either by manual setting or by the relation of surface temperature and surface albedo to find the partition of turbulent heat fluxes for each pixel. These methods originate in the SEBI (Surface Energy Balance Index) formulation proposed by Menenti & Choudhury (1993). SEBI was developed further by many researchers. For example Su (2002) introduced the SEBS (Surface Energy Balance System) scheme incorporating the aerodynamic roughness length for heat in the model. S-SEBI (Simplified Surface Energy Balance Index - Roerink et al. 2000) was derived from SEBS for use with remote sensing data. Because of its simplicity this method is applied in this paper to assess the general usability of this group of methods.

The SEBAL approach uses a combination of the bulk transfer approach and the extreme pixel approach. The sensible heat flux is modelled using the bulk aerodynamic resistance model in combination with an estimation of the net radiation and the soil heat flux. To estimate air temperatures, extreme pixels are used to find an assumed linear relationship between the difference of surface temperature and air temperature and surface temperatures (Bastiaanssen et al., 1998). Bastiaanssen et al. (2005) reviewed 26 research studies applying the SEBAL approach, finding that the overall accuracy of evapotranspiration for single-day events and

for scales of about 100 ha is +/−15% over agricultural areas. Further space and time integration would even improve the accuracy. SEBAL is not used in this paper as the results of S-SEBI did not indicate further work in this direction.

The LUMPS approach introduced by Grimmond & Oke (2002) is a linked set of equations using the method presented in de Bruin & Holtslag (1982) and Holtslag & van Ulden (1983). LUMPS requires only standard meteorological observations and basic knowledge of the surface cover. Similar to the bulk transfer approach it is driven by net radiation. Though the LUMPS approach was originally developed for surface station data, it was also used recently in combination with remote sensing data (Rigo 2007, Xu et al. 2008). Central to the LUMPS approach is the determination of surface dependent parameters, which also show a high variability over heterogeneous surfaces.

All three methods (ARM, extreme pixels and LUMPS) require net radiation and the soil heat flux as input. While net radiation can be estimated from satellite radiances and radiative transfer modelling, the soil heat flux is a function of the net radiation and surface properties. Please refer to Gowda et al. (2007) for a comprehensive review on energy balance methods with special focus on the determination of evapotranspiration.

To compare the results of the three different methods against field values, a measurement campaign was conducted from October 2007 to February 2008 in Greater Cairo. All relevant variables were continuously measured at three stations, each representing a major land cover class: ‘urban’, ‘agricultural’ and ‘desert’. Further details and results from this campaign are described in Frey et al. (2010).

After a presentation of the study site in chapter 2.2.2, the used in situ data and remote sensing products are introduced in chapter 2.2.3. The methods are introduced in chapter 2.2.4 and 2.2.5, separately for each the radiation and the heat fluxes. Chapter 2.2.6 presents the results of this paper and chapter 2.2.7 discusses these results and draws the conclusions of the paper.

2.2.2 Study area

The study area is Greater Cairo, the largest city in Egypt and on the African continent. Greater Cairo is a megacity, which administratively belongs to three different units: the governorates of Cairo, Giza and Qalyubiyya. For this historical division of the contiguous agglomeration of the megacity and due to many unregistered persons, cited inhabitant numbers may differ considerable. As a whole the population can be estimated to about 20 million inhabitants (Schlink et al. 2007). Besides the study area of the urban agglomeration there are neighbouring agricultural and natural desert landscapes, resulting in a high diversity of surface characteristics dominating the scene. Landscape features range from small-scale, irrigated farming spots, to the labyrinthine of the wadi systems in the Eastern desert, to diverse urban settlements (extremely dense housing to spacious villa quarters). This high diversity, manifesting itself in large amplitudes of surface albedo, emissivity, irradiation, soil humidity, and roughness, requires extremely robust procedures for the processing of the remote sensing data and quickly exposes potential weaknesses of each of the methodologies. Additional information about the study area can be found in Frey et al. (2010).

2.2.3 Data

2.2.3.1 Satellite data

The main remote sensing data source was ASTER (Advanced Spaceborne Thermal Emission and Reflection Radiometer), an optical imager on the TERRA satellite of NASA. It crosses the equator at about 10:30 local time. The spectral resolution ranges from the very visible to the thermal infrared with a spatial resolution from 15 m in the

visible to 90 m in the thermal infrared. ASTER has a swath width of 60 km and its revisit time is 16 days. All these features make ASTER an optimal candidate for medium scale landscape analyses. A key question of this paper is how ASTER data can be used for energy balance studies in urban regions. Since the atmospheric correction of optical satellite data is still a difficult task, it was decided not to rely on the standard procedures offered by NASA, but to investigate this processing step ourselves to estimate the uncertainty in the flux products induced by the atmospheric correction. Therefore, only Level-1B data are used in this paper.

For the atmospheric correction the operational aerosol product from MISR (Multi-angle Imaging SpectroRadiometer), also onboard TERRA, was taken. MISR makes optical multi-angular measurements and has a spatial resolution of 17.6 km. The algorithm for the product was developed by Martonchick et al. (1998). It is based on a set of predefined climatological aerosol mixtures to cover the most likely maritime, rural and urban conditions. Thanks to the broad swath width of 380 km the effective repetition period for a given ground location lies between 2 and 7 days (Keller et al. 2007).

Additionally a scene of ASAR (Advanced Synthetic Aperture Radar), an imaging microwave radar operating at C-band was used in this study. The scene was acquired in the ASAR image mode, where only one of seven predetermined swaths is sensed. A geolocated level 1B product with polarization set to 'VV' was chosen. Spatial resolution of the delivered product was 12.5 m. Further, the SRTM (Shuttle Radar Topography Mission) digital elevation model of the region was downloaded for use in the spatial irradiation modelling.

2.2.3.2 In situ data

In situ data from the CAPAC campaign (Frey et al. 2010) were used additionally to the satellite data. Besides standard meteorological parameters like air temperature, humidity and wind speed / direction, also the long and shortwave up- and downwelling radiation, the soil heat flux and the turbulent heat fluxes were measured continuously from 20 October 2007 to 20 February 2008 at three locations. The first station was on the roof of a building inside the campus of the Cairo University in Giza, west of the River Nile. At this station the soil heat flux was not measured, but indirectly derived from the other terms as described in chapter 2.2.5.1. The second station was on the northern rim of Cairo in the Bahteem district on an agricultural field inside a meteorological station of EMA (Egyptian Meteorological Authority). The third station was also part of a meteorological station of EMA outside the agglomeration of Cairo in the desert, next to the satellite town 10th Ramadan. Further details of the campaign and a description of the data can be found in Frey et al. (2010).

In a first step the in situ measurements were used for the development of a 'best fit' version of the atmospheric correction procedure as described in chapter 2.2.4.1. Secondly the data were used for the development of empirical regression equations for a) the soil heat flux, b) the air temperature, c) two empirical parameters of the LUMPS approach and d) the aerodynamic resistance. Finally the data served as comparison material for the radiation and heat fluxes described in chapter 2.2.6.

Flux measurements using the eddy covariance technique frequently suffer from a closure gap in the energy balance (for example Wilson et al. 2002). The sum of the measured turbulent fluxes is sometimes lower than the available energy (the difference between net radiation and the soil heat flux). This residual is subject to current research and was attributed, amongst other reasons, to the influence of advection, lacking homogeneity of the surface, weak turbulence, and the exclusion of large eddies through a probably too short sampling time (Foken 2008). In the data of CAPAC a considerable residual was found, too (Frey et al. 2010). Most probably, it is

reasonable partitioning the residual among the turbulent heat fluxes to close the gap. However, it is unclear, to which percentages this distribution must take place. Twine et al. (2000) proposed a simple distribution proportional to the Bowen ratio. This approach was applied here, despite the supposition that the ratio might be different for large eddies (Foken 2008).

Another constraint of the eddy covariance technique is that fluxes are average values of a certain time period (30 minutes in the CAPAC campaign), while satellite data are instantaneous measurements. Therefore during the averaging period considerable changes in the radiation situation might occur, probably influencing the derivation of these fluxes considerable. Such changes are not incorporated in the satellite measurement, surely leading to a certain mismatch when comparing products from the two approaches.

The following dates of ASTER data were available during the campaign in Cairo. Not all stations ('Cairo University', 'Bahteem', and '10th Ramadan') were covered by all scenes. An X in Table V indicates that the station is covered by at least one scene during this day. Scenes (a) are usually depicting the Northern part of the agglomeration, scenes (b) show the southern part.

Unfortunately the ASTER SWIR instrument suffers from thermal anomalies from December 2008. Therefore the SWIR data from 24 December and 2 January could not be used in this study. It mainly affected the estimation of the broadband albedo. The substituting algorithm is described in Chapter 2.2.4.2.1. Further, the scene of 15 November 2007 could not be used due to wide spread cloud cover over Cairo. In addition, all other scenes had more or less cloud contaminations. Cloud areas were first detected using an automated cloud-detection algorithm. As the algorithm was not able to detect all areas where strong haze occurred, additional manual edition was necessary. The cloudy areas were not used in any of the following analyses.

Table V Dates of ASTER acquisitions during the CAPAC campaign.

Date	Number of scenes	'Cairo Univers-ity'	'Bah-teem'	'10th Ramadan'
15 Nov 07			X	
22 Nov 07	2 (a+b)	X	X	X
1 Dec 07	2 (a+b)	X	X	X
24 Dec 07	2 (a+b)	X	X	X
2 Jan 08	1			X

2.2.4 Methods: Radiation balance

2.2.4.1 Atmospheric correction

To obtain bottom of the atmosphere radiances (BOA radiances) from the shortwave ASTER data, the at-sensor or top of the atmosphere radiances (TOA radiances) were atmospherically corrected for the influence of absorbing and scattering processes according to

$$L_{toa}(\lambda) = L_p(\lambda) + \tau(\lambda) \cdot \rho(\lambda) \cdot L_g(\lambda) + L_{ad}(\lambda) \quad (7)$$

whereas L_{toa} is the radiance at-sensor [Wm^{-2}sr^{-1}µm^{-1}], L_p is the path radiance [Wm^{-2}sr^{-1}µm^{-1}], τ is the average transmissivity between the Earth surface and the sensor, ρL_g is the reflected radiance [Wm^{-2}sr^{-1}µm^{-1}], L_{ad} are the adjacency effects [Wm^{-2}sr^{-1}µm^{-1}] and λ is the spectral range of the respective band. The term ρ is the reflectance of the Earth surface. To correct the image for the atmospheric effects, L_p and τ were determined for each ASTER band using the radiative transfer model MODTRAN. The input atmosphere for the calculations was taken from midday radiosonde ascents south of Cairo in Helwan from the same days like the ASTER over flights. For the aerosol setting a first default option 'urban, visibility 5 km' was taken. It was considered the most suitable setting, as Cairo is an overwhelming megacity with heavy air

pollution. The aerosol function was set to 'Mie scattering'.

After Frey et al. (2010) evidence is given that the aerosol load is not equally distributed over the images. Since, L_p and τ are not constants, but vary in the spatial domain. Several options in determining the spatial aerosol optical depth (*AOD*) were investigated. First of all, it was tried to determine *AOD* from the ASTER data itself, following the method of Kaufmann et al. (1997). However, because of the actual lack of knowledge of band relations for bright surfaces, this method was not possible to conduct. Second, the MODIS *AOD* product was examined for all available dates. But as the method also uses the method of Kaufmann et al. (1997) the product had too many missing pixels in the area of Greater Cairo, so this option was also not feasible. The third option was to take the *AOD* product from MISR data (Martonchik et al. 1998). As this product does not rely on such band relations, enough pixels were available for the area. Band 2 (558 nm) was taken as input for the correction process. This approach is henceforth addressed as the 'best guess' option, assuming to have no other reference data than the radiosonde ascents. The fourth and last option also used the MISR *AOD*, but the aerosol setting of MODTRAN was put to 'rural, visibility 23 km'. Even though this setting is not optimal, this option provided the best fit with the in situ measured albedo values (mean absolute difference 0.022). In this study, we will use option three ('best guess') and option four ('best fit') for further analyses. These options will apply also for the calculation of the broadband solar irradiation, the net radiation and consequently for all other dependent variables.

The relation of τ with *AOD* follows a negative exponential curve; the relation of L_p with *AOD* starts with a logarithmic curve, but then decreases again. For the correction of the ASTER images only *AOD* values up to 1 are considered. Therefore it was straight forward to assume a linear relation-ship of the path radiance and the transmissivity with the *AOD* in this range (see Figure 12).

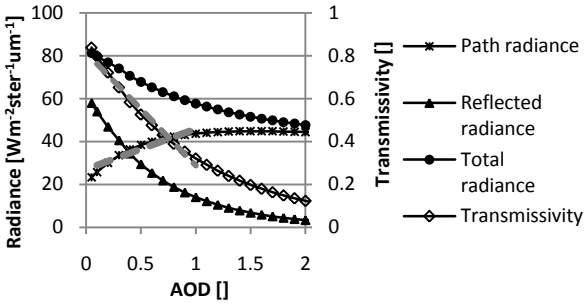

Figure 12 Dependence of path radiance, reflected radiance, total radiance and transmissivity on *AOD*

L_p is not only dependent on *AOD*, but also on ρ, as depicted in Figure 13. Therefore an additional interpolation was introduced to scale the estimated L_p to the apparent ρ. As ρ is only available after the atmospheric correction, slightly modified TOA ρ were used. They were calculated as

$$\rho_{toa} = \frac{L_{toa} \cdot d^2}{L_{exo} \cdot \cos \Theta_s} \qquad (8)$$

and then multiplied by 1.1, an manual set factor. ρ_{toa} is the top of the atmosphere reflectance, L_{exo} the exo-atmospheric irradiance for the respective ASTER band [$Wm^{-2}sr^{-1}\mu m^{-1}$], d the Earth-Sun-Distance in astronomical units and Θ_s the solar zenith angle [°].

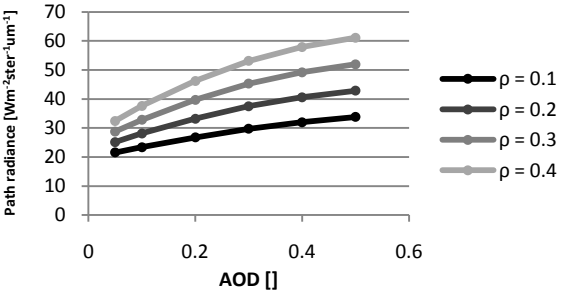

Figure 13 Dependence of path radiance on the AOD and the reflectance of the Earth surface

For the correction of each scene, six MODTRAN runs were necessary with different combinations of *AOD* and *ρ*, yielding a different output for each run. Four runs were necessary to find the relation between L_p, τ and the *AOD* and *ρ*, two additional new runs were necessary to calculate the incoming solar irradiance and its dependence on the *AOD*. The incoming solar irradiance is needed for the calculation of *ρ*. Its calculation is comparable to the procedure described in chapter 2.2.4.2.3.

ρ(λ) is the spectral surface reflectance and calculated as

$$\rho(\lambda) = \frac{L_r(\lambda)}{L_g(\lambda)} \quad , \qquad (9)$$

where L_r is the radiance reflected from the Earth' surface [$Wm^{-2}sr^{-1}\mu m^{-1}$] and L_g the global irradiance (beam plus diffuse irradiance) [$Wm^{-2}sr^{-1}\mu m^{-1}$].

The correction of the longwave bands is similar to equation 1. The basic equation is

$$L_{toa}(\lambda) = L_p(\lambda) + \tau \cdot L_g(\lambda) + L_r(\lambda) \quad , \qquad (10)$$

with L_{toa} being the TOA radiance [$Wm^{-2}sr^{-1}\mu m^{-1}$], L_p the path radiance [$Wm^{-2}sr^{-1}\mu m^{-1}$], τ the average transmissivity and L_r the radiance reflected from the Earth surface (a very small term). As the longwave radiation is not influenced significantly by aerosols or *ρ*, these terms were kept constant over the full scene.

2.2.4.2 Modelling of net radiation

The net radiation $Q*$ [Wm^{-2}] is given as

$$Q^* = (1 - \alpha) \cdot K_{\downarrow} + L_{\downarrow} - L_{\uparrow} \quad , \qquad (11)$$

with α denoting the broadband surface albedo, $K_{\downarrow}$ the broadband irradiation [Wm^{-2}], $L_{\downarrow}$ incoming longwave radiation [Wm^{-2}], and $L_{\uparrow}$ outgoing longwave emission [Wm^{-2}]. In the following, all terms will be explained separately.

2.2.4.2.1 Broadband albedo *α*

To convert the spectral reflectances *ρ* of ASTER obtained from the atmospheric correction algorithm to broadband albedos, an empirical equation was used. The equation was gained from a multiple regression approach, using 86 samples of different surface materials of the ASTER spectral library Version 1.2 of JPL Laboratories. The following flow chart (Figure 14) describes the different steps of the algorithm.

The regression of the broadband reflectances *α* and the modelled reflectances ρ_i showed a very high correlation of 0.9986, even though surface materials with highly varying spectral reflectances were chosen. In case of the ASTER scenes from 24 December 2007 and 01 February 2008 only the VNIR bands were available due to a temperature anomaly in the detector. Therefore, another equation was obtained for these dates. The resulting empirical regression equations are listed in the annex.

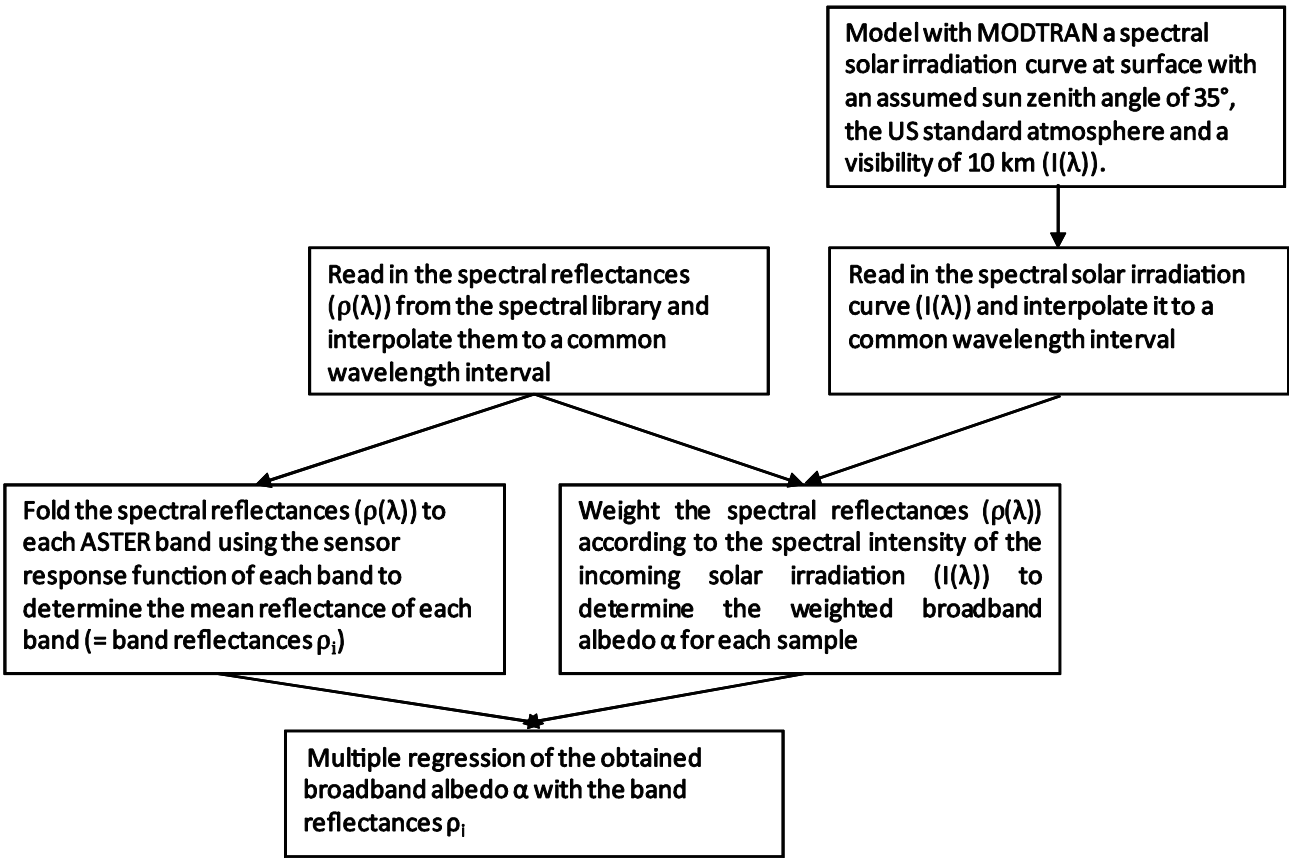

Figure 14 Flowchart for the estimation of the empirical regression equation for the broadband albedo

2.2.4.2.2 Outgoing longwave emission $L_{\uparrow}$

For the outgoing longwave emission $L_{\uparrow}$ the atmospheric corrected TOA radiances using the 'best guess' option were converted to brightness temperatures using the Planck-function. As the Planck-function is only valid for a single band wave number, the correction of the least-square-fit method described in Liang (2004) was used. Using an assumed synthetic emissivity, surface temperatures were then calculated from band 14. The assumed emissivities were 0.98 (water and pure vegetation) and 0.90 (urban and desert). In urban and agricultural areas of the ASTER scenes, where often mixed pixels occur, the formulas of Carlson & Ripley (1997) were used, incorporating the before mentioned emissivities for pure pixels. The emissivities of the other bands were then obtained by comparing their surface temperatures with the surface temperatures of the emissivity-corrected band 14. The resulting band emissivities (ε_{bi}) were then converted to broadband emissivities (ε) using empirical regression equations for each land use. The empirical equations were generated similar to the shortwave case. Only, the weighting function for the broadband emissivity was the Planck-curve at 300 K (instead of the solar irradiation). The equations for the different land use classes are also in the annex.

2.2.4.2.3 Incoming broadband irradiation $K_{\downarrow}$ and incoming longwave radiation $L_{\downarrow}$

Incoming broadband irradiation $K_{\downarrow}$ was estimated using MODTRAN runs over the shortwave range from 0.25 to 4 microns. For the option 'best guess' the same MODTRAN settings were used as for the atmospheric correction of the band radiances in the 'best guess' mode. For the option 'best fit' however, the in situ

measured $K_{\downarrow}$ values from the CAPAC campaign (Frey et al. 2010) were used to iteratively find the optimal *AOD* values for the three available stations by minimizing the differences between the measured and the modelled $K_{\downarrow}$ values. These values were then generally applied to the image according to the respecting land cover.

The spatial solar irradiation $K_{\downarrow}$ is given as the sum of beam irradiation ($K_{\downarrow b}$), diffuse irradiation ($K_{\downarrow d}$), and irradiation reflected from the environment ($K_{\downarrow r}$), all terms in Wm^{-2}. In case of shaded areas, the beam radiation is dismissed.

$$K_{\downarrow sunlit}(x,y) = K_{\downarrow b} \cdot \cos\varphi\,(x,y) + K_{\downarrow d} \cdot svf(x,y) + K_{\downarrow r}(x,y) \quad (12)$$

$$K_{\downarrow shaded}(x,y) = K_{\downarrow d} \cdot svf(x,y) + K_{\downarrow r}(x,y) \quad (13)$$

φ is the illumination angle [°] and can be calculated following Liu & Jordan (1963) using the SRTM DEM. *svf* is the sky view factor, which describes the proportion of the upper hemisphere that is 'seen' by a pixel. It is also calculated with the SRTM DEM. Its calculation is described in Frey & Parlow (2009). The irradiance reflected from the environment is calculated iteratively using following parameterization:

$$K_{\downarrow r}(x,y) = K_{\downarrow}(x,y) \cdot \alpha(x,y) \cdot (1 - svf(x,y)) \quad (14)$$

Incoming longwave radiation $L_{\downarrow}$ was also estimated using the ‚best guess' option in MODTRAN. Yet, no 'best fit' option was introduced to the longwave fluxes.

2.2.5 Methods: Heat fluxes

2.2.5.1 Modelling of the soil heat flux Q_s

The soil heat flux Q_s [Wm^{-2}] is a function of the available energy on the surface and the layers beneath and the thermal properties of the soil. Thermal properties are dependent on soil moisture and porosity and therefore only constant at sealed surfaces. Whilst the estimated Q^* stands for the available energy, it is more difficult to describe the thermal properties of the ground. Common approaches found in literature are using different vegetation indices for this purpose; the SEBAL procedure for example (Baastianssen et al. 1998) includes also the surface temperature and the albedo in the calculation.

All approaches found in the literature and used in this paper, except the one from Parlow (Rigo & Parlow 2006), were designed for natural surfaces.

Table VI shows five different approaches that were found in literature and were tested in this study. The indices '*fcover*' (fraction of vegetation cover), '*NDVI*' (normalized difference vegetation index) and '*MSAVI*' (modified soil adjusted vegetation index) were calculated following De Ridder & Mensink (2003) and Qi et al. (1994) for each of the 'best fit' and the 'best guess' option.

Apart from these approaches, a new formula was derived using linear regression with a set of in situ data from the CAPAC campaign. Due to extremely high fluctuations in the storage term of the ground heat flux (Frey et al. 2010), it was decided only to work with 30 minute averages. Daytime Q^* and Q_s (07:00–16:00) from the period from 20 November 2007 to 20 February 2008 were used.

Table VI Literature approaches for the calculation of the soil heat flux

Approach	Equation	
'Choudhury'*	$Q_s = Q^* \cdot \left(c1 \cdot fcover + c2 \cdot (1 - fcover)\right)$	(15)
'Norman'**	$Q^*_{soil} = Q^* - Q^* \cdot e^{0.9 \cdot ln(1-fcover)}$ and $Q_s = 0.35 \cdot Q^*_{soil}$	(16)
'Parlow/urban'***	$G_{urban} = (0.3673 - 0.3914 \cdot NDVI) \cdot Q^*$	(17)
'Parlow/rural'***	$G_{rural} = (0.3673 - 0.3914 \cdot NDVI) \cdot Q^*_{short} \cdot \left(-0.8826 \cdot ln\left(R_{n\_short}\right) + 5.0967\right)$	(18)
'SEBAL'****	$Q_s = Q^* \cdot \frac{T_S}{\alpha} \cdot (0.0038 \cdot \alpha_0 + 0.0074 \cdot \alpha_0^2) \cdot (1 - 0.98 * NDVI^4)$	(19)
'Sobrino'*****	$Q_s = 0.5 \cdot Q^* \cdot e^{-2.13 \cdot MSAVI}$	(20)

* Chourdhury et al. (1987), c1 = 0.05 for Vegetation (Monteith & Unsworth, 1990), c2 = 0.315 for bare soil (Kustas & Daughtry, 1990)
** Norman et al. (1995)
***Rigo & Parlow 2006
**** Baastianssen et al. (1998)
***** Sobrino et al. (2005)

The data were filtered for sunny hours by comparing actual net radiation to an adapted sine wave. The daily curve of Q_s features a time offset towards the curve of Q^* of about one hour. Therefore the whole time series of the latter parameter was shifted backwards one hour for the regression calculations. The resulting formulas, split to land cover, are:

$$Q_{s\_urban} = 0.342555 \cdot Q^*_{h-1} - 1.22602 \quad r^2 = 0.77 \quad (21)$$

$$Q_{s\_rural} = 0.140445 \cdot Q^*_{h-1} - 0.39747 \quad r^2 = 0.78 \quad (22)$$

$$Q_{s\_desert} = 0.312526 \cdot Q^*_{h-1} - 0.318237 \quad r^2 = 0.94 \quad (23)$$

Q^* of one hour before the over flight (Q^*_{h-1}) can be calculated from Q^*_h assuming that Q^* follows the above mentioned idealised sine wave. In the morning the wave starts at the point, when Q^* gets positive (sine = 0). It then grows to the maximum (sine = 1) at the point of time, when Q^* has its maximum to decrease to sine = 0 again in the evening, when Q^* gets negative. Q^*_{h-1} is then

$$Q^*_{h-1} = Q^*_h \cdot \frac{\sin(\beta_{h-1})}{\sin(\beta_h)} \quad (24)$$

with Γ given in Table XI in the annex. This approach is further addressed as 'Frey/landuse'. In a second approach the *NDVI* was used to explain the differences between the stations, similar to the 'Parlow' approaches for example. The first term explains the variation of the landuse and was derived specifically for the late morning hours. The second term describes the relation between Q^* and Q_s and is valid for the whole day. For the regression equation only data

up to the 31 December 2007 were used, due to the unavailability of the *NDVI* afterwards.

$$Q_S = (-0.528892 \cdot NDVI + 0.369931) \cdot (1.15453 \cdot Q^*_{h-1} - 17.5422)$$

$r^2 = 0.6$ (25)

Q_s was not measured at the urban station. Therefore it had to be deduced from the balance of Q^* and the turbulent heat fluxes. However, for not perfectly homogeneous surfaces the energy balance is not closed and a considerable unexplained residual remains. This residual was roughly estimated for the urban station using the residuals from the agricultural and the desert station. Then Q_s was derived as balance from Q*, the turbulent heat fluxes and the estimated residual. Of course this procedure introduced an additional source of uncertainty. But it is assumed, that such error is smaller than the error that results from not accounting any residual.

Besides Q^* other variables like α, ε and the *NDVI* were tested for their feasibility in describing Q_s. But none of these variables was able to improve the regression coefficients. In the case of urban surfaces the term 'ground heat flux' would be more appropriate than the term 'soil heat flux'. However, as latter term was used in Part 1 (Frey et al. 2010), this term will also be used in this paper for continuity reasons.

2.2.5.2 LUMPS

LUMPS stands for the Local-Scale Urban Meteorological Parameterization Scheme and is a set of equations to calculate turbulent fluxes using standard meteorological measurements and two semi-empirical parameters describing the surface cover. Its origin is a simplified Penman-Monteith approach, incorporating the Priestley-Taylor coefficient for extensive wet surfaces and extending it to non-saturated surfaces (Grimmond & Oke 2002). While the α parameter should account for the strong correlation between the heat fluxes (Q_H, Q_{LE}) and the available energy (Q^*- Q_s), β stands for the uncorrelated part (Holtslag & van Ulden, 1983). In this study both parameters were derived empirically from the in situ data of the CAPAC campaign. The derived values are given a) for all wind directions ('all directions' approach) and b) also for each station for a vegetated and a non-vegetated wind sector ('sectoral' approach). Further, a comparison with a set of selected values from literature from Grimmond & Oke (2002) is given. Thereby the values from Mexico City were taken for the urban station. Table VII gives the α and β values. The LUMPS equations for the turbulent heat fluxes are as follows:

$$\boldsymbol{Q_{LE} = \alpha \left[\frac{1}{1+\left(\frac{\gamma}{s}\right)}\right](Q^* - Q_s) + \beta} \quad (26)$$

$$Q_H = \alpha \left[\frac{1-\alpha+\left(\frac{\gamma}{s}\right)}{1+\left(\frac{\gamma}{s}\right)}\right](Q^* - Q_S) - \beta \quad (27)$$

Table VII α and β parameter derived from the in situ data of the CAPAC campaign

	'Cairo University'		'Bahteem'		'10th Ramadan'	
	α	*β*	*α*	*β*	*α*	*β*
All directions	1.62	0.73	1.57	56.50	0.77	6.78
Non-veg sector	1.46	3.43	1.52	43.99	0.78	0.78
Vegetated sector	1.64	7.2	3.17	33.16	0.71	9.70
Values from literature (Grimmond & Oke 2002)	0.19	-0.3	1.2	20	0.2	20

2.2.5.3 ARM (Aerodynamic Resistance Method

An alternative method to estimate the sensible heat flux is the bulk transfer equation,

$$Q_H = \rho_a * C_p * \frac{T_s - T_a}{r_{ah}} \quad , \tag{28}$$

where ρ_a is the density of air [kg m^{-3}], c_p the specific heat of air at constant pressure [J kg^{-1} K^{-1}], T_s is the surface temperature [K] calculated from the ASTER TIR data and T_a is the air temperature [K]. r_{ah} is the aerodynamic resistance for heat [sm^{-1}] (Verma 1989). Q_{LE} is then the residual of the available energy and Q_H. Spatial T_a had to be estimated and was deducted using empirical regression equations with T_s and wind speed obtained from the CAPAC campaign data. The equations are given in the appendix. An additional approach using an expression given in Xu et al. (2008) was also examined.

$$T_a = \left({T_s}^4 - \left(\frac{0.08 * K_{\downarrow} \cdot (1-\alpha)}{\varepsilon \cdot \sigma} \right) \right)^{0.25} \tag{29}$$

The aerodynamic resistance r_{ah} can be determined with an approach using the roughness length, stability correction functions for momentum and heat, and the friction velocity (Voogt & Grimmond 2000). The estimation of these parameters needs a detailed surface scheme, including a digital surface model of the urban area. However, no such detailed model was available for Cairo in sufficient accuracy; therefore another empirical approach using radar data was pursued. Several studies have shown that aerodynamic roughness length can be represented by radar data (Prigent et al. 2005, Greeley et al. 1997, Blumberg 1993). Using the measurement data from the CAPAC campaign an empirical relation was found between r_{ah} and the radar backscattering coefficient σ^0 of the ASAR image from 02 January 2008. The in situ measurement data showed that r_{ah} was not constant over time probably due to surface inhomogeneities around the stations. A slight directionality was found dependent on the wind direction (Figure 15). During winds from the northern sector, r_{ah} was highest at all three stations. Largest difference in mean r_{ah} values between the northern and the southern sector was found at the agricultural station with 29.5 sm^{-1}. The urban and the desert station however showed only small differences of 8.6 sm^{-1} and 6.9 sm^{-1} respectively. For the regression equation, all wind directions were used.

The radar image was smoothed with a 13x13 filter to remove speckle and other disturbing effects before serving as input in the regression calculation. The resulting equation is

$$r_{ah} = -0.0647 * \sigma^0 + 98.229 \tag{30}$$

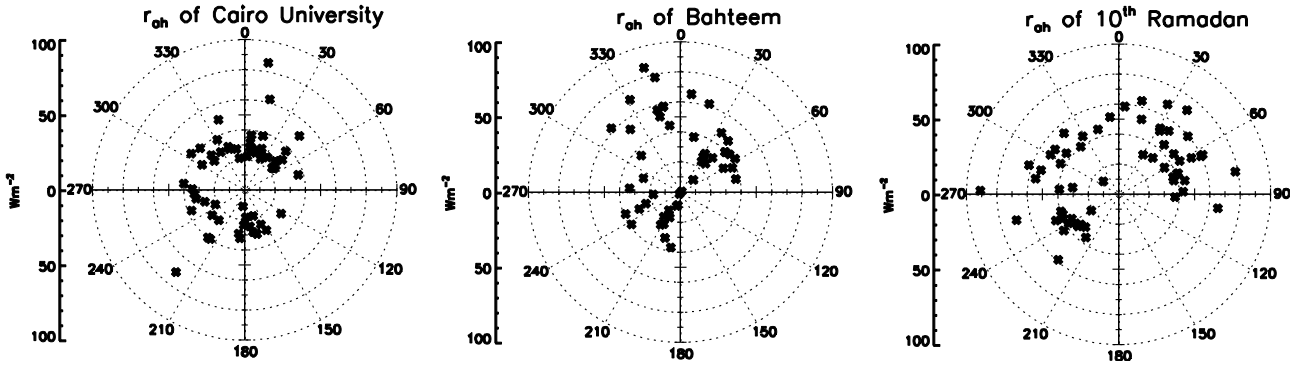

Figure 15 Measurement values of rah of Cairo University, Bahteem and 10th Ramadan in dependence of the wind direction

2.2.5.4 S-SEBI

The S-SEBI - Method (Simplified Surface Energy Balance Index - Roerink et al. 2000) estimates the evaporative fraction Λ from remote sensed T_s and α. Λ describes the ratio of the energy that goes into Q_{LE} and the available energy of Q^* after subtraction of Q_s, which is the amount of energy that goes into the turbulent heat fluxes.

$$\Lambda = \frac{Q_{LE}}{Q_{LE}+Q_H} = \frac{Q_{LE}}{R_n - Q_s} \tag{31}$$

According to the theory of S-SEBI Λ can also be expressed by (imaginary) surface temperature differences.

$$\Lambda = \frac{T_H - T_S}{T_H - T_{LE}} = \frac{a_H + b_H \cdot \alpha - T_S}{a_H - b_H + (b_H - b_{LE}) \cdot \alpha} \tag{32}$$

The upper term corresponds to Q_{LE}. It is the difference between an imaginary albedo controlled temperature T_H [K] (assuming no evaporation) and the real temperature T_s [K]. The lower term corresponds to the available energy. It is the imaginary albedo controlled temperature T_H minus the imaginary evaporation controlled temperature T_{LE} [K]. T_H is the highest possible temperature for a given α, assuming there is no evaporation. T_{LE} is the lowest temperature for a given α, assuming there is no Q_H. These extreme temperatures can be found from an albedo-temperature scatter plot. A straight line that goes through all albedo controlled and another line that goes through all evaporation controlled points can be found through a regression of all maximum and minimum values of the triangle-shaped scatter plot of the albedo and the temperature to define the gains (b_H and b_{LE}) and offsets (a_H and a_{LE}) (Roerink et al. 2000).

T_s also depend on the height, the slope and exposition of the surface. Therefore two correction steps were performed. Firstly, a simple correction for the height above a reference height was performed. An average value of 0.6°K per 100 m was applied (Roerink et al. 2000). While the Nile delta consists of more or less flat areas, the desert surroundings, mainly the eastern desert, includes several wadi systems, which can be characterized through their various illumination geometries. Sunlit slopes feature much higher surface temperatures than shaded slopes. To eliminate this effect, the regression line of surface temperatures and modelled solar irradiation was rotated to be horizontally. Through this approach, the influence of the solar irradiation (which is mainly determined by the exposition and the slope of the surface), is cancelled out and the temperature values correspond to an “imaginary” flat surface. This step was only applied to the desert areas, where evaporation is assumed to be minimal or zero and where the pixels should represent T_H. Therefore a variation in surface temperature for a given albedo would be misleading and distort the S-SEBI results.

According to the theory of S-SEBI, all pixels having a zero-evaporation should equal to the maximum temperature line. However, this is not the case in the area of interest of this research. All scenes feature large desert areas, where the evaporation tends to zero. Even though they show quite high variation in the distribution of the surface temperature as can be seen in Figure 16.

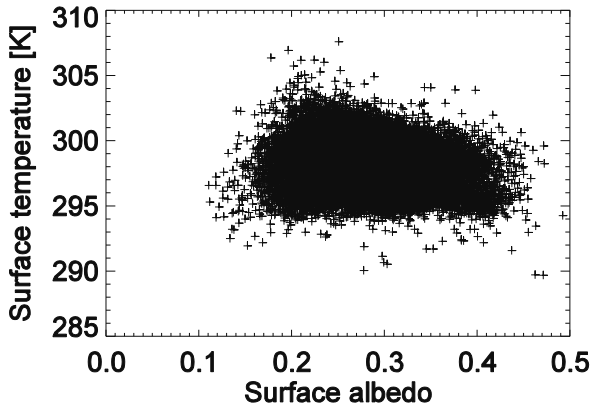

Figure 16 Scatterplot of the surface broadband albedo and the surface temperature [K] for the height and exposition corrected desert pixels for the scene a of 24 December 2007

Choosing the maximum temperatures for each surface albedo, as specified by S-SEBI, these pixels may be misguiding, as pixels, featuring lower surface temperatures, might also represent areas of nearly zero-evaporation. The result of this fact is an underestimation of evaporation in well irrigated areas and an overestimation of dry areas. Given the fact, that surface temperatures do not only depend on albedo and evaporation, S-SEBI is not suitable to estimate surface heat fluxes in this area.

2.2.5.5 Source footprint models

Eddy flux towers measure fluxes originating from an extended upwind source area of the tower. The spatial extent of the source area depends on the measuring height, the roughness of the surface, and the stability of the boundary layer. In the CAPAC campaign considerable directionality was found in the turbulent flux data, especially at the agricultural station 'Bahteem' (Frey et al. 2010). To be able to compare these in situ measurements with the remote sensing data, it was decided to use source footprint models. Analytical approaches describing the source area have their origin in the works of van Ulden (1978) and Pasquill and Smith (1983). Theoretically, these models are limited to ideal homogeneous surface layer conditions. However, flux measurements are mostly conducted in non-ideal environments asking for a more sophisticated approach. But simplicity and decreasing computational expense is an important precondition for an operational application of footprint models. More complex models which include non-ideal topography and spatial heterogeneity are therefore not suitable for this purpose (Neftel et al. 2008). In this paper three different analytical models are used. In the following, they will be referred to as KM model (Kormann & Meixner 2001), H model (Hsieh et al. 2000, as used in Li et al. 2008) and C model (Chen et al. 2009).

The flux footprints were calculated for a 4000x2000 grid and scaled up to the necessary spatial resolution of the ASTER data. As the total footprints would not exactly sum up to unity, they were interpolated so that the sum of all pixels would be one. Afterwards they were rotated into the prevailing wind direction and laid over the respective satellite image flux product with the footprint origin located at the pixel corresponding to the in situ measurement. Figure 17 shows the footprints for the three stations on 24 December 2007. Footprints were used for the evaluation of the LUMPS and the ARM results.

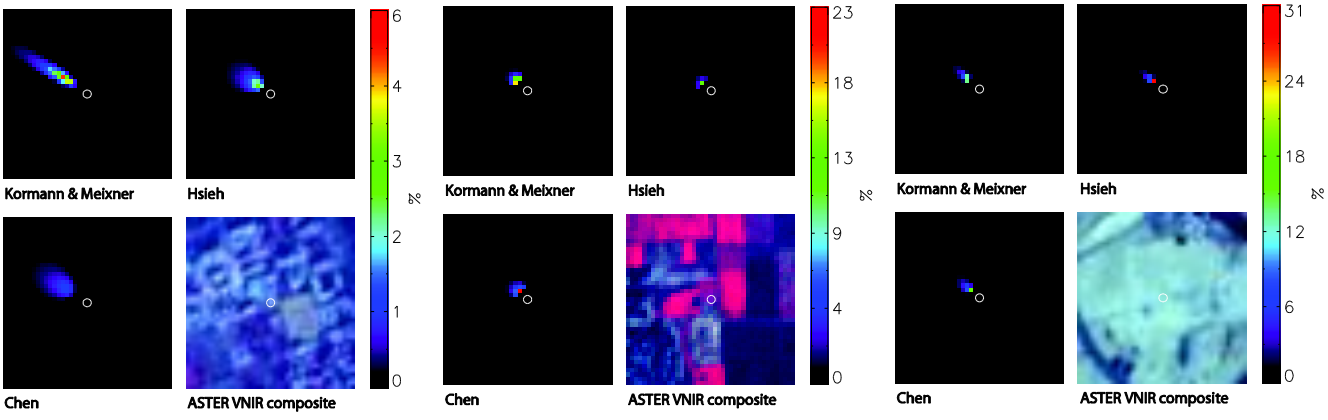

Figure 17 Footprints for the three stations and the scenes from 24 December 2007. Due to less unstable conditions, the flux footprints extend over a large area. As the colour table is linear, only a part of the footprint is given in color.

2.2.6 Results

The presentation of the results follows two strategies. First the calculated parameters from the ASTER data are compared to the in situ measurements. The comparison is executed by the analysis of mean absolute differences (*MAD*), which are the mean values of the differences between associated values from each the in situ measurement and the remote sensing approaches. In a second step the spatial variations in the image are discussed on the basis of what is expected and realistic. Basis for this discussion are the general land use classes 'urban', 'agriculture' and 'desert'.

2.2.6.1 Radiation fluxes

The calculated radiation fluxes from the ‚best guess' and the ‚best fit' option were compared to the in situ measured fluxes (original 1 minute averages) using directly the values of the pixel associated with the station. Assuming a purely cosine dependent sensor response of the in situ radiation measurement instrument, reflected radiation for the agricultural and the desert station is coming from a circular area within a radius of 11 m. In case of the urban station however, the radius is much larger. But, using only the height difference between the sensor and the roof, about 90% of the flux would come from a circle within a radius of 45 m. Comparisons showed that resulting *MAD*s did not improve when taking into account the surrounding pixels. Considering also the unknown position of the tower inside the pixel and the small proportion of radiation only originating surrounding pixels, the actual pixel value was taken, even though the resolution of the VNIR ASTER bands is 15 m (VNIR).

For the urban and the agricultural station three over flights could be used, the desert station had four scenes for comparison. The *MAD*s of these 10 value pairs were calculated and are listed in Table VIII. The critical term is the albedo, which has in the 'best fit' option a *MAD* of 2.2 %. All differences of the albedo were of such magnitude, independent on the station. The high *MAD* of the 'best guess' irradiation of 48.9 Wm^{-2} could be improved significantly by using the 'best fit' option, reducing the *MAD* to only 12.6 Wm^{-2}. The two longwave terms both showed a good agreement in the 'best guess' case, therefore no 'best fit' option was introduced. The net radiation finally could be determined with 11.6 % accuracy in the 'best guess' option, and with 6.9% in the 'best fit' option. As the 'best fit' option is fitted to the measurement values, this comparison is of course not independent. Anyhow, the 'best guess' version can be interpreted as an error measure for other pixels not included in this comparison.

The in situ radiation values were measured using a CNR1 from Kipp & Zonen. The specification sheet lists the expected accuracy for the daily totals to be +- 10 %. A calibration of the instruments at the end of the campaign improved the accuracy to about 10% for single measurements. Having this in mind, the achieved 11.6 % accuracy for the net radiation using the 'best guess' option is good.

Table VIII Mean absolute difference (MAD) of the 4 key variables of the radiation balance. The values in brackets indicate the percentage of the MAD on the mean of the in situ measured values

	MAD 'Best guess'	*MAD* 'Best fit'
Albedo [%]	3.5 (15.4 %)	2.2 (9.8 %)
Irradiation [Wm^{-2}]	48.9 (8.5 %)	12.6 (2.2 %)
Longwave emission [Wm^{-2}]	8.4 (2.0 %)	Na
Counter radiation [Wm^{-2}]	20.4 (6.5 %)	Na
Net radiation [Wm^{-2}]	37.6 (11.6 %)	22.3 (6.9 %)

A main constraint in the modelling of the irradiation was the limited accuracy of the used DEM. The DEM had a spatial resolution of 3arcsecond (≈ 90 m), but could not resolve exactly the geomorphologic features occurring in the desert like the wadi systems. Further, the modelling of the irradiance reflected from opposed slopes is simply parameterized using the neighbouring pixel's reflectance and therefore might be underestimated. Hence, areas of massive over- and underestimation of the incoming spectral irradiance were present in some areas of the desert, finally resulting in wrong albedo values. Also, radar data exhibit increased scattering over rough surfaces. Therefore, the SRTM data over urban areas showed some irregularities. To account for this, the slope was set to zero over urban areas. A further constraint is given by the fact, that solar irradiation was modelled assuming the urban surface to be flat, for example no enhanced reflections from sun-facing walls and sloped roofs or diminishing effects of shadows were considered. This assumption can lead to considerable errors, as was shown in Frey & Parlow (2009). For the used ASTER scenes a maximum error of 2 % is estimated for this geometry effect.

Figure 18 shows the 'best fit' net radiation from scene (b) of 24 December 2007 for a part of Greater Cairo. The three main landscape features can be easily recognized: The desert areas in the right part of the image with low net radiation values, the agricultural fields in the upper left part with high net radiation values and the urban parts with medium net radiation values. The River Nile is also clearly visible with very high values.

A similar distribution is found in all scenes; however, in some scenes the net radiation of the urban areas almost equalled the net radiation of the agricultural areas. The main reason for this difference is the albedo. So is the difference between the mean urban and mean agricultural albedo of the scene (b) from 01 December 2007 only 0.007, while in the scene (b) from 24 December 2007, which covers a very similar sector, it is 0.041. Even though the difference between the mean values is very small, there results an effect on the spatial pattern. The urban net radiation of the scene (b) from 01 December 2007 is 9.1 Wm^{-2} lower than the agricultural net radiation. In case of the scene (b) from 24 December2007 it is 30.3 Wm^{-2} lower.

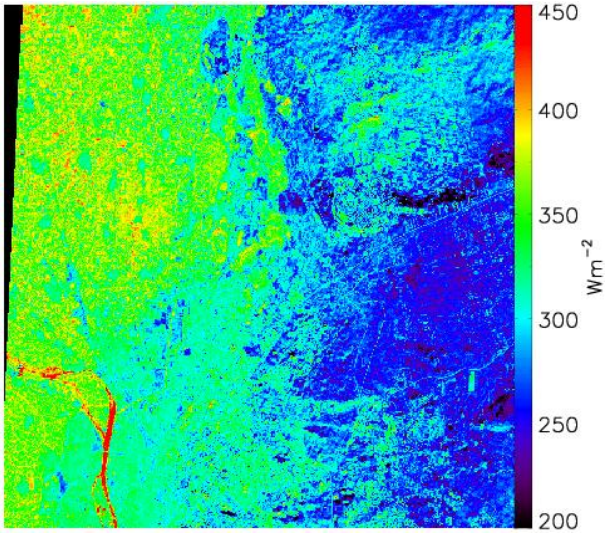

Figure 18 Net radiation (option 'best fit') from one of the ASTER scenes from 24.12.2007

2.2.6.2 Soil heat flux

Q_s was derived using the six described methods from literature and using the regression equations obtained from the in situ measurements. It was compared to half hour averages of Q_s from the measurement campaign. The option 'best guess' and the option 'best fit' were used as input in the comparison. However, none of the approaches was able to reproduce the measured Q_s very accurately. Generally the option 'best fit' performed slightly better than the option 'best guess'. But the *MAD* of 'best fit' was only few percent lower than 'best guess'. The best agreement showed the 'Parlow/urban' approach. There the *MAD* for the option 'best fit' was 18.9 % of mean Q_s. The new approaches and the 'Choudhury' approach performed similarly

well (see Table IX). The 'Sobrino' and the 'SEBAL' approaches showed highest deviations. The method of Norman et al. (1995) was only applicable on rural pixels, so only 2 points were available for comparison. However, these two points didn't compare well, are not shown in Table IX and also not subject to further analysis. Table IX shows the *MAD*s of Q_s.

Spatial analysis showed that most, but not all, approaches were in agreement with the general assumed spatial pattern with agricultural pixels having the lowest Q_s and urban pixels featuring the highest values. The desert pixels range somewhere in between. Exceptions were the 'Choudhury' approach, where the mean of all urban and the mean of all agricultural pixels equalled more or less. The 'Parlow/urban' approach showed another pattern in 3 scenes only: here the means of the urban and the means of the desert pixels were similar. The 'Sobrino' and the 'Parlow/rural' approaches in turn overestimated the agricultural Q_s, so that the mean of the agricultural pixels almost equalled the mean of the desert pixels. 'SEBAL' finally produced very similar Q_s for all three land use classes.

Table IX MAD of the soil heat flux, option 'best fit'

	MAD [Wm^{-2}]	*MAD* [%]	*MAD* [Wm^{-2}] single stations		
			Urban	Agriculture	Desert
'Parlow/urban'	15.47	18.90	27.42	8.44	10.02
'Frey / *NDVI*'	17.53	21.42	24.07	13.69	14.54
'Frey / land use'	18.97	23.18	35.50	12.37	9.87
'Choudhury'	21.28	26.01	25.02	41.59	8.33
'Sobrino'	38.01	46.45	46.93	45.66	27.49
'SEBAL'	47.64	58.23	53.99	27.87	52.76
'Parlow/rural'	47.71	58.31	44.34	31.09	58.54

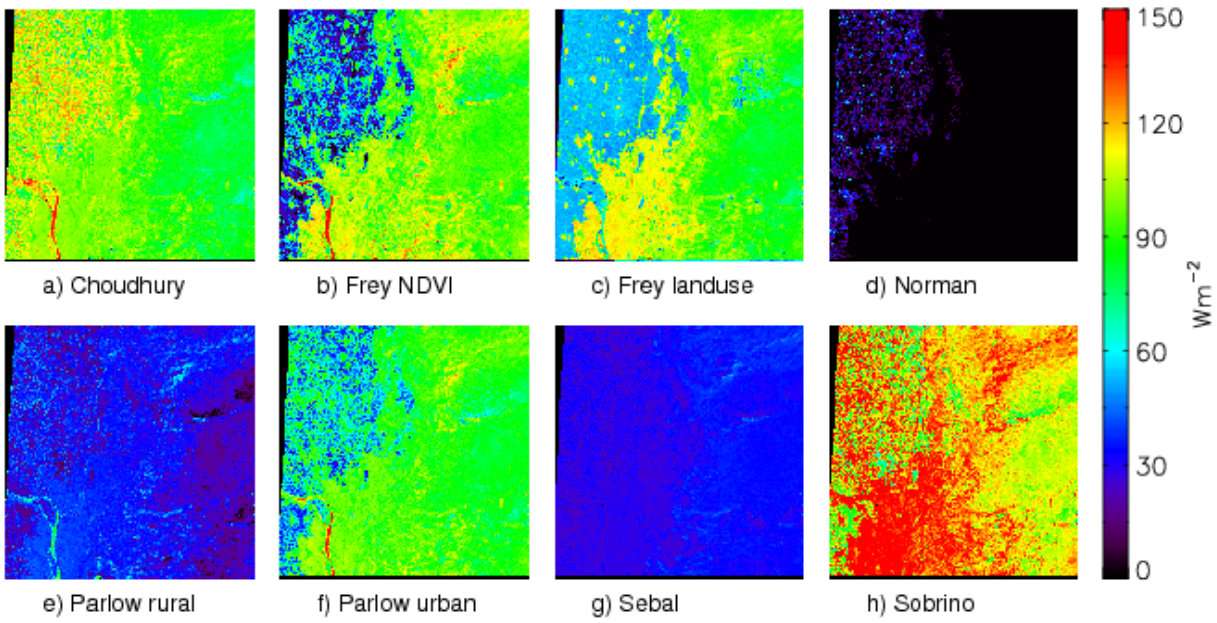

Figure 19 Soil heat flux on 24 December 2007

Differences were found not only in the scaling between the classes but also in the absolute amount. 'Parlow/rural' and 'SEBAL' gave generally too low values. 'Choudhury' and 'Sobrino' showed a very strong dependence on the vegetation density. So many rural pixels still had relatively high Q_s. Only the pixels with very dense vegetation showed lower values, which explains the above mentioned high soil heat flux of the agricultural pixels of the 'Choudhury' approach. The three other approaches ('Parlow/urban' and our new approaches) rendered the most comprehensible images. Figure 19 shows the sample from the scene (b) on 24 December 2007. The left part of the image shows the Nile delta with agricultural lands, rural settlements and the city of Cairo being situated in the lower left corner. The right part of the image is covered by desert. The values of the River Nile are probably not realistic, as no special algorithm for water was used.

2.2.6.3 LUMPS

For the urban station, three value pairs of each turbulent heat flux were available for comparison, the agricultural station had only one pair, and the desert station also had three pairs. For simplicity, the agricultural pair is also addressed as *MAD* in the further analysis.

The parameters from Grimmond & Oke (2002) produced fairly good Q_H and acceptable Q_{LE} at the desert station. Assuming Q_s to equal the in situ measured Q_s (at the urban station in situ derived) and using the 'best fit' option for Q*, the *MAD* of Q_H and Q_{LE} was 6.0 Wm^{-2}, and 16.8 Wm^{-2} respectively, without using a footprint model. The parameters retrieved from the campaign in Cairo produced very similar good results. This good fit is mainly due to the simple environment at the desert station, facilitating the model development. At the urban and the agricultural station, higher deviations of 68.8 Wm^{-2} and 89.0 Wm^{-2} for Q_H and 59.8 Wm^{-2} and 117.9 Wm^{-2} for Q_{LE} were observed for the same setting taking the parameters from Grimmond & Oke (2002). The deviation of the agricultural station is extreme, even though the best fitting value for α proposed by Grimmond & Oke (2002) (α =1.2) was taken. Higher α-values would be for large lakes or oceans; under the condition that β is set to 20.

The parameters derived from the measurement data of course performed much better for both the urban and the agricultural station. *MAD* of Q_H from the 'sectoral' approach of the urban station was 26.9 Wm^{-2}, of the agricultural station 0.6 Wm^{-2} and of the desert station 4.9 Wm^{-2} in case no footprint model was used. The respective values of Q_{LE} are 21.3 Wm^{-2}, 28.3 Wm^{-2}, and 16.1 Wm^{-2}. No significant differences between the 'sectoral' approach and the 'all directions' approach was found, except for the agricultural value. This general good agreement is naturally given, as the parameters were derived from exactly these stations. Strictly speaking only the comparison with the parameters from Grimmond & Oke (2002) is a true validation.

When adding the remotely sensed Q_s to the LUMPS calculations, the results worsened slightly due to the additional source of error in the calculation of Q_s. However, in some cases also the fit was improved as errors tend to cancel out each other. For example, the *MAD* of the urban station of Q_H was only 9.7 Wm^{-2} (compared to 21.4 Wm^{-2}) when taking Q_s from 'Sobrino' and the 'all directions' approach. In the case of the desert station, the *MAD* would not change whatever was the remote sensing Q_s. The 'sectoral' approach mostly increased the *MAD* in case of the urban station compared to the 'all direction' approach when using remote sensed soil heat fluxes, while the *MAD* values of the agricultural and the desert station were mixed. These results were found for all remote sensing methods.

The *MAD* naturally increased more, when not using the 'best fit' option, but the 'best guess' option for the net radiation input in the calculations. By assuming that the best method for Q_s is 'Parlow/urban' and by taking the parameters from Grimmond & Oke (2002) we

obtain the fluxes which correspond to a 'best guess' option. The *MAD*s for the urban, the agricultural and the desert station were 68.1 Wm^{-2}, 82.0 Wm^{-2} and 25.2 Wm^{-2} for Q_H and 59.7 Wm^{-2}, 119.3 Wm^{-2}, and 16.4 Wm^{-2} for Q_{LE}. From these results we can see that it is fairly reasonable to model turbulent heat fluxes in desert-like environments from values in the literature, but it is more critical to do so in urban or suburban environments.

To evaluate the performance of the LUMPS approach in depth, the KM, the H and the HS footprint model were applied to the results of the approach. This procedure is somewhat erroneous for the campaign parameters, as α and β needed by the LUMPS scheme were retrieved from the in situ measurements which already include the flux footprint. The 'sectoral' approach accounted for this problem by deriving more surface-specific parameters from the measurements. However, no better parameters are at hand up to date. Due to cloudiness not all values could be used in the footprint analyses. There was a limitation in the calculation, that at least 70% of the accumulated flux footprint must be cloud free, otherwise the result was invalid. This led to the fact, that the agricultural station had no valid values for the H footprint model.

The use of the footprint models only partly improved the results. In many cases, the results were worsened. The *MAD* of the desert station increased in all cases for Q_H, except for the 'best guess' cases, and decreased only very slightly for Q_{LE} in all cases. The Q_H and Q_{LE} *MAD* values of the agricultural station were sometimes improved sometimes degraded, without logical order. At the urban station the *MAD* of Q_H improved substantially in case the in situ soil heat flux (as residual) was taken (from 27.5 Wm^{-2} in case of the 'all direction' approach to 18.2 Wm^{-2}, 16.6 Wm^{-2}, and 17.7 Wm^{-2} respectively for the KM, the H and the C model). But using a remotely sensed soil heat flux would increase the *MAD* of Q_H again in most cases. Q_{LE} did not improve in almost all cases. Overall, the effect of the footprint models was ambiguous. Results sometimes improved in case of the 'best guess' option, but no direct benefit could be proven. Figure 20 and Figure 21 show the *MAD* of Q_H and Q_{LE} for all calculated combinations.

Summarizing the LUMPS results, we conclude that the estimation of the turbulent heat fluxes from remote sensing data is only applicable, when the environment is fairly simple, like our desert example. As soon as the environment becomes more complex the determination is more difficult due to the uncertainty of the correct input parameters. The correct estimation of the radiation balance was already discussed and this problem propagates to the LUMPS approach.

This discussion neglects the problem of the imprecise determination of the turbulent fluxes by eddy covariance measurements. Especially in inhomogeneous areas, the onsite flux determination is difficult, but also at our desert station the measured energy balance had to be closed by force. Before closing, midday ensemble average of the residual term from the desert station was nearly 60 Wm^{-2}; at the agricultural station it almost reached 150 Wm^{-2}. Similar residuals were found by Moderow et al. (2009) or Wilson et al. (2002). Having these magnitudes of closure gaps in mind, the results of the remote sensing fluxes do actually compare quite well.

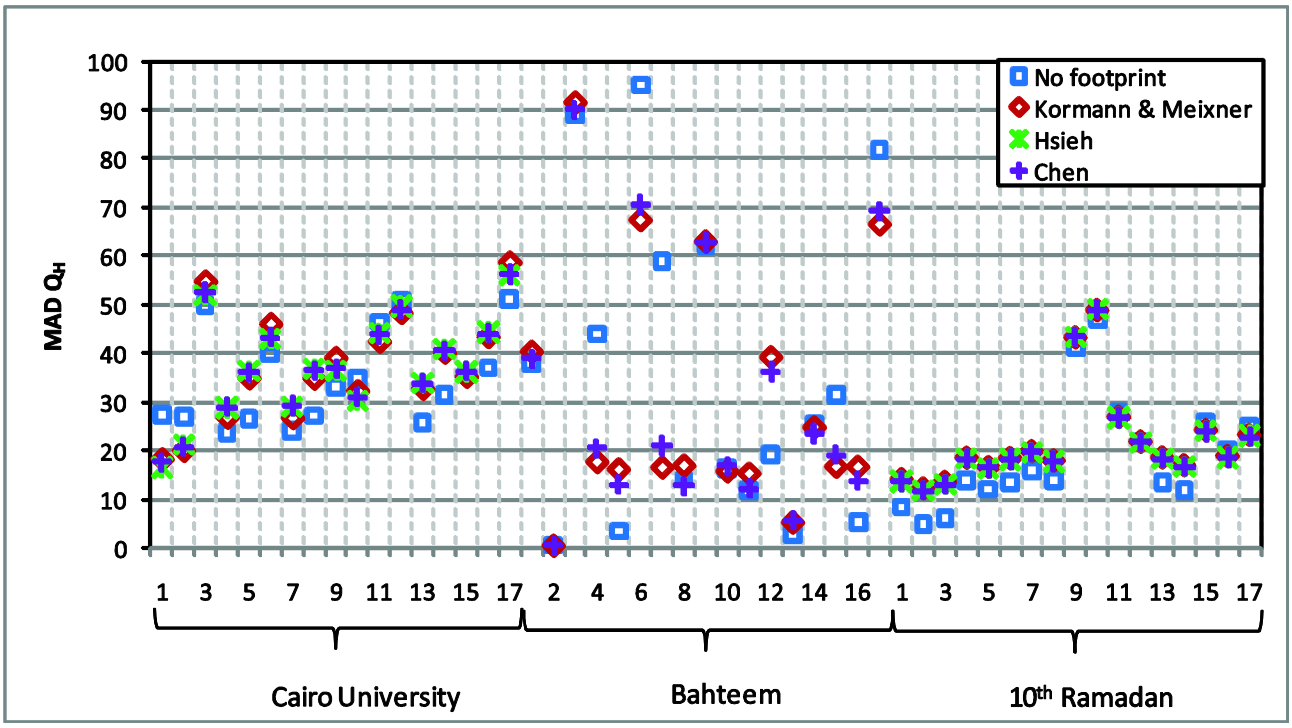

Figure 20 MAD of Q_H [Wm^{-2}] for the different methods of soil heat flux (Q_s), parameters for the LUMPS scheme and atmospheric correction option (for the legend see Table X). MADs are given for simple pixel comparison as well as for the usage of the footprint models.

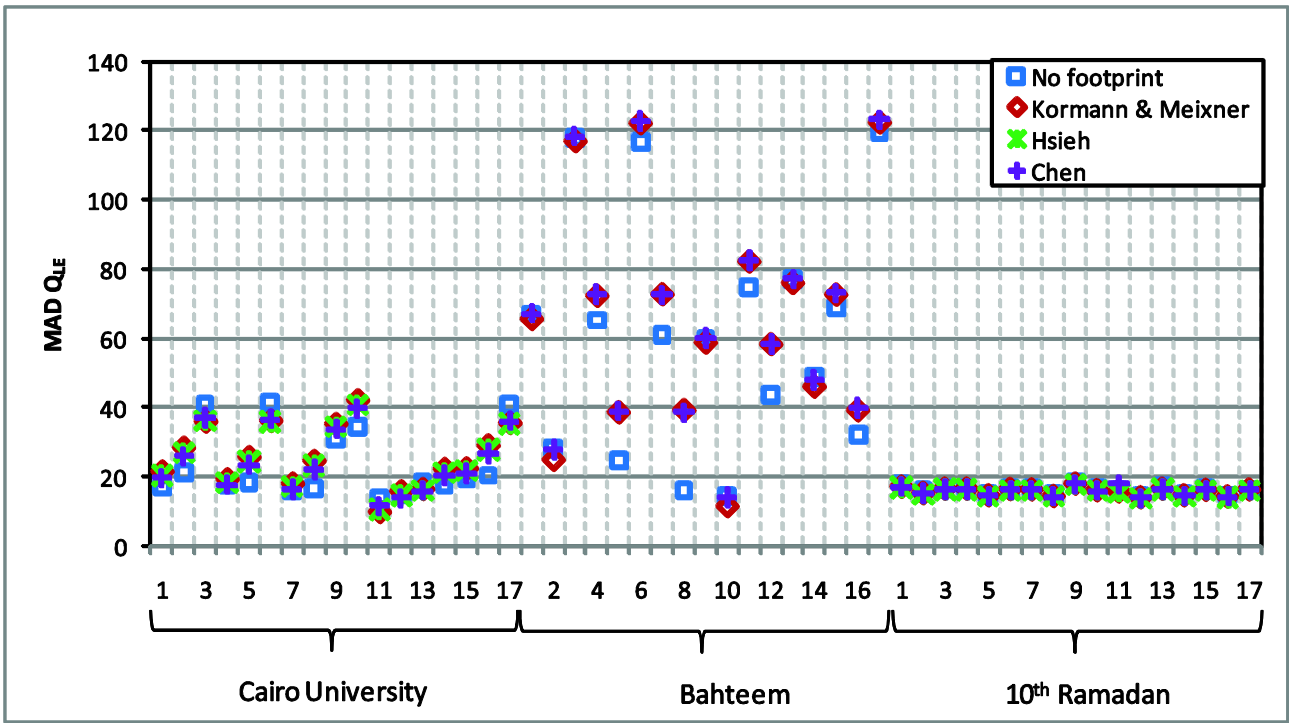

Figure 21 MAD of Q_{LE} [Wm^{-2}] for the different methods of soil heat flux (Q_s), parameters for the LUMPS scheme and atmospheric correction option (for the legend see Table X). MADs are given for simple pixel comparison as well as for the usage of the footprint models.

Table X Annotations for Figure 20 and Figure 21

Nr.	Soil heat flux	LUMPS parameter	Atmospheric correction
1	In situ	Frey / all directions	best fit
2	In situ	Frey / sectoral	best fit
3	In situ	Grimmond	best fit
4	Parlow	Frey / all directions	best fit
5	Parlow	Frey / sectoral	best fit
6	Parlow	Grimmond	best fit
7	Frey / *NDVI*	Frey / all directions	best fit
8	Frey / *NDVI*	Frey / sectoral	best fit
9	Sebal	Frey / all directions	best fit
10	Sebal	Frey / sectoral	best fit
11	Sobrino	Frey / all directions	best fit
12	Sobrino	Frey / sectoral	best fit
13	Choudhury	Frey / all directions	best fit
14	Choudhury	Frey / sectoral	best fit
15	Parlow	Frey / all directions	best guess
16	Parlow	Frey / sectoral	best guess
17	Parlow	Grimmond	best guess

Spatial analysis of the LUMPS heat fluxes showed that the different approaches produced fairly different patterns. Following Frey et al. (2010) it was assumed, that the sensible heat flux should be highest in desert areas, closely followed by urban areas and be lowest over agricultural fields. The latent heat flux however should be highest over the agricultural fields, followed by the urban areas and be lowest in the desert areas. This pattern was only partly fulfilled by the LUMPS approaches. The latent heat flux was modelled fairly in accordance with this pattern in almost all cases. Only the approaches using the parameters of Grimmond & Oke (2002) rendered urban Q_{LE} which were lower than the desert Q_{LE}. Figure 22 b) shows Q_{LE} modelled using the 'Frey/*NDVI*' Q_s and the 'all direction' approach for the LUMPS parameters.

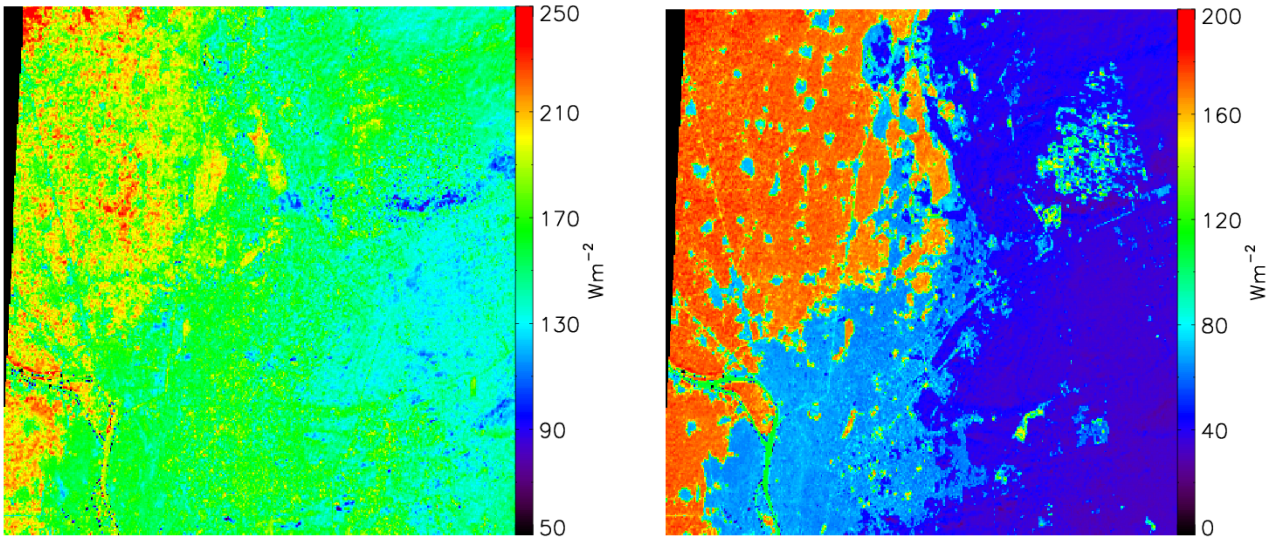

Figure 22 Q_H (left) and Q_{LE} (right) modelled using the 'Frey / NDVI' Q_s and the all-direction approach for the LUMPS parameters from 24.12.2007

All LUMPS approaches estimated a very low Q_H in the desert. Almost half of the different LUMPS method combinations rendered a desert Q_H which was much lower than the urban Q_H which is probably not realistic. As mentioned before, Q_{LE} was modelled quite well. This is attributed to the fact, that the LUMPS parameters α and β deducted from the in situ measured values were retrieved for equation (26), which estimates Q_{LE}. Q_H in equation (27) then uses the same parameters. Due to the structure of the formula, it is not possible to retrieve α and β for equation (26).

Looking at the Bowen ratio β (=Q_H/Q_{LE}), most methods assigned the desert the highest β values, the urban areas slightly lower and the agricultural areas the lowest β. The methods including the 'sectoral' approach gave the most reasonable results. Mean desert β thereby were found in the range $7 < \beta > 5$, agricultural areas featured $3 < \beta > 0.5$ and urban areas $3 < \beta > 1$ including all available dates and method combinations. The parameters from the literature however rendered extremely high urban β ($28 < \beta > 10$) and also very high agricultural values ($\beta \approx 3$).

Due to the accumulated uncertainties of the input terms Q^* and Q_s in LUMPS, it is difficult to decide from this dataset whether wrong flux estimates are due to a failure of the LUMPS approach or due to incorrect input data.

2.2.6.4 ARM

Q_{LE} estimated with the ARM method was calculated firstly with the in situ measured values for Q_s and secondly with the 'Parlow/urban' Q_s. According to equation (28), Q_H is independent of Q_s. Generally, *MAD* of Q_H and Q_{LE} of the ARM method were higher than the *MAD* of the LUMPS approach. Especially at the desert station the agreement worsened. Only the agricultural *MAD* was better with the ARM method. *MAD* of Q_H for the urban, the agricultural and the desert station were 41.2 Wm^{-2}, 7.85 Wm^{-2} and 31.1 Wm^{-2} for the 'best fit' option. At the urban station the 'best guess' option of Q_{LE} performed better than the 'best fit' option (16.0 Wm^{-2} versus 41.3 Wm^{-2} with the in situ measured Q_s and 29.9 Wm^{-2} versus 41.2 Wm^{-2} with the 'Parlow/urban' approach). However, at the agricultural and the desert station the 'best fit' approach performed better for both the in situ and the 'Parlow/urban' approach ('best fit': 28.8 Wm^{-2} / 34.1 Wm^{-2} and 40.2 Wm^{-2} / 34.7 Wm^{-2}). The use of the approach of 'Parlow/urban' instead of the in situ values increased the *MAD* only at the agricultural station. At the urban station, it did not alter the *MAD* and at the desert station it even decreased the *MAD*. Using the method of Xu et al. (2008) for the estimation of air temperature, *MAD* increased in some cases, but also decreased in other cases, for example for the agricultural pixels.

Spatial analysis of the ARM heat fluxes followed the same rules as in the LUMPS analysis. Q_{LE} was modelled correctly, with the agricultural Q_{LE} the highest; the desert Q_{LE} the lowest and the urban Q_{LE} somewhere in between. Still, the 'best fit' option with using T_a according to Xu et al. (2008)'s formula produced desert Q_{LE} almost as high as the urban Q_{LE}. Q_H was modelled correctly at most dates when using T_a deduced with the empirical equations from the campaign, but rendered too low desert Q_H and almost equal means of urban and agricultural Q_H in case, Xu et al. (2008)'s formula was taken. Figure 23 shows Q_H and Q_{LE} for the 'best fit' option and the 'Parlow / urban' Q_s.

The analysis of the Bowen ratios β showed, that also most methods assigned the desert β highest values, the urban areas slightly lower β and the agricultural areas the lowest. However, in some cases the desert had a negative latent heat flux, resulting in negative β values. The method combination using Xu et al. (2008)'s formula did not perform well also in this analysis of the Bowen ratios.

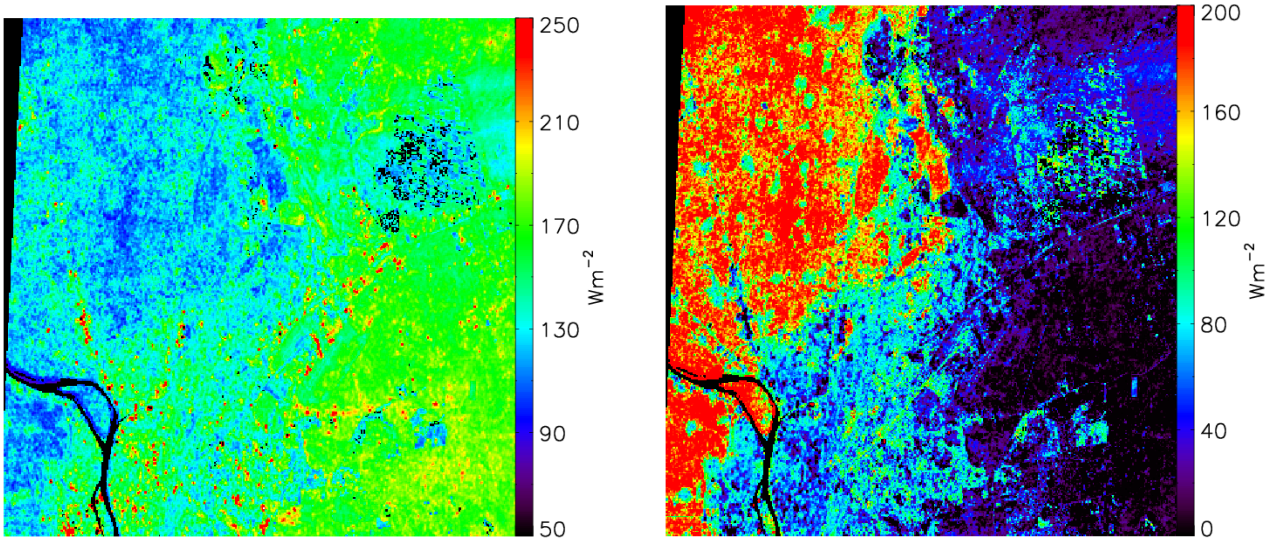

Figure 23 ARM heat fluxes. a) Q_H and b) Q_{LE} modeled using the 'Parlow / urban' Q_s from 24.12.2007

2.2.7 Conclusions

The estimation of the radiation and energy balance from satellite images strongly depends on a successful atmospheric correction. Especially in areas, where the aerosol content of the troposphere is not constant (for example due to air pollution as in our research area), the atmospheric correction is a crucial task. Here, the albedo is estimated with a 15.4% accuracy in the 'best guess' scenario. Shortwave irradiation was estimated with 8.5%, longwave emission with 2.0%, incoming longwave radiation with 6.5%, and finally the net radiation with 11.6% accuracy. The 'best fit' case improved these values considerably. Considering the conservative estimation of an accuracy of in situ measurements of 10%, achieved percentages are quite good. However, in a single case at the desert station the solar irradiation was underestimated about 99.6 Wm^{-2} (scene (a) of 22 November 2007) due to an inappropriate value of a MISR *AOD* product pixel. *Q** then was underestimated 111.2 Wm^{-2}. In the LUMPS approach this produced a difference to the 'best fit' option in Q_H of 31.1 Wm^{-2} taking the campaign retrieved parameters and the Q_s of 'Parlow/urban'. The difference in Q_{LE} with the same input is only 4.7 Wm^{-2}. Using the ARM approach the difference between this 'best guess' option and the 'best fit' option is 35.7 Wm^{-2} for Q_{LE}. Dealing with such magnitudes it is difficult to decide whether a spatial pattern is mainly governed by land use or due to incorrect atmospheric correction.

In any case, the soil heat flux could be modelled satisfactorily with three different approaches when comparing the values to 30 minute averages. Direct comparison to 1 minute averages would render extreme differences. This is because the storage heat flux as part of the soil heat flux showed extreme deviations due to short-time fluctuations of the surface temperature. Such high fluctuations can never be explained by the net radiation and vegetation indices only. From the existing approaches only the 'Parlow/urban' approach rendered proper values. Further two new empiric approaches gave good results. Their transferability to other regions however must be proven in future studies.

All in all 17 possible methodological combinations were used to calculate Q_H and Q_{LE} with the LUMPS approach. Combinations included the 'best guess' and the 'best fit' option of Q*, different approaches for α and β, and various sources for the ground heat flux. Each

combination was further input in the three used footprint models, resulting in 68 combinations. Overall *MAD* of Q_H of the urban station was 40 Wm^{-2} which is 21% of the mean in situ measured flux. At the agricultural station the overall *MAD* was 33 Wm^{-2} (28%) and at the desert station it was 21 Wm^{-2} (14%). The respective values for Q_{LE} were 28 Wm^{-2} (58%), 65 Wm^{-2} (35%) and 16 Wm^{-2} (63%). The desert station showed the best results due to its simple and homogeneous environment. The agricultural station on the contrary showed the highest deviations, which resulted probably from the high fragmentation of the landscape. The urban station was somewhere in between. Considering the uncertainty of the in situ measurements these results are quite acceptable. Single combinations showed differing results, with generally the 'best fit' option improving the *MAD* and the empirical estimated α and β delivering better results than the values from literature. Taking the spatial analysis into consideration the 'sectoral' approach for the estimation of α and β in combination with a ground heat flux from 'Parlow/urban' or the two own approaches performed the best.

The application of the footprint models increased the *MAD* in most cases. It is therefore not encouraged to use such models when working with high uncertainties. Spatial analysis showed that not all combinations rendered acceptable pattern. While Q_{LE} was modelled quite well in almost all cases, Q_H seemed to be overestimated over agricultural areas and underestimated in the desert.

The LUMPS approach is somehow promising as it is fast and simple. However, the determination of the parameter α and β is difficult. Values from literature are only partly applicable, so better values must be retrieved empirically. However, the number of reference stations in this study was very limited; therefore the retrieved values were not fully representative for the whole scene. It is strongly encouraged, that further work in the estimation of these parameters is pursued. Grimmond & Oke (2002) started already to depend α on the surface cover (fraction of vegetated and irrigated areas). More work in this direction should be done for different urban and non-urban surfaces. In future studies α and β should be modelled in dependence on the surface characteristics (housing density and vegetation cover, irrigation). Taking only fixed values makes it difficult to represent the actual flux distribution.

The ARM approach was calculated with six different combinations, while Q_H was only affected from two combinations. Additionally add also the foot print models. The combinations were the 'best guess' and 'best fit' options of Q*, the source of the ground heat flux and the modelling of the air temperature. Overall *MAD* of Q_H of the urban station was 49 Wm^{-2} which is 26% of the mean in situ measured flux. At the agricultural station the overall *MAD* was 10 Wm^{-2} (8.6%) and at the desert station it was 52 Wm^{-2} (33%). The respective values for Q_{LE} were 45 Wm^{-2} (93%), 46 Wm^{-2} (25%) and 49 Wm^{-2} (215%). The percentages for the latent heat flux at the urban and the desert station are therefore extremely high, as the latent heat flux is generally very low. Altogether similar results to the LUMPS analysis were found. 'Best fit' worked better than the 'best guess' option and the use of a remote sensing ground heat flux increased the *MAD* due to the additional source of uncertainty. The application of the footprint model worsened the results. The estimation of air temperature with the formula from Xu et al. (2008) decreased the accuracy slightly compared to our own regression equation. Spatial analysis showed that the ARM approaches were able to reproduce spatially distributed fluxes, with the exception of the approach with Xu et al. (2008) formula.

Due to a high range of surface temperatures in desert areas, no representative surface temperature for a given albedo could be determined. Therefore the S-SEBI approach is not suitable in this environment and was not used to calculate surface fluxes for the area.

2.2.8 Acknowledgements

This work was supported by the Swiss National Science Foundation (grant number 200020–120080/1).

2.2.9 References

Bastiaanssen WGM, Menenti M, Feddes RA, Holtslag AAM. 1998. A remote sensing surface energy balance algorithm for land (SEBAL). 1. Formulation. *Journal of Hydrology* **212–213**: 198–212.

Bastiaanssen WGM, Noordman EJM, Pelgrum H, Davids G, Thoreson BT, Allen RG. 2005. SEBAL Model with Remotely Sensed Data to Improve Water-Resources Management under Actual Field Conditions. *Journal of Irrigation and Drainage Engineering* **131(1)**: 85–93.

Blumberg DG, Greeley R. 1993. Field studies of aerodynamic roughness length. *Journal of Arid Environments* **25**: 39–48

Carlson TN, Ripley DA. 1997. On the relation between *NDVI*, fractional vegetation cover and leaf area index. *Remote Sensing and Environment* **62**:241–252.

Chen B, Black TA, Coops NC, Hilker T, Trofymow JAT, Morgenstern K. 2009. Assessing tower flux footprint climatology and scaling between remotely sensed and eddy covariance measurements. *Boundary-Layer Meteorology* **130**: 137–167.

Choudhury BJ, Idso SB, Reginato RJ. 1987. Analysis of an empirical model for soil heat flux under a growing wheat crop for estimating evaporation by an infrared-temperature based energy balance equation. *Agricultural and Forest Meteorology* **39**: 283−297.

de Bruin HAR, Holtslag AAM. 1982: A simple parameterization of surface fluxes of sensible and latent heat during daytime compared with the Penman-Monteith concept. *Journal of Applied Meteorology* **21**: 1610–1621.

De Ridder K, Mensink C. 2003. Surface fluxes and atmospheric stability obtained from a surface energy balance model with parameters estimated from satellite remote sensing. *International Journal of Environment and Pollution* **19(1)**: 22–31.

Foken T. 2008. The energy balance closure problem: an overview. *Ecological Applications* **18(6)**: 1351–1367.

Frey CM, Parlow E. 2009. Geometry effect on the estimation of band reflectance in an urban area. *Theoretical and Applied Climatology* **96**: 395–406.

Frey CM, Parlow E, Vogt R, Abdel Wahab M, Harhash M. 2010. Flux measurements in Cairo. Part 1: In situ measurements and their applicability for comparison with satellite data. *International Journal of Climatology*. Accepted and published online.

Gowda PH, Chávez JL, Colaizzi PD, Evett SR, Howell TA, Tolk JA. 2007. Remote sensing based energy balance algorithms for mapping ET: current status and future challenges, *Transactions of the ASABE* **50(5)**: 1639–1644.

Greeley R, Blumberg DG, McHone JF, Dobrovolskis A, Iversen JD, Lancaster N, Rasmussen KR, Wall SD, White BR. 1997. Applications of spaceborne radar laboratory data to the study of aeolian processes. *Journal of Geophysical Research* **102(E5)**: 10,971–10,983.

Grimmond CSB, Oke TR. 1999. Aerodynamic properties of urban areas derived from analysis of surface form. *Journal of Applied Meteorology* **38**: 1262−1292.

Grimmond CSB, Oke TR. 2002. Turbulent heat fluxes in urban areas: Observations and a local-scale urban meteorological parameterization scheme (LUMPS). *Journal of Applied Meteorology and Climatology* **41(7)**: 792–810.

Hsieh CI, G Katul, T Chi. 2000. An Approximate Analytical Model for Footprint Estimation of Scalar Fluxes in Thermally Stratified Atmospheric Flows. *Advances in Water Resources* **23**: 765−772.

Holtslag AAM, AP van Ulden. 1983. A simple scheme for daytime estimates of the surface fluxes from routine weather data. *Journal of Climate and Applied Meteorol*ogy **22**: 517–529.

Kaufman YJ, Tanré D, Remer LA, Vermote EF, Chu A, Holben BN. 1997. Operational remote sensing of tropospheric aerosol over land from EOS moderate resolution imaging spectro-radiometer. *Journal of Geophysical Research* **102**: 17 051–17 068.

Keller J, Bojinski S, Prevot ASH. 2007. Simultaneous retrieval of aerosol and surface optical properties using data of the Multi-angle Imaging SpectroRadiometer (MISR). *Remote Sensing of Environment* **107**: 120–137.

Kormann R, Meixner FX. 2001. An analytic footprint model for neutral stratification. *Boundary-Layer Meteorology* **99**: 207–224.

Kustas WP, Choudhury BJ, Moran MS, Reginato RJ, Jackson RD, Gay LW, Weaver HL. 1989. Determination of sensible heat flux over sparse canopy using thermal infrared data. *Agricultural and Forest Meteorology* **44**: 197–216.

Kustas WP, Daughtry CST. 1990: Estimation of the soil heat flux/net radiation from spectral data. *Agricultural and Forest Meteorology* **49**: 405–223.

Li F, Kustas WP, Anderson MC, Prueger JH, Scott RL. 2008. Effect of remote sensing spatial resolution on interpreting tower-based flux observations. *Remote Sensing of Environment* **112 (2)**: 337–349.

Liang S. 2004. *Quantitative Remote Sensing of Land Surfaces*. Wiley Series in Remote Sensing.-(Series Editor): Jin Au Kong. Hoboken, New Jersey: 534

Liu BYH, Jordan RC. 1963. The long-term average performance of flatplate solar energy collectors. *Solar Energy* **7**: 53.

Martonchik JV, Diner DJ, Kahn RA, Ackerman TP, Verstraete MM, Pinty B, Gordon HR. 1998. Techniques for the Retrieval of Aerosol Properties Over Land and Ocean Using Multiangle Imaging. *IEEE Transactions on Geoscience and Remote Sensing* **36(4)**: 1212–1227.

Menenti M, Choudhury BJ. 1993. Parameterization of land surface evaporation using a location dependent potential evaporation and surface temperature range. In: H.J. Bolle *et al. Exchange Processes at the Land Surface for a Range of Space and Time Scales. IAHS Publication* **21:** 561–568.

Moderow U, Aubinet M, Feigenwinter C, Kolle O, Lindroth A, Mölder M, Montagnani L, Rebmann C, Bernhofer C. 2009. Available energy and energy balance closure at four coniferous forest sites across Europe. *Theoretical and Applied Climatology* **98**: 397–412.

Monteith JL, Unsworth MH. 1990. Principles of environmental physics, 2nd ed. Edward Arnold, London, United Kingdom.

Neftel A, Spirig C, Ammann C. 2008. Application and test of a simple tool for operational footprint evaluations. *Environmental Pollution* **152**: 644–652.

Norman JM, Kustas WP, Humes KS. 1995. Source approach for estimating soil and vegetation energy fluxes in observations of directional radiometric surface temperatures. *Agricultural and Forest Meteorology* **77(3–4)**: 263–293. (Erratum: *Agricultural and Forest Meteorology* **80(2–4)**: 297.

Offerle BD. 2003. The energy balance of an urban area: examining temporal and spatial variability through measurements, remote sensing and modelling, *PhD*, Indiana University, Bloomington USA.

Pasquill F, Smith FB. 1983: Atmospheric Diffusion. 3rd edn. Wiley, New York, 437.

Prigent C, Tegen I, Aires F, Marticorena B, Zribi M. 2005. Estimation of the aerodynamic roughness length in arid and semi-arid regions over the globe with the ERS scatterometer. *Journal of Geophysical Research* **110(D09205)**: 1–12.

Qi J, Chehbouni A, Huete AR, Kerr YH, Sorooshian S. 1994. A modified soil adjusted vegetation index. *Remote Sensing of Environment* **48(2)**: 119–126.

Rigo G. 2007. Satellite analysis of radiation and heat fluxes during the Basel Urban Boundary Layer Experiment (BUBBLE). *PhD*. University of Basel, Switzerland

Rigo G, Parlow E. 2006. Modelling the ground heat flux of an urban area with remote sensing data. *Theoretical and Applied Climatology* **90(3–4)**: 185–199.

Roerink GJ, Su Z, Menenti M. 2000. S-SEBI: A simple remote sensing algorithm to estimate the surface energy balance. *Physics and Chemistry of the Earth, Part B: Hydrology, Oceans and Atmosphere* **25(2)**: 147–157.

Schlink U, Rehwagen M, Richter M, Herbarth O. 2007. Environmental security in urban areas. Health-relevant VOC exposure in the Greater Cairo Area, Egypt. In: Linkov I, Wenning RJ, Kiker GA (eds.), Managing critical infrastructure risks: decision tools and applications for port security. Springer, Dordrecht: 423–434.

Sobrino JA, Gómes M, Jiménez-Muñoz JC, Olioso A, Chehbouni G. 2005. A simple algorithm to estimate evapotranspiration from DAIS data: Application to the DAISEX campaigns. *Journal of Hydrology* **315(1–4)**: 117–125.

Su Z. 2002. The surface energy balance system (SEBS) for estimation of turbulent heat fluxes. *Hydrology and Earth System Sciences* **6(1)**: 85–99.

Twine TE, Kustas WP, Norman JM, Cook DR, Houser PR, Meyers TP, Prueger JH, Starks PJ, Wesely ML. 2000. Correcting eddy-covariance flux underestimates over a grassland. *Agricultural and Forest Meteorology* **103(3)**: 279–300.

van Ulden AP. 1978. Simple estimates for vertical diffusion from sources near the ground. *Atmospheric Environment* **12**: 2125–2129.

Voogt, J.A. and C.S.B. Grimmond, 2000. Modelling surface sensible heat flux using surface radiative temperatures in a simple urban area. *Journal of Applied Meteorology* **39**, 1679–1699.

Verma SB. 1989. Aerodynamic resistances to transfers of heat, mass and momentum. Estimation of Areal Evapotranspiration. - Black TA, Spittlehouse DL, Novak MD, Price DT (Eds.), *International Association of Hydrological Sciences* **177**: 13–20.

Wilson K, Goldstein A, Falge E, Aubinet M, Baldocchi D, Berbigier P, Bernhofer C, Ceulemanns R, Dolman H, Field C, Grelle A, Ibrom A, Law BE, Kowalski A, Meyers T, Moncrieff J, Monson R, Oechel W, Tenhunen J, Valentini R, Verma S. 2002. Energy balance closure at FLUXNET sites. *Agricultural and Forest Meteorology* **113(1–4)**: 223–243.

Xu W, MJ Wooster, CSB Grimmond 2008: Modelling of urban sensible heat flux at multiple spatial scales: a demonstration using airborne hyperspectral imagery of Shanghai and a temperature-emissivity separation approach. *Remote Sensing of the Environment* **112**: 3493–3510.

Annex

The regression equations for the broadband albedo are:

$$\alpha = 0.001 + \alpha_{b1}\cdot 0.221 + \alpha_{b2}\cdot 0.174 + \alpha_{b3}\cdot 0.265 + \alpha_{b4}\cdot 0.295 + \alpha_{b5}\cdot(-0.514) + \alpha_{b6}\cdot 0.504 + \alpha_{b7}\cdot 0.066 + \alpha_{b8}\cdot(-0.074) + \alpha_{b9}\cdot 0.015 \quad (33)$$

$$\alpha = 0.035 + \alpha_{b1}\cdot 0.132 + \alpha_{b2}\cdot 0.101 + \alpha_{b3}\cdot 0.637 \quad (34)$$

The equations for the broadband emissivity for the different land use classes are:

Desert:

$$\varepsilon = 0.287 + \varepsilon_{b10}*(0.175) + \varepsilon_{b11}*(-0.080) + \varepsilon_{b12}*(0.068) + \varepsilon_{b13}*(0.541) \quad (35)$$

Vegetation:

$$\varepsilon = 0.001 + \varepsilon_{b10}*(0.091) + \varepsilon_{b11}*(-0.023) + \varepsilon_{b12}*(0.349) + \varepsilon_{b13}*(0.584) \quad (36)$$

Water:

$$\varepsilon = -0.470 + \varepsilon_{b10}*(0.416) + \varepsilon_{b11}*(0.815) + \varepsilon_{b12}*(-0.452) + \varepsilon_{b13}*(0.163) + \varepsilon_{b14}*(0.529) \quad (37)$$

Urban:

$$\varepsilon = 0.486 + \varepsilon_{b11}*(0.026) + \varepsilon_{b12}*(0.091) + \varepsilon_{b13}*(0.374) \quad (38)$$

The regression equations for estimation of spatial air temperature are:

$$T_{s\ urban} = 0.697\cdot T_a - 0.632\cdot wnd_{spd} + 0.588 \qquad r^2 = 0.83 \quad (39)$$

$$T_{s\ agri} = 0.575\cdot T_a - 0.277\cdot wnd_{spd} + 2.482 \qquad r^2 = 0.71 \quad (40)$$

$$T_{s\ desert} = 0.601\cdot T_a - 0.420\cdot wnd_{spd} + 1.657 \qquad r^2 = 0.77 \quad (41)$$

Table XI *Γ* values for the calculation of the sinus curve

Hour	*Γ*	Hour	*Γ*
07:00	0.000	12:00	1.396
07:30	0.175	12:30	1.222
08:00	0.349	13:00	1.047
08:30	0.524	13:30	0.873
09:00	0.698	14:00	0.698
09:30	0.873	14:30	0.524
10:00	1.047	15:00	0.349
10:30	1.222	15:30	0.175
11:00	1.396	16:00	0.000
11:30	1.571 (= 90*π/180)		

2.3 Flux measurements in Cairo. Part 3 - CO_2 fluxes and concentrations (co-authoring)

Susanne A. Burri, Roland Vogt, Corinne M. Frey, Eberhard Parlow

Submitted to International Journal of Climatology

ABSTRACT *Fluxes and concentrations of carbon dioxide (CO_2) were measured by the eddy covariance method in the city of Cairo in Egypt from November 2007 until February 2008. The measurements were taken in the framework of the CAPAC project (Cairo Air Pollution And Climate) on the flat roof of a building of Cairo University. Most of earlier CO_2 measurements have been taken in cities of industrial countries in Europe, Northern America or Asia. The current study is of special interest, as it shows results from a city in a less developed country within a semi-arid environment.*

The CO_2 fluxes peaked in a single maximum between 1 and 3 pm, which is different from most previous studies, where often two rush-our peaks (in the morning and in the late afternoon) were observed. Average peak values were around 15 $\mu mol\, m^{-2}s^{-1}$. The CO_2 fluxes showed a distinct weekly cycle, as they were remarkably lower on Fridays (Sabbath in Cairo). The CO_2 concentrations showed the maximum in the morning with average values around 420 ppm. However, the peak values occurred also later than expected (around 8 to 9 am). This delay could be assigned to the diurnal course of stability, as the change from stable to unstable conditions usually happened only at about 8 am. An additional land use-dependent analysis revealed higher CO_2 fluxes over an urban surface (with predominantly buildings and roads with heavy traffic) in the north of the station, compared to a surface with mainly agricultural and sports fields in the south of the station.

2.3.1 Introduction

In 2008, the atmospheric carbon dioxide (CO_2) concentration reached 385.2 ppm (World Meteorological Organization 2009), a level which the atmosphere according to ice core records had not experienced for at least 650'000 years (Denman *et al*., 2007). The main reasons for this increase are the burning of fossil fuels and land use change (deforestation as well as other changes in land use and changes in agricultural practices), and to a smaller part cement production. Thus, humans apparently induce an altering of the natural carbon cycle by speeding up the CO_2 release to the atmosphere. Since an increasing part of the world's population lives in cities, CO_2 emissions of urban areas are large and concentrate on a local to regional scale. However, the urban surface consist of a complex pattern of different surfaces, some of which are CO_2 sources, while others act as CO_2 sinks. Not only the pattern of surfaces is complex, but also the processes governing the CO_2 exchange. The understanding of the dynamics of CO_2 sources and sinks in cities helps quantifying the local to regional CO_2 emissions of urban areas. This is of high importance for the detailed understanding and modelling of the carbon cycle as well as CO_2 budget considerations (Churkina, 2008).

While the surface-atmosphere exchange of CO_2 has been studied for many different natural surfaces, the exchange over urban surfaces has come into focus only in the last years. Grimmond *et al*. (2002) were among the first to measure CO_2 fluxes in urban environments by the eddy covariance method in Chicago in 1995. A number of urban climate studies using the same method followed (Nemitz *et al*. (2002) in Edinburgh, Soegaard and Møller-Jensen (2003) in Copenhagen, Moriwaki and Kanda (2004) in Tokyo, Grimmond *et al*. (2004) in Marseille, Velasco *et al*. (2005) in Mexico City, Vogt *et al*. (2006) in Basel, Moriwaki *et al*. (2006) in Tokyo, Coutts *et al*. (2007) in Melbourne, Vesala *et al*. (2008b) in Helsinki). Obviously, the larger part of the measurements was taken in industrial countries of Europe, North America, Japan or Australia.

The measurements of CO_2 fluxes and concentrations analyzed in this study were taken in the framework of the CAPAC project (Climate and Air Pollution Analysis of Cairo). Cairo is a megacity, whose exact population number is not known, but estimations range between 15 and 20 million people (Ibrahim and Ibrahim, 2006). The critical values of air pollution are highly exceeded (Ibrahim and Ibrahim, 2006), most likely to a large extent induced by the high traffic density and the low technology of cars. The objective of this study was to quantify the CO_2 fluxes and concentrations of Cairo, a highly polluted megacity of a less developed country.

Due to the location of the measurement site, it was possible to divide the surface around the station into different land use sectors resembling the method used by Vesala *et al*. (2008b). Therefore, the aim was also to investigate the influence of different urban surfaces on the CO_2 fluxes and concentrations. A question always kept in mind was if and to what extent vegetated areas were capable of reducing urban CO_2 emissions.

2.3.2 Methods

2.3.2.1 Site description

The measurement site was operated in the district of Giza on the roof of a building of Cairo University (30°01'33.39''N, 31°12'27.81''E). The building density on the campus area of Cairo University is relatively low compared to other very densely populated areas of Cairo. It consists of three- to four-storied buildings, roads and squares, as it is also common on European or American campus areas. For further details on the city of Cairo and on the location of the station see Frey *et al*. (2010).

The neighbourhood of the station varies (Figure 24). To the north and north-west of the station lies the campus area of the university (Figure

25a), while a street with several lanes in both directions and very intensive traffic is located in a distance of about 300 m. Beyond the campus area the building density is considerably higher. To the north-east, also in about 300 m distance, lies another street with heavy traffic. Beyond this street, a large green area, a zoological garden, is located. The area south of the station is dominated by the sports field in the south-east and agricultural fields in the south-west (Figure 25b).

Figure 24 View of the different surfaces surrounding the urban station (2008 Digital Globe. Google Earth).

Figure 25 a) View from the station to the north. b) View from the station to the south-west.

Some of the agricultural fields are botanical test fields of the university. They reach almost a kilometre to the south. The closest street in the west and south-west lies in about 500 to 800 m distance. The selection of the site resulted from a cooperation with Cairo University. It was of course not representative of the whole city, but rather could give an insight into that specific part of the city. While selecting the location of the site, it was not possible to consider only scientific requirements as permission by authorities as well as security issues also played an important role.

2.3.2.2 Instrumentation and data processing

CO_2 fluxes were measured with an open-path gas analyzer (LI-7500, LICOR) and a sonic anemomenter (CSAT3, Campbell) using the eddy covariance method. The instruments were mounted on a 12 m mast on the flat roof of a 15 m high building of Cairo University. The total measurement height was 27 m. The collection of the data began on 10th November 2007 and ended on 26th February 2008 (109 days). Data were sampled at 20 Hz and CO_2 fluxes were derived every 30 min. Fluxes were calculated online, but raw data were also stored on the data logger (CR3000, Campbell). Maintenance of the station was done twice a week. Both the humidity correction for the sensible heat flux (Schotanus *et al*., 1983) and the correction for the upward directed mean wind (Webb *et al*., 1980) were calculated online.

Before data analysis, error values in the CO_2 measurements induced by precipitation or maintenance events (water on the sensor head) were excluded from the data record. Short gaps with a maximum of four missing values in the flux data were interpolated. From 27th January 2008 (17:30) until 3rd February 2008 (18:00), a large data gap occurred due to a malfunction of the eddy covariance system. To do a surface dependent analysis, the data were divided into three land use sectors: a north sector (270-40°, predominantly urban, buildings and roads with

heavy traffic), an east sector (40-135°, mainly zoological garden) and a south sector (135-270°, agricultural fields and sports field). While the difference in land use between the north and the south sector was obvious, it was not that straightforward for the east sector. The latter was mainly chosen in order to investigate a potential influence of the zoological garden (lying at some distance from the station) on the CO_2 fluxes. An overview of data availability for each sector is shown in Table XII. Unfortunately, data availability for the east sector was very low due to infrequent winds blowing from that direction. This somewhat complicated the analysis of the data for the east sector. Interpreting the results in the three defined sectors, the need for estimating the actual size of the source area came up. Thus, a footprint estimation with the one-dimensional model of Hsieh *et al*. (2000), an analytical model based on a Lagrangian stochastic dispersion model, was conducted. The model of Hsieh *et al*. (2000) is more straightforward to apply than many other footprint models. While it is not perfectly applicable to an urban environment, hardly any of the footprint models is (Vesala *et al*. 2008a). The city surface has a high roughness and its land use is very inhomogeneous on a small scale. Therefore footprint models, originally designed for homogeneous conditions, are difficult to apply. The results of this footprint calculation can thus be seen as an estimation, but the uncertainty in the applicability of the model on urban surfaces should be kept in mind.

Table XII Data availability for the corrected CO_2 flux for each defined land use sector

Sector's name	Wind Direction	Description	Relative Frequency
North	270-40°	Predominantly urban, buildings and roads with heavy traffic	58.7%
East	40-135°	Zoological garden	6.2%
South	135-270°	Agricultural fields and sports field	27.2%
Errors			7.8%
Total			100.0%

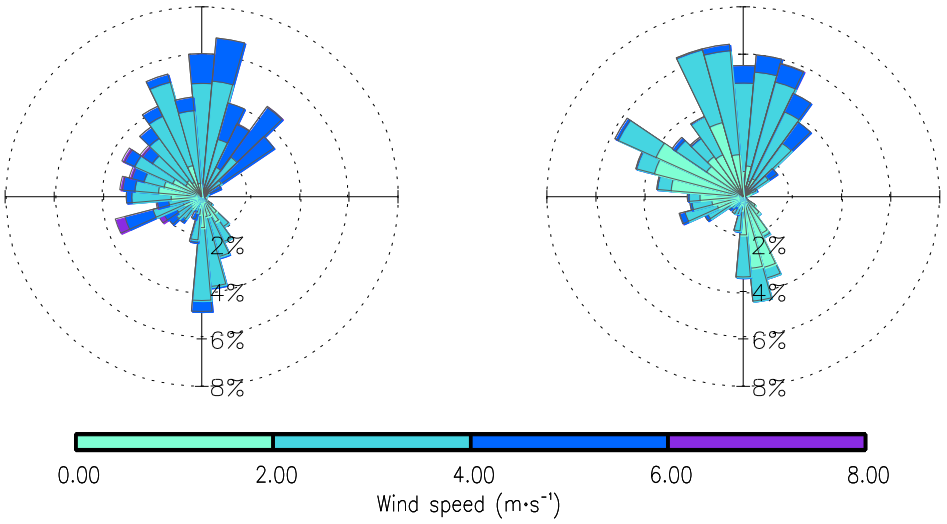

Figure 26 Wind roses for daytime (left, positive net radiation) and nighttime (right, negative net radiation) situation.

2.3.3 Results and discussion

2.3.3.1 Meteorological conditions

The weather in Cairo during the months of the measurement campaign was typical for the hot desert climate (annual mean temperature over 18°C and only little precipitation, which mostly falls in the winter months). The weather was fair most of the time, resulting in a quite regular diurnal course of radiation. The temperature showed a clear diurnal cycle and a decrease from November until around the end of January to rise again in February (monthly means of air temperature: November: 19.3°C, December: 16.2°C, January: 13.0°C, February: 14.1°).

Moreover, wind speed also showed a clear diurnal cycle: the maximum wind speed was observed around at 2 or 3 pm and the minimum at around 7 am. However, no such diurnal course was observed for the wind direction. Two dominant wind directions were observed: a north-eastern and a southern component, while winds from the north-eastern direction were more frequent and normally stronger (Figure 26). A less frequent south-western component agreed well with the observations of Favez *et al*. (2008), who found these winds mainly blowing during winter time. In their study, during summer, the wind came predominantly from the north, while in the winter and spring months the presence of the south-western winds had an important impact. In Cairo, these south-western winds are called 'Khamasin winds' and are often associated with dust storms (Favez *et al*., 2008). During the measurement campaign, especially in January, sand storms occurred, which subsequently impaired the measurements, as the instrument got very dirty. Generally, the air over Cairo was often dusty due to the strong air pollution. For a more detailed description of the meteorological conditions during the measurement campaign see Frey *et al*. (2010).

2.3.3.2 Average CO_2 fluxes and CO_2 concentrations

The CO_2 fluxes showed a diurnal pattern consisting of daily peaks with maximum values up to 40 µmol m^{-2} s^{-1} and minimum values down to -20 µmol m^{-2} s^{-1}. The mean CO_2 flux during the measurement campaign was 6.18 µmol m^{-2} s^{-1} (with 50% of the data in between 1.19 µmol m^{-2} s^{-1} and 9.86 µmol m^{-2} s^{-1}). Thus, on average the fluxes were always directed away from the surface. Concerning the CO_2 concentrations, a diurnal pattern with daily peaks was observed; however, the variations were not as regular as the ones from the fluxes. The mean concentration during the measurement campaign was 403 ppm (with 50% of the data in between 388 ppm and 411 ppm).

On the average diurnal course (Figure 27), the fluxes increased during the morning, to finally peak in a maximum average value of 13.7 µmol m^{-2} s^{-1} at 2.30 pm, and then sank continuously to reach their minimum average value of 1.1 µmol m^{-2} s^{-1} in the morning at 6 am. The single maximum at around 2.30 pm is late compared to the studies of Velasco *et al*. (2005), Vogt *et al*. (2006), Coutts *et al*. (2007) and Moriwaki *et al*. (2006) where the CO_2 fluxes peaked in the morning, and sometimes again in the evening, and were related to rush-hour traffic. A small peak at 8 am may have resulted from rush-hour as traffic starts between 7 and 8 am, but it is not distinct enough to really relate it to a traffic pattern. Thus, distinct rush-hour peaks were not evident in Cairo. Moreover, the CO_2 fluxes started to increase clearly after 6 am while in the above-mentioned studies, the increase occurred earlier than 6 am. The maximum CO_2 fluxes in the afternoon correspond quite well with the maximum in wind speed, though (Figure 27). The absence of rush-hour peaks might also be related to the fact that there is dense traffic in Cairo over the whole day, and no clear difference between rush-hour periods and periods with less traffic. Thus, the rush-hour peaks might not have been as distinct as in other cities, and reflect the

general very intense traffic. Moreover, the distance to the street with high traffic density possibly attenuated potential rush-hour peaks.

The average diurnal course of the CO_2 concentrations was described by Vogt *et al*. (2006) in four stages: (1.) Low concentrations in the afternoon with the minimum concentrations in the early evening. (2.) Rising concentrations during the late evening and through the night. (3.) Maximum values in the early morning around 06:00. (4.) Rapid decrease of the concentrations until noon. This pattern was also found in the other studies and was confirmed by the measurements in Cairo (Figure 27).

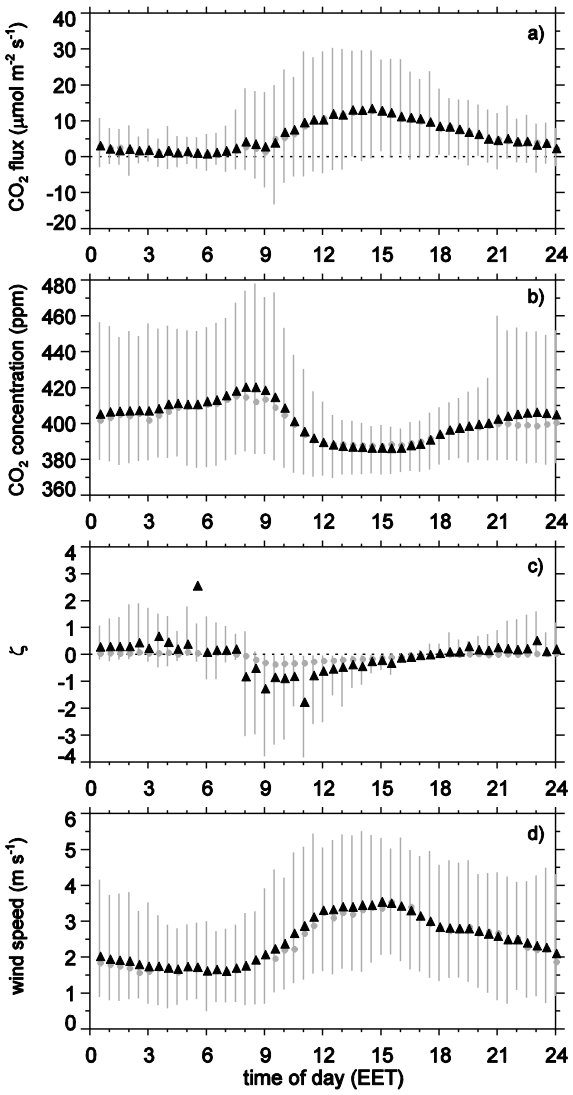

Figure 27 Average diurnal courses of a) CO_2 fluxes, b) CO_2 concentrations, c) stability index and d) wind speed. Triangle: mean, circle: median, grey bars: contain 90% of the data.

The CO_2 concentrations rose during the night, to reach the maximum average value of 421 ppm at 8.30 am. While the concentrations increased steadily to this morning peak, the subsequent decrease occurred relatively suddenly. The minimum average value of 387 ppm was reached in the afternoon at 3.30 pm. The statistical spread was higher for nocturnal values compared to diurnal values. But the morning peak was considerably later (around 8 to 9 am) compared to the measurements of Vogt *et al*. (2006), Grimmond *et al*. (2002) and Velasco *et al*. (2007).

The CO_2 fluxes and concentrations were to a large extent influenced by stability (Figure 27). The delayed morning peak of CO_2 concentrations as well as the late increase of CO_2 fluxes matched the average diurnal course of stability well. On average, the conditions were unstable during the day and stable during the night. The change from stable to unstable conditions occurred at around 8 am, and subsequently the CO_2 concentrations decreased. The CO_2 fluxes started to increase after 6 am indicating the starting breakup of the nocturnal boundary layer and continuously rise with increasing wind speed. The change from unstable to stable conditions at around 6 pm is again consistent with an increase in CO_2 concentrations and a decrease in CO_2 fluxes.

While the influence of stability on the average CO_2 fluxes and concentration was quite obvious, the expected influence of traffic on the average CO_2 fluxes and concentration was, as already mentioned, not that apparent. However, the direct influence of traffic became evident on taking a closer look at the average diurnal courses of CO_2 fluxes per weekday (Figure 28). An obvious difference occurred on Friday compared to other weekdays. The fluxes did not peak in a maximum in the afternoon as they did on all other weekdays, and were clearly lower compared to the other weekdays. At around 9 am on Friday the values were even negative on average. On Saturday, the fluxes were higher again but on average still lower than the fluxes on the following weekdays.

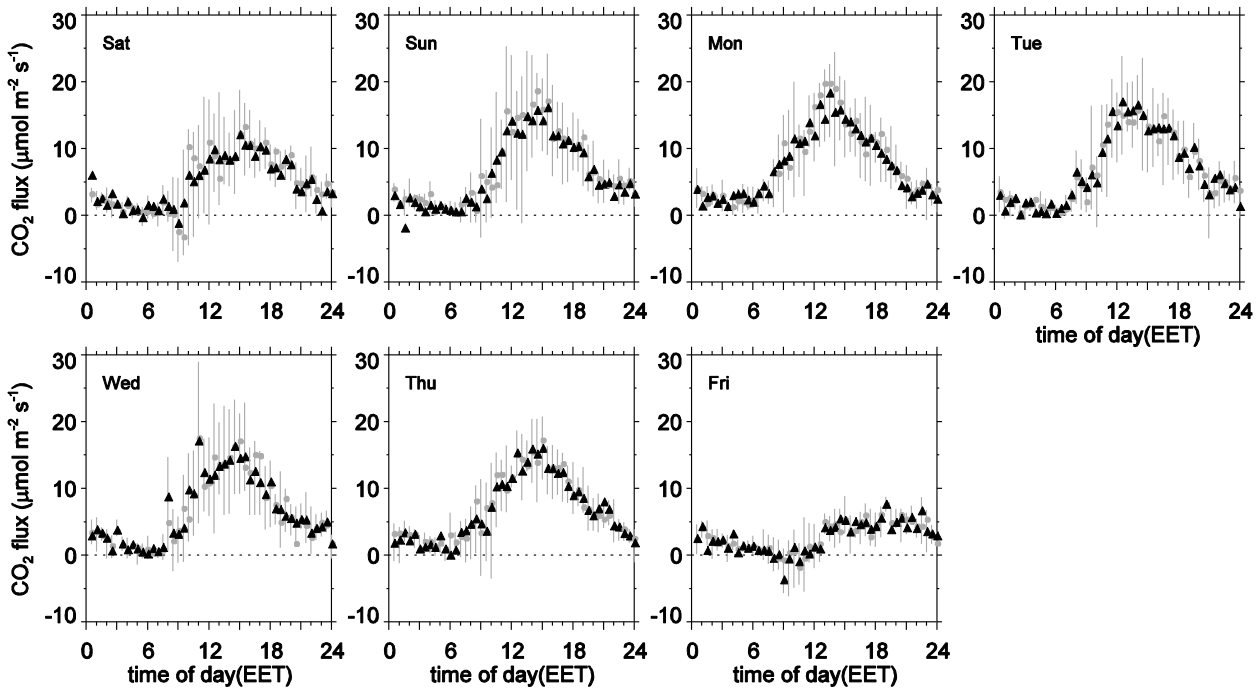

Figure 28 Average diurnal courses of CO_2 fluxes per weekday. Triangle: mean, circle: median, grey bars: contain 50% of the data.

Friday is Sabbath in Cairo, and the traffic density is therefore considerably lower than on the other weekdays. This effect confirmed the influence of traffic on the CO_2 fluxes, although no clear rush-hour peaks were evident. Also on Saturday, the traffic density was still lower compared to the following weekdays, which manifested itself in higher CO_2 fluxes compared to Friday but still lower CO_2 fluxes compared to the other weekdays. Concerning the average diurnal courses of CO_2 concentrations per weekday, no distinct difference between each weekday appeared. The morning peak was at around 9 am on all weekdays.

2.3.3.3 Land use-dependent CO_2 fluxes and concentrations

Both the CO_2 fluxes and the CO_2 concentrations showed a dependency on wind direction (Figure 29). The highest CO_2 fluxes were recorded with winds blowing from the north to the north-east, with some peak values being higher than 40 µmol m^{-2} s^{-1}. With winds from the south to the south-west, the CO_2 fluxes were generally lower with most of the values below 20 µmol m^{-2} s^{-1}. Winds from the east did not occur very frequently, hence, it is difficult to see a certain pattern. Negative CO_2 fluxes were very rare but not restricted to one wind direction although they were more frequent in the south sector compared to the north and the east sector.

The highest CO_2 concentrations occurred with winds from west-northwest with values of up to 500 ppm, and some of them even higher. A second maximum occurred with winds from south-southwest. These two maxima can be very well explained by the windrose for the nighttime situation (Figure 26). Weak winds frequently came from these directions, especially during the night, resulting in the observed accumulation of CO_2.

Concerning the three defined land-use sectors, the CO_2 fluxes of the north sector (predominantly urban, buildings and roads with heavy traffic) were significantly higher than the ones of the south sector (agricultural fields and sports field). Due to low data availability the east sector is

difficult to evaluate. The CO_2 concentrations were highest in the north sector. There, two clusters could be defined: The already mentioned maximum around west-northwest and a second maximum around north-northwest. The latter mainly occurred in the morning hours around 9 am.

The fact that the CO_2 fluxes of the north sector were higher than the ones of the south sector was also confirmed by the average diurnal CO_2 fluxes per land use sector (Figure 30). The CO_2 fluxes of the north sector peaked in a clear maximum in the afternoon. On the other hand, the average CO_2 fluxes of the south sector showed not such a distinct afternoon peak. Around 9 am, they were, on average, even negative in the south sector, while the ones of the north sector were positive. The lower and partly negative fluxes indicate that the vegetation of the south sector could reduce the CO_2 emissions by photosynthesis, as already observed by Vesala *et al*. (2008b). It has to be kept in mind, however, that at the same time the CO_2 emissions were probably lower in the south sector. The values of the east sector lay in between those of the north sector and those of the south sector. There was no clear influence of the zoological garden in the east sector on the CO_2 fluxes as they were not considerably lower compared to the fluxes from the north sector. Regarding the nocturnal fluxes, there was no distinct difference observable between the three sectors.

Estimations by a one-dimensional footprint model (Hsieh *et al*., 2000) showed that the peak location during unstable conditions did not exceed 100 m, while for stable conditions it lay at around 1000 meters. The street with intense traffic in the north was only included in the 50% flux fetch requirement but not in the peak location which only included the campus area. This might be the reason for the lower than expected CO_2 fluxes, and it can be assumed that measurements taken closer to the street may have yielded different results. In the south sector, the 50% flux fetch requirement mainly consisted of vegetated areas. The large vegetated areas of the zoological garden in the east sector were only included in the 90% flux fetch requirement. This confirmed that the influence of the zoological garden on the CO_2 flux was not very large, and that the measurements were mainly influenced by the close-by street.

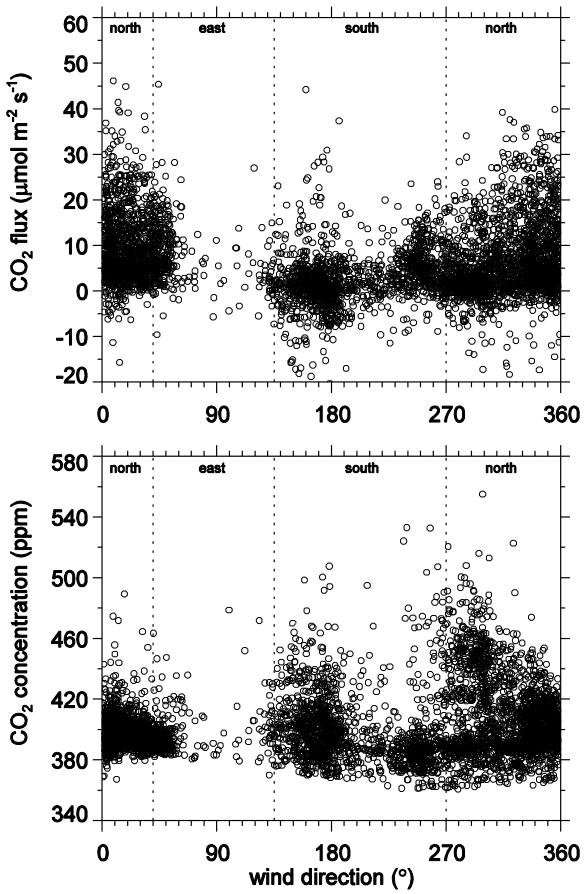

Figure 29 CO_2 fluxes (top) and CO_2 concentrations (bottom) depending on wind direction. Dotted lines mark the division into the three land use sectors: north sector (270-40°, predominantly urban, buildings and roads with heavy traffic), east sector (40-135°, zoological garden), south sector (135-270°, agricultural fields and sports field).

The diurnal CO_2 concentrations of the south sector were lower than the ones of the north sector. This is probably an effect of photosynthesis during the day as well as higher mixing over the vegetated surface as the turbulent heat fluxes were considerably higher

over the south sector compared to the north sector (Frey *et al*., 2010). Concerning both the CO_2 fluxes and concentrations, the overall results highlight that source areas play an important role in the interpretation of the influence of different urban land use on flux measurements. A measurement tower provides a point measurement and its height as well as its exact location influence the results. Measurements taken closer to the street in the north might have revealed different CO_2 fluxes, for example. The influence of vegetation on the CO_2 emissions was quite obvious and underlines the importance of urban vegetation in relation to urban CO_2 emissions.

In terms of the sector-dependent CO_2 concentrations (Figure 30), the nocturnal concentrations of the north sector were higher than the ones of the south sector. They were most probably influenced by additional urban CO_2 sources. Moreover, the lower nocturnal concentrations in the south sector were surprising, since they were expected to be influenced by the nocturnal respiration of the vegetation. This would have resulted in higher nocturnal concentrations over the vegetated surface of the south sector compared to the nocturnal concentrations over the urban surface of the north sector. The estimates of the flux fetch requirements revealed that the source area under stable conditions could outreach the vegetation area. This could be one reason why the nocturnal respiration did not leave a clear signal in the measurements.

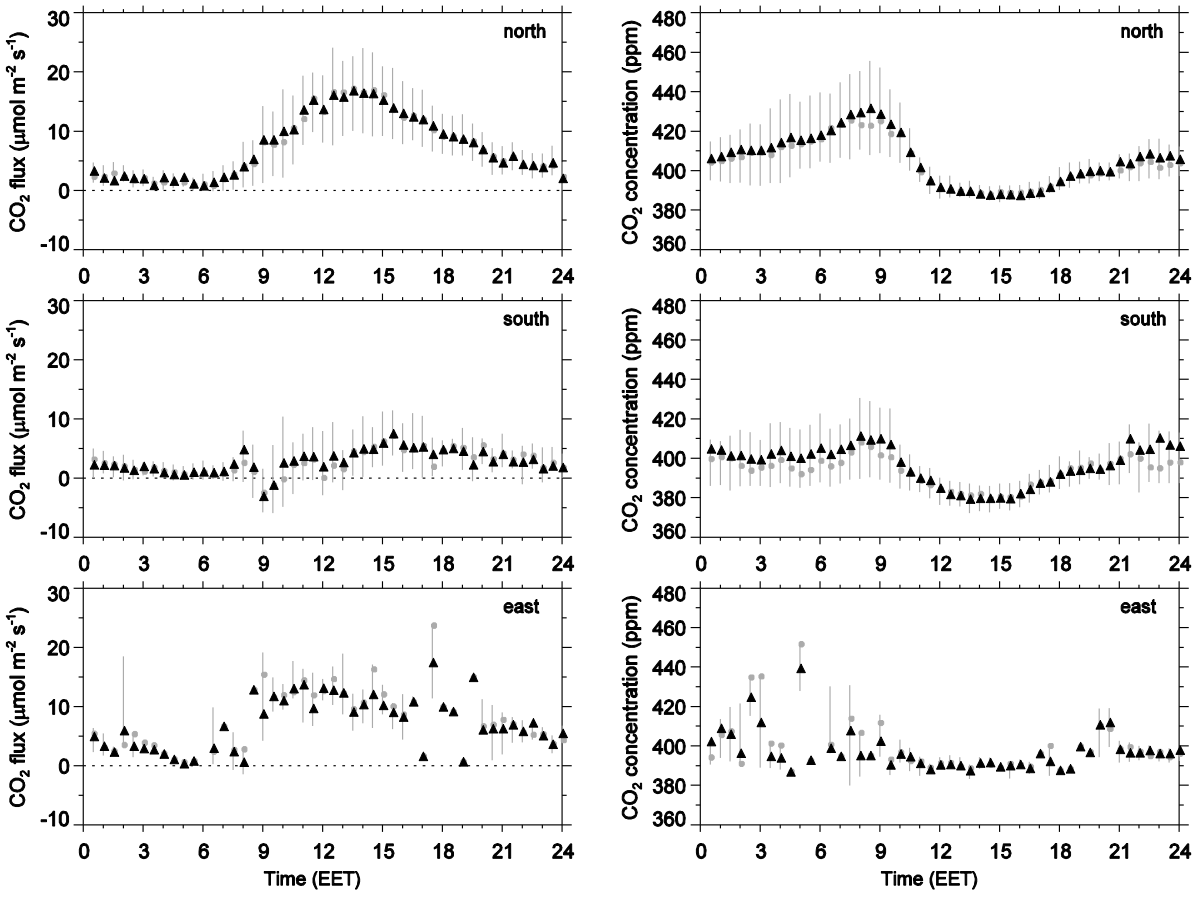

Figure 30 Average diurnal course of CO_2 fluxes (left) and of CO_2 concentrations (right) per land use sector. North sector: 270-40°, predominantly urban, buildings and roads with heavy traffic; east sector: 40-135°, zoological garden; south sector: 135-270°, agricultural fields and sports field. Triangle: mean, circle: median, grey bars: contain 50% of the data.

2.3.4 Conclusion

The aim of the present study was to provide insight into the CO_2 fluxes and concentrations of the city Cairo. Cairo, a city of a non-industrial country, with its location in a hot and dry climate and its enormous air pollution is a unique place to measure urban CO_2 fluxes and concentrations, especially as few studies exist from comparable cities so far. Cities contribute significantly to CO_2 emissions, and are therefore of special interest, especially for analysis or modelling of the carbon cycle on a local to regional scale.

Cairo with its high traffic density and a considerable share of old cars as well as other CO_2 emitters was expected to show higher CO_2 fluxes than cities of more developed countries. However, results showed that the average diurnal course of CO_2 fluxes was not as distinctly coupled to the traffic regime as it was in previous studies of other cities. No distinct rush-hour peaks occurred and the CO_2 fluxes were not considerably higher compared to cities of industrial countries. The fact that the exact diurnal course of traffic was not known, made the interpretation of the data in connection with traffic more complicated. Moreover, the relation of CO_2 fluxes to traffic may also have been blurred by the stability regime and the distance to the direct CO_2 sources. Nevertheless, the influence of traffic became most evident on Fridays (Sabbath in Cairo), when the fluxes were considerably lower compared to the other weekdays.

The CO_2 concentrations showed an average diurnal course with the maximum in the early morning as a result of the nocturnal stable boundary layer. In general, the CO_2 concentrations were governed to a large extent by the stability regime, since the diurnal courses of the CO_2 concentrations and of the stability matched quite well.

From the investigation of the various urban surfaces on the CO_2 fluxes and concentrations, it can be concluded that the vegetated area in Cairo was actually able to reduce the CO_2 fluxes. The negative fluxes induced by photosynthesis, however, were superimposed by the overall CO_2 source of the city, and the CO_2 fluxes resulted therefore positive on average. Regarding the CO_2 concentrations, the morning peak and the daily concentrations were considerably lower over the vegetated area.

In conclusion, it has to be said that it is difficult to draw universally valid conclusions from the present study, because its CO_2 measurements at the city of Cairo represent a relatively short time span only. Moreover, comparisons with traffic counts, which unfortunately were not available, could have revealed a more detailed view on the traffic regime and might have simplified data interpretation in relation to traffic. Nevertheless, a valuable insight into the CO_2 dynamics at the site in Cairo city could be gained. Due to the small number of other eddy covariance measurements of CO_2 fluxes and concentrations from urban areas of non-industrial countries at present, this study represents a special contribution in this respect.

2.3.5 Acknowledgments

Many thanks go to Maha Harhash and Mohammad M. Abdel Wahab of the Astronomy Department at Cairo University for the help and support in Cairo during the measurement campaign. The core project of CAPAC was supported by the Swiss National Science Foundation (grant number 200021-1094).

2.3.6 References

Churkina G. 2008. Modeling the carbon cycle of urban systems. *Ecological Modelling* **216**: 107-113.

Coutts AM, Beringer J, Tapper NJ. 2007. Characteristics influencing the variability of urban CO_2 fluxes in Melbourne, Australia. *Atmospheric Environment* **41**: 51-62.

Denman KL, Brasseur G, Chidthaisong P, Ciais P, Cox PM, Dickinson RE, Hauglustaine C, Heinze C, Holland E, Jacob D, Lohmann U, Ramachandran S, da Silva Dias PL, Wofsy SC, Zhang X. 2007. Couplings Between Changes in the Climate

System and Biogeochemistry. In: *Climate Change 2007: The Physical Science Basis. Contribution of Working Group I to the Fourth Assessment Report of the Intergovernmental Panel on Climate Change* [Solomon S, Qin D, Manning M, Chen Z, Marquis M, Averyt KB, Tignor M, Miller HL (eds.)]. Cambridge University Press, Cambridge, United Kingdom and New York, NY, USA.

Favez O, Cachier H, Sciare J, Alfaro SC, El-Araby TM, Harhash MA, Abdelwahab MM. 2008. Seasonality of major aerosol species and their transformations in Cairo megacity. *Atmospheric Environment* **42 (7)**: 1502-1516.

Frey C, Parlow E, Vogt R, Abdel Wahab M, Harhash M. 2010. Flux measurements in Cairo. Part 1 – In situ measurements. *International Journal of Climatology*.

Grimmond CSB, King TS, Cropley FD, Nowak DJ, Souch C. 2002. Local-scale fluxes of carbon dioxide in urban environments: methodological challenges and results from Chicago. *Environmental Pollution* **116**: 243-254.

Grimmond CSB, Salmond JA, Oke TR, Offerle B, Lemonsu A. 2004. Flux and turbulence measurements at a densely built-up site in Marseille: Heat, mass (water and carbon dioxide), and momentum. *Journal of Geophysical Research* **109**: D24101 1-19.

Hsieh CI, Katul G, Chi T. 2000. An approximate analytical model for footprint estimation of scalar fluxes in thermally stratified atmospheric flows. *Advances in Water Resources* **23**: 765-772.

Ibrahim FN, Ibrahim B. 2006. *Ägypten*. Wissenschaftliche Buchgesellschaft (WBG): Darmstadt.

Moriwaki R, Kanda M. 2004. Seasonal and diurnal fluxes of radiation, heat, water vapor, and carbon dioxide over a suburban area. *Journal of Applied Meteorology* **43**: 1700-1710.

Moriwaki R, Kanda M, Nitta H. 2006. Carbon dioxide build-up within a suburban canopy layer in winter night. *Atmospheric Environment* **40**: 1394-1407.

Nemitz E, Hargreaves KJ, McDonald AG, Dorsey JR, Fowler D. 2002. Micrometeorological measurements of the urban heat budget and CO_2 emissions on a city scale. *Environmental Science and Technology* **36**: 3139-3146.

Schotanus P, Nieuwstadt FTM, De Bruin HAR. 1983. Temperature measurement with a sonic anemometer and its application to heat and moisture fluxes. *Boundary-Layer Meteorology* **26**: 81-94.

Soegaard H, Møller-Jensen L. 2003. Towards a spatial CO_2 budget of a metropolitan region based on textural image classification and flux measurements. *Remote Sensing of Environment* **87**: 283-294.

Velasco E, Pressley S, Allwine E, Westberg H, Lamb B. 2005. Measurements of CO_2 fluxes from the Mexico City urban landscape. *Atmospheric Environment* **39**: 7433-7446.

Vesala T, Kljun N, Rannik Ü, Rinne J, Sogachev A, Markkanen T, Sabelfeld K, Foken T, Leclerc MY. 2008a. Flux and concentration footprint modelling: State of the art. *Environmental Pollution* **152**: 653-666.

Vesala T, Järvi L, Launiainen S, Sogachev A, Rannik Ü, Mammarella I, Siivola E, Keronen P, Rinne J, Riikonen A, Nikinmaa E. 2008b. Surface-atmosphere interactions over complex urban terrain in Helsinki, Finland. *Tellus*, **60B**: 188-199.

Vogt R, Christen A, Rotach MW, Roth M, Satyanarayana ANV. 2006. Temporal dynamics of CO_2 fluxes and profiles over a central European city. *Theoretical and Applied Climatology* **84**: 117-126.

Webb EK, Pearman GI, Leuning R. 1980. Correction of flux measurements for density effects due to heat and water vapour transfer. *Quart. J. R. Met. Soc* **106**: 85-100.

2.4 Determination of the aerodynamic resistance to heat using morphometric methods

Corinne Frey, Eberhard Parlow

Submitted to eProceedings of EARSeL

ABSTRACT *The spatial estimation of the aerodynamic resistance to heat using morphometric methods was evaluated on the example of three different approaches using a digital surface model to calculate the roughness length for momentum and heat. The digital surface model was a result of manual digitizing of a Google Earth image and another model retrieved from two stereoscopic SPOT images. Resulting values for the building area density and frontal area index were slightly lower than comparable values found in the literature, which could be attributed to the building structure. An empirical parameter α, used for the calculation of the roughness length for heat, was fitted to observational data. α was found to be higher than suggested by literature values. The three morphometric methods proved to follow the same principle, spatial analysis however showed that they produced different results in some very dense areas.*

2.4.1 Introduction

The determination of the aerodynamic resistance to transfer of sensible heat r_h, short 'aerodynamic resistance to heat', is necessary in the estimation of heat fluxes using Bulk transfer methods applied with satellite data. In such approaches remotely sensed surface temperatures are combined with an estimation of this parameter r_h, together with the climatological variables air temperature, net radiation, and soil heat flux to derive the final product, the turbulent heat fluxes. r_h thereby is a function of the roughness of the surface, described by the displacement height z_d and the roughness length for momentum z_{0m} and heat z_{0h} (Verma, 1989). The roughness of the surface is very distinct in urban areas; therefore a sound determination of these parameters is essential for successful flux modelling. Grimmond & Oke (1999) have summarized several morphometric methods to determine z_d and z_{0m} from a digital surface model, finding a distinct variability in the output of the tested approaches. They ranked the approaches by comparing their output to measurement values. They found the methods of Bottema (1997), Raupach (1994, 1995) and Macdonald et al. (1998) to score highest. Liu et al. (2008) also verified these three methods with observational data. Their results suggest that the three methods are not very different from each other.

In the above mentioned three morphometric methods, the average roof height, the building area density, and the frontal area index are used. These indices can be calculated from a digital surface model using trigonometry. Burian et al. (2002) has described the calculation of these parameters in a GIS (Geographic Information System) and their subsequent use for the estimation of the roughness parameters. Also some other studies have reported on roughness parameters in urban areas. Gál & Sümeghy (2007) for example presented an urban roughness mapping method with the approach from Bottema (1997) to localize ventilation paths in the city. Ratti et al. (2002) used the approach from Macdonald et al. (1998) to extract several flow and dispersion parameters from an urban database. The parameters are the plan and frontal area densities, their function and distribution with height, their standard deviation, the aerodynamic roughness length and the sky view factor. Ioannilli & Rocchi (2008) finally compared the methods of Bottema (1997) and

Raupach (1994, 1995) for a portion of Rome, using cadastral databases. In many developed countries, digital surface models have been made available for cities by the respective authorities. In developing countries however, this data is mostly not existing at all or not available for external researchers. Also for our study area no such model was available; therefore it had to be generated manually. The resulting digital surface model does not offer the same accuracy of up-to-date models generated from cadastral maps and provided by authorities. However, it is a good alternative and is sufficient for the needs of this study.

In this research, the three above mentioned best-fitting morphometric methods for the estimation of z_d and z_{0m} are used to deduct the aerodynamic resistance to heat r_h for a comparison with estimations of r_h from in situ measurements in an urban area. The methods used were proposed by Raupach (1994, 1995), by Macdonald et al. (1998) and by Bottema (1997) and are further referred as RA, MA and BO. Additionally, an empiric relation connecting the roughness length heat z0h with Re^* (Brutsaert 1982, Kanda et al. 2007) was fitted to the data set with in situ measurements of r_h. A new value of an empirical parameter used in this relation is subsequently proposed.

The results of this study can be used by researchers using very high resolution remote sensing approaches or urban climate models, by seeing the effect of these three different approaches and by proposing a new empiric value for the estimation of the roughness length for heat in urban areas. Especially the definition of new values for this relation has been the topic of a couple of recent publications (Kanda et al., 2007; Kawai et al., 2009; Loridan et al., 2010) that focus on urban environments. This research is farther input in this discussion. Besides this, the study shortly discusses the optimal resolution for the calculation of the input parameter from the digital surface model for this study area.

2.4.2 Study area

The study area is a small part of the Gizah district in the megacity Cairo in Egypt. Central to the area is the campus of the Cairo University. The campus consists of broad blocks and spacious squares and alleys. Some trees and bushes are planted along the alleys. Botanical test fields are to the south of the campus. The fields of this area are sometimes surrounded by trees. A park and a zoological garden both with dense tree cover are found in the East of the campus and very dense housing blocks emerge from the west and to the north of the campus. These blocks belong to lower income social classes. The cross-streets between the single houses of these blocks are extremely narrow and are often not clearly detectable on satellite images. The whole area is 3.205 x 2.45 km.

2.4.3 Methods

2.4.3.1 Calculation of the aerodynamic resistance to heat

From November 2007 to February 2008 a micrometeorological field campaign was conducted in Cairo, Egypt (Frey et al. 2010). Micrometeorological parameters were continuously measured at three stations. One of these stations was located at the campus of Cairo University, on a building in the south of the campus (‘Laser’-Building at 30°01’33.39’’N, 31°12’27.81’’E, see figure 1). r_h [sm^{-1}] was computed from measurements of radiative surface temperature T_s [K], air temperature T_a [K] and sensible heat flux Q_H [Wm^{-2}] in half hourly intervals, following Verma (1989)

$$\mathrm{Q_H} = \rho_{air} \cdot c_p \cdot \frac{T_s - T_a}{r_h} \qquad (42)$$

where ρ_{air} is the density of air [kg m^{-3}] and C_p the specific heat of air at constant pressure [J kg^{-1} K^{-1}].

Also following Verma (1989), r_{ah} can be expressed by

$$r_{ah} = \frac{1}{ku^*}\left(ln\left(\frac{z-z_d}{z_{0m}}\right) - \psi_h\right) + \frac{1}{ku^*}\left(ln\left(\frac{z_{0m}}{z_{0h}}\right)\right) \quad (43)$$

as was done previously by Xu et al. (2008). u^* is the friction velocity [ms^{-1}], k is the Karman's constant (=0.4) and ψ_h is a stability correction function for heat, depending on the Monin Obukhov length (Foken 2003). The first term in equation (43) thereby corresponds to the aerodynamic resistance for momentum, the latter term to a bulk aerodynamic excess resistance. Please refer to Liu et al. (2007) for other parameterizations of r_{ah}. As equation (43) does not allow an input of zero for z_{0m} and z_{0h}, these terms were set to 1e-4, and 1e-5 in respective cases.

The aerodynamic surface temperature T_0 which is originally used in the bulk transfer equation (equation (42)) is the temperature extrapolated to a surface that is at the height $z_d + z_{0h}$ (the zero-plane displacement length plus roughness length for heat [m]). However, the introduction of a corrective term, the radiometric excess resistance, allows substituting T_0 with the radiometric surface temperature T_s as was done in equation (42) (Chehbouni et al 2001). The radiometric excess resistance is

$$r_r = \frac{kB^{-1}}{u^* \cdot k} \quad \text{, with} \quad (44)$$

$$kB^{-1} = ln\left(\frac{z_{0m}}{z_{0h}}\right). \quad (45)$$

r_h in equation (42) is the sum of r_{ah} and r_r.

$$r_h = r_{ah} + r_r \quad (46)$$

Please refer to Voogt and Grimmond (2000) for a more detailed discussion of the assumptions made above.

The roughness length z_{0m} used in equation (43) was estimated with the three methods RA, MA and BO. All these methods need the input parameter λ_f which is the frontal area index. This index uses the length of any obstacle, the mean height of the obstacle, as well as the angle of attack of the prevailing wind to the obstacle in a given window. To extract this information for the given area, a digital surface model must be available. As no such model was available for the study area, it was generated manually as described in the next section.

2.4.3.2 Generation of a digital surface model

For the calculation of the roughness lengths, first a simple digital surface model of the closer surrounding of Cairo University was built. The buildings were digitized manually from a Google Earth cut-out in 1.5 km view in the ENVI programme from ITT Visual Information Solutions. Many of the cross-streets in some low income areas were not detectable from the Google Earth image. Therefore the houses along a bigger street were digitized as one block. These cross-streets are extremely narrow and the wall surfaces of the canyons are not exposed to the dominant wind system of the broader area. Therefore it is considered to be legitimate to omit these streets and treat the building series of a whole street-side as one block. Afterwards, mean heights were allocated to the buildings using a coarser digital surface model of the area that was extracted from two stereoscopic SPOT images (Goossens 2008). As the SPOT surface model did not assign a correct height to the 'Laser'-Building, a corrective factor was introduced all over the area to match the height of the 'Laser'-Building to the actual height of the building.

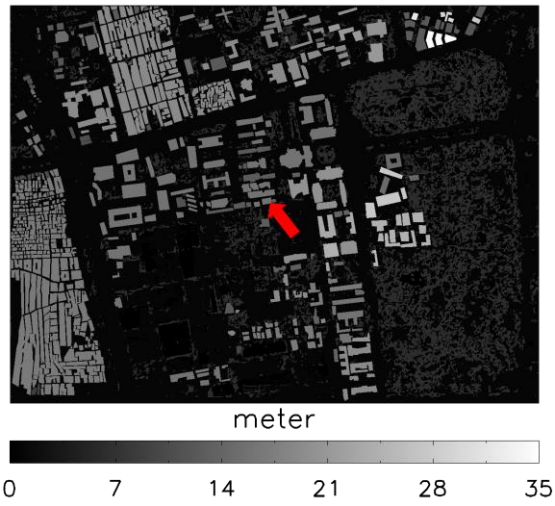

Figure 31 The surface model including vegetation. Grey values correspond to height. The model is oriented to North.

Some extended vegetated areas exist in the area as described above. To analyse the influence of this vegetation on the estimated roughness parameters, a second model was built. Trees and fields were extracted using the RGB values of the Google Earth image. Thereby thresholds for the slope between the blue and the green and between the green and the red channel were used to find the vegetated areas. Trees and fields were then separated using the dissimilarity filter implemented in the ENVI programme. The vegetative covers of the fields were assigned a height of 0.2 m; trees got an average height of 8 m. By merging the two height models – buildings and vegetation - a second model was built. Figure 1 shows this model in 2D. Both models were saved with a spatial resolution of 2.5 m.

2.4.3.3 Estimation of the frontal area index λ_f

There is no common way of calculating the frontal area index so far, thus the used routine shall be explained below. In a first step, the length of any obstacle in a moving window was calculated. The window width was 3 pixels (= 7.5 m). Thereby it was assumed, that only one obstacle can be located in the set window at any time (see Figure 32).

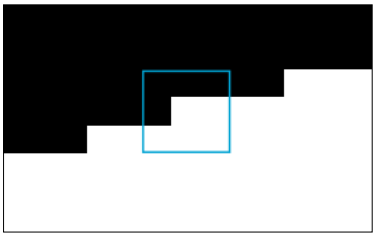

Figure 32 Example of a south-south-east oriented wall with a moving window size of 3 pixels (blue square). Inside the moving window are 4 black pixels representing an obstacle and 5 white pixels representing open space.

In each window, the pixels were divided into obstacle and open space. If one of the four direct neighbouring pixels of a pixel was open space, then this pixel was classified as wall (belonging to an obstacle). The boundary of this obstacle (building or a group of trees) could have only one direction (azimuth angle, east of north). Edges of obstacles were not detected separately. So, if an edge occurred in the window, it was treated as a wall, having the directional properties of the mean of the two adjacent walls of the edge. The mean azimuth angle of all wall pixels was determined using trigonometry. The mean height is just the average height of all obstacles in a window.

This approach was originally developed for buildings only. The vegetation in the second model is handled in the same way as buildings. This simplification introduces some uncertainty, as vegetation is semi-permeable for air masses and does not cause the same roughness as massive walls. The inclusion of vegetation might therefore overestimate the roughness and results should be treated with care.

The calculation of the frontal area index λ_f and the density of the obstacles λ_p was done in a second step with a moving window of 125 m (50 pixel). λ_f was calculated using

$$\lambda_f = \overline{L_y}\overline{z_h}/A_T \qquad (47)$$

where $\overline{L_y}$ is the mean breadth of roughness elements perpendicular to the wind direction. The mean breadth of the roughness elements was weighted with a cosine function according to the relation of the azimuth angle and the angle of attack of the wind. $\overline{z_h}$ is the mean height of the lot area and A_T is the total lot area. The density of the obstacles λ_p, used for example in equation (48), was estimated using the ratio of the number of pixels with obstacles and the window size.

Burian et al. (2002) have pointed out, that the window size for the calculation of λ_f should be chosen such that the characteristics of interest in the urban area are discernible. In this research, the window size for the calculation of the frontal area index was first varied from 25 m to 150 m to assess the sensitivity of r_h to the window size. It was found, that window sizes greater than 75 m produced r_h values that did not change anymore significantly. Lower window sizes however increased r_h substantially. For example: r_h calculated with a 25 m window size was 20 to 40 sm^{-1} lower than calculated with a 150 m window size (MA method with α ranging from -0.1 to -1, see equations (50), (51) and (55), including all occurring wind speeds). Lower α values decrease the difference. Further analyses are made on 125 m basis, which is thought to be a good window size to represent a single unit in this study area, coupled with acceptable computing times. Smaller sizes down to 75 m would also be acceptable. Bigger window sizes (in this study done up to 150 m) are just increasing the computing time.

2.4.3.4 Calculation of roughness lengths

The roughness lengths were then estimated following the three approaches addressed in the introduction. BO relates z_d/z_h to an exponential curve of the density of the obstacles λ_p, while z_{0m}/z_h is given by a natural logarithm. For simplicity, the in-plane sheltering displacement height of BO is set equal to z_d.

$$\frac{z_d}{z_h} = {\lambda_p}^{0.6} \quad (48)$$

$$\frac{z_{0m}}{z_h} = \frac{z_h - z_d}{z_h} \exp\left(-\frac{\mathrm{k}}{(0.5\mathrm{C_{Dh}}\lambda_\mathrm{f})^{0.5}}\right) \quad (49)$$

C_{Dh} is the isolated obstacle drag coefficient (=0.8). According to MA, the zero-plane displacement height z_d is given by

$$\frac{z_d}{z_h} = 1 + {\alpha_m}^{-\lambda_p}(\lambda_p - 1) \quad . \quad (50)$$

The roughness length for momentum z_{0m} is found by

$$\frac{z_{0m}}{z_h} = \left(1 - \frac{z_d}{z_h}\right) \exp\left\{-\left[0.5\beta_m \frac{C_D}{k^2}\left(1 - zdzh\lambda f - 0.5\right)\right.\right. \quad , \quad (51)$$

where α_m and β_m are empirical constants. The latter constant is a net correction factor for the drag coefficient. Recommended values are α_m=4.43 and β_m=1.0. C_D is a drag coefficient (=1.2).

RA gives the zero-plane displacement height z_d as

$$\frac{z_d}{z_h} = 1 - \frac{1 - exp\left[-\left(2c_{d1}\lambda_f\right)^{0.5}\right]}{\left(2c_{d1}\lambda_f\right)^{0.5}} \quad (52)$$

And the roughness length for momentum z_{0m} is found by

$$\frac{z_{0\mathrm{m}}}{z_h} = \left(1 - \frac{z_d}{z_h}\right) \exp\left\{-k\frac{U}{u_*} + \psi_h\right\} \text{ , where} \quad (53)$$

$$\frac{u_*}{U} = min\left[\left(c_s + c_r\lambda_f\right)^{0.5}, \left(\frac{u_*}{U}\right)_{max}\right] \quad (54)$$

Ψ_h is the roughness sublayer influence function, U is the large-scale wind speed, u^* is the friction velocity, c_s and c_r are drag coefficients for the substrate surface at height z_h in the absence of roughness elements, and of an isolated roughness element mounted on the surface. c_{d1} is an empirical constant. According to RA c_S = 0.003, c_R = 0.3, $(u^*/U)_{max}$ = 0.3, Ψ_h = 0.193, and c_{d1} = 7.5 was used. Note that the notation of equation (52) is different from the respective given in Grimmond & Oke (1999).

The roughness length for heat z_{0h} was found for all 3 approaches using

$$z_{0h} = z_{0m} \cdot \beta \cdot exp\left(\alpha \cdot Re^{*^{0.25}}\right) \quad , \qquad (55)$$

with Re^* being the Roughness Reynolds number. α and β are empirical constants for bluff-rough situations given by Brutsaert (1982). Xu et al. (2008) and Loridan et al. (2010) used -1.29 for α, which they took from the work of Kanda et al. (2007) for urban areas. Kanda et al. (2007) regressed data from an outdoor experiment with the Comprehensive Outdoor Scale Model (COSMO) to find the relationship between kB^{-1} and Re^*, a different form of equation (55). They found that the regressed function agreed with data from three other urban sites better than using the Brutsaert (1982) value, even though the surface geometry of the urban sites differed. This α parameter is subject to further research in this paper and alternative values are investigated. β is kept constant at 7.4 (Voogt & Grimmond 2000).

To give an overview of the whole methodology, in Figure 33 a diagram is given with an overview of the different processing steps in this study.

2.4.3.5 Footprint modelling

To compare the results with the measurements, the footprint model of Kormann & Meixner (2000) was used. The model output was thereby adjusted to the pixel resolution of the citymodel and laid over the image to fit the measurement station.

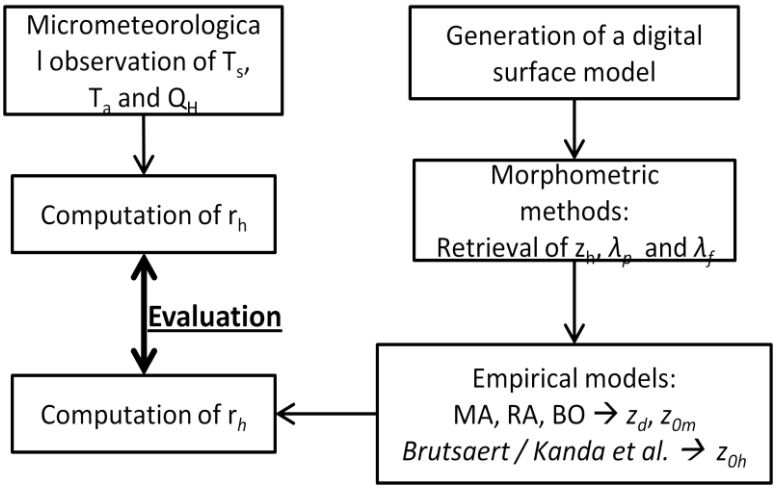

Figure 33 Overview of the different processing steps of the study

2.4.4 Results

2.4.4.1 Mean density and frontal area index

The mean density λ_p and the mean frontal area index λ_f were calculated twofold: a) for the whole area and b) for only the built up area, excluding the botanical test fields in the south of the campus and the parks in the East. This was done for both surface models, excluding and including vegetation. Resulting values are given in Table XIII. λ_p ranges from 0.170 to 0.413, λ_f from 0.079 to 0.138. This corresponds to the lower range of the values of λ_p and λ_f given in Grimmond & Oke (1999). There, λ_p ranges from 0.33 to 0.58 and λ_f from 0.13 to 0.33. Reasons for our low values are firstly found in the very high density areas, where the buildings are put together in the model to form one big block and secondly in the spacious architecture of the campus.

Table XIII Mean density λ_p and mean frontal area index λ_f as calculated from the 150 m resolution windows

	z_h	λ_p	λ_f
First model (including only buildings)			
Whole area	9.21	0.170	0.079
Built up area only	12.72	0.256	0.117
Model (including also vegetation)			
Whole area	8.09	0.413	0.104
Built up area only	10.38	0.346	0.138

2.4.4.2 Comparison of morphometric methods

In a first step, z_d/z_h, z_{0m}/z_h and z_{0h}/z_h of the three different models (MA, BO and RA) were compared by plotting them against λ_p or λ_f (Figure 34). The relation between z_d/z_h and λ_p is comparable in all three approaches (a), d) and g)). Especially the curves of MA and of BO are very similar. z_d/z_h increases when the building density is higher. Note, that the RA approach relates z_d/z_h to λ_f (black curve). The grey values in Figure 34 however give the relation to λ_p.

Increasing the housing density continuously, one will reach a point, where the roughness peaks at a maximum value. More dense housing will decrease the roughness again, as the narrow canyons lose their influence on the air flow. This fact is depicted in the figures b), e) and h) of Figure 34. All three approaches let increase z_{0m}/z_h with increasing λ_f up to a maximum value, to decrease again. The curve of RA for z_{0m}/z_h is a single curve, as it is only dependent of λ_f, while the curves of MA and BO are dependent on λ_f and λ_p. The grey values in b) and c) in Figure 34 depict these dependencies and relative λ_p values are given in the scale bar.

The relation between z_{0h}/z_h and the frontal area index λ_f is less clear and subject to strong scattering. Both the approaches from MA and BO have very low values, with a high scattering up to single values around 200'000. The data using the RA approach is following an increasing trend with increasing λ_f.

2.4.4.3 Alpha parameter

Equation (55) calculates z_{0h} from z_{0m} and the Reynolds number Re^* using the empirical parameters α and β. Brutsaert (1982) sets α to -2.46 for bluff-rough surfaces. However, it seems that this parameter is not suitable for urban areas. While retaining the β parameter of Brutsaert (1982), several options for α were investigated. Thereby r_h was calculated iteratively using equation (43) with an increasing α. The resulting r_h values, calculated for 4 wind directions and 3 wind speed classes, were compared to the r_h values retrieved from the in situ measurements using equation (42). It was shown, that the wind speed did not influence significantly the retrieved best fitting value.

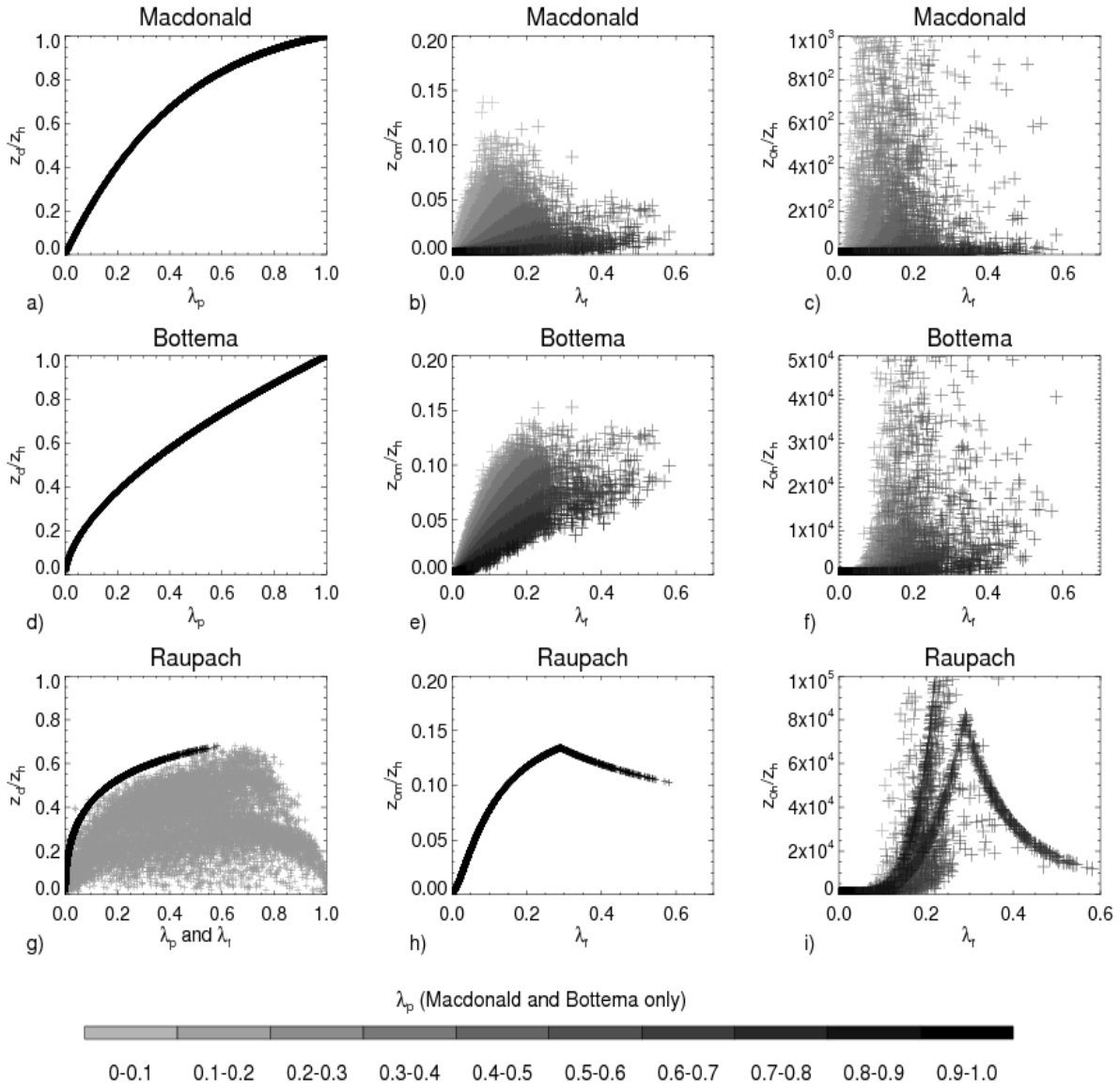

Figure 34 Relation between z_d/z_h and the housing density λ_p and z_{0m}/z_h and z_{0h}/z_h and the frontal area index λ_f for α=0.8 given for the model including vegetation and a window size of 150 m. b), c) e) and f) show additionally the dependence on λ_p (grey values). Note that h) and i) only show relations to λ_f.

Table XIV Differences of r_h [sm^{-1}] in a moving window of 125 m. The footprint model of Kormann & Meixner (2000) was used for the comparison.

α	BO		MA		RA	
	Buildings	Buildings + vegetation	Buildings	Buildings + vegetation	Buildings	Buildings + vegetation
-0.4	23.39	37.63	14.37	26.99	30.04	44.20
-0.5	9.45	22.54	-1.03	14.68	17.39	30.30
-0.6	-4.44	7.47	-16.36	2.39	4.83	16.48
-0.7	-17.80	-7.56	-30.89	-9.77	-6.86	3.10
-0.8	-29.31	-22.32	-42.85	-21.51	-17.18	-9.65

Table XIV gives the differences of the two r_h values respective to α as weighted means from all wind speed classes. It shows, that the best fitting α values range from -0.5 to -0.7 for both surface models. These values are higher than the value proposed by Kanda et al. (2007), but fit much better to the field data he showed in figure 6. Their proposed curve lies mostly over the in situ test data of the business district, Tokyo and the dense residential area, Tokyo, while the curve with the new α values would go right through the measurement data.

In the following several influences in the retrieval of r_h will be investigated. One source of error in the estimation of r_h is the correction of the surface temperatures from the emissivity effect. Emissivity was set to 0.96, according to a analysis of ASTER data of the area (Frey et al. subm.). Comparison calculations showed that lowering the emissivity about 0.02 from 0.96 to 0.94 would decrease the best fitting α values only about 0.1. This quite low difference shows that the emissivity effect alone cannot explain the differences of α to the value of Kanda et al. (2007) or Brutsaert (1982). Another uncertainty is resulting from the fact that instead of the aerodynamic surface temperature T_0 the radiative surface temperature T_s is used in equation (42). Despite the use of a corrective term r_r some uncertainty remains, as the departure of the aerodynamic temperature from the radiative temperature is controlled by several factors that cannot be simply put into one corrective term (Chehbouni et al. 2001). Further, the in situ sensor does not sense the complete surface, but only the surfaces in the field of view (Voogt & Grimmond 2000). Vertical walls not seen by the sensor do contribute to the sensible heat flux, but are not included in the measurement. However, assuming that those vertical walls are at least partly shaded and exhibit lower surface temperatures than the roof areas, resulting r_h values would be lower. Such lower r_h would need higher α values to fit the observational data. So, thermal anisotropy is also not able to explain the high α values compared to Brutsaert (1982). The fact finally, that the λ_p and λ_f values are lower than literature values also does not explain this difference, as higher λ_p and λ_f values would result in a higher aerodynamic resistance to heat, which would also ask for a increase in α to optimally fit the modelled data and the values retrieved from the in situ measurements. As a conclusion new α values of -0.5 to -0.7 are proposed for the application in urban areas similar to our Cairo test case.

Figure 35 shows a comparison of the in situ measured and modelled r_h values according to the wind direction. Only situations with wind speed greater than 1 ms^{-1} and lower than 7 ms^{-1} are considered. Mean in situ values are plotted as bold crosses. They show a distinct directionality which corresponds to the building density in the surrounding of the measurement mast. The modelled values generally follow this pattern well. They were calculated with mean input variables associated with the considered wind speed range. In eastern wind situations the agreement seems to be relatively good, however, not much reference data is available in this sector (Frey et al. 2010). In western wind situations, r_h is underestimated by all models. Such discrepancies can be attributed to the limited accuracy of the digital surface model and the crude assumptions about vegetation. Note, that the in situ measured values have a quite high statistical spread.

2.4.4.4 Spatial distribution

Extended areas with no significant roughness elements came out with a value of zero for z_{0m} and z_{0h}. These areas were set to 1e-4, and 1e-5 m, respectively. Due to this assumption large areas of the first model with parks and fields (in the East of the image), had a constant r_h value (44 sm^{-1} in Figure 36).

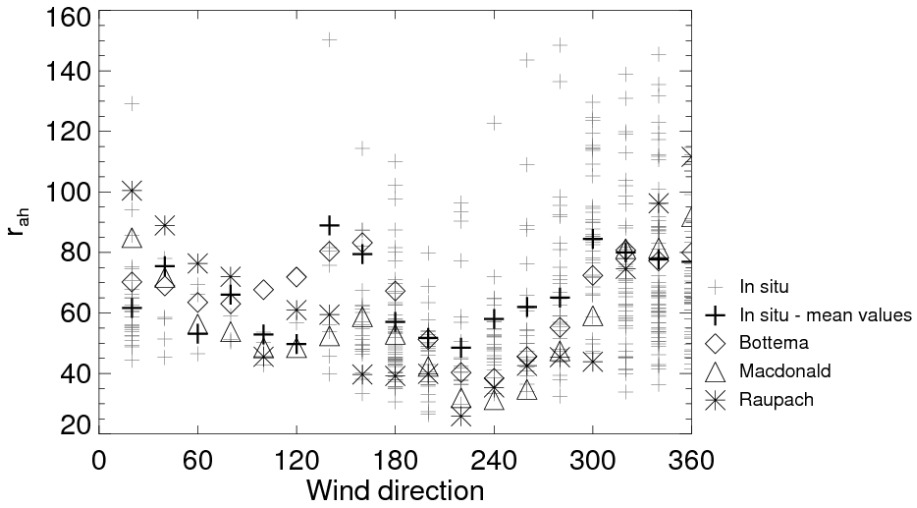

Figure 35 Aerodynamic resistance to heat, calculated with 125 m windows for all wind directions, for the MA, the BO and the RA approach and corresponding in situ values.

The same areas produced values in a similar range in the second model (including vegetation), which is in accordance to measurements done by Liu et al (2007). The r_h values of the open areas did not influence the estimation of the best-fitting α value, as the footprint rarely extended to the East.

The BO and the RA approaches produced very similar spatial pattern, while the MA approach sometimes behaved inverse to the other two: in the very dense housing areas the MA approach showed lower values than BO and RA (see Figure 36). This difference is due to very low z_{0m} values estimated by the MA approach. The relation of z_{0m} and λ_f can be seen in Figure 34. Also there, the MA approach can be distinguished by the production of low z_{0m} values. The MA approach is using two empirical constants α_m and β_m. A further investigation of the influence of these constants on r_h is recommended for future research in the comparison of MA, BO and RA methods.

Highest r_h values are found in all three approaches in a lot with high rise buildings left to the extended park area and in some parts of the very dense housing areas.

2.4.5 Conclusions

The use of morphometric methods for the estimation of the aerodynamic resistance to heat r_h is a promising approach when spatial data are needed. The precondition of a high resolution citymodel however, restricts this method to areas where such models are available. With the launch of TerraSAR-X and its twin TanDEM-X of the German Aerospace Center more and more high resolution DEMs will be available worldwide from about 2014 (www.dlr.de). In this study a new city model was built from Spot and Google Earth images for the extent of the test area.

The mean density λ_p and the mean frontal area index λ_f were lower than literature values because of specific characteristics of the area and the surface model. Higher λ_p and λ_f values would result in a higher aerodynamic resistance.

Due to the semi-empiric nature of the estimation of the roughness lengths, it is necessary, to define optimal parameters for urban surfaces. This study is an approach to find an optimal configuration of the morphometric methods to fit values deducted from in situ measurements. The best fitting α value was similar for the three different methods and the two surface models. Best fitting α values range from -0.5 to -0.7, independent of the wind speed. A value of -0.6 is recommended for further studies in this area.

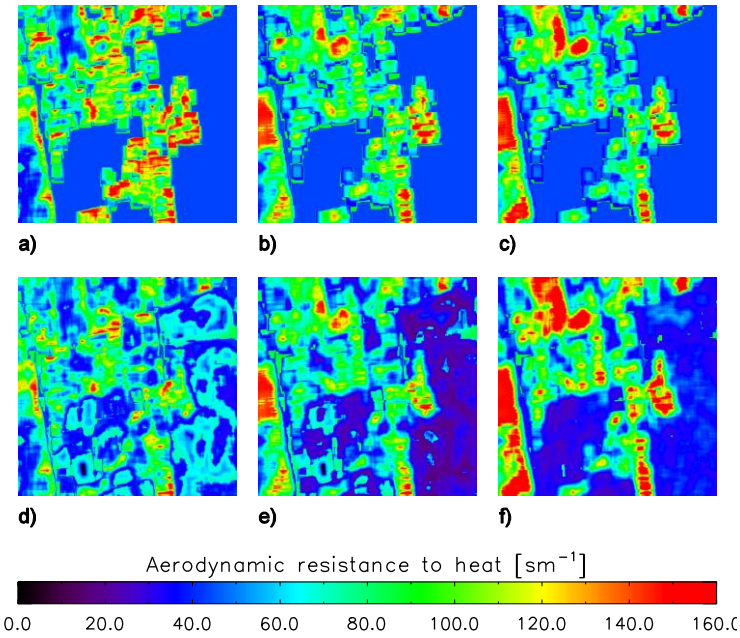

Figure 36 Aerodynamic resistance to heat, calculated with 125 m windows for a wind direction of 0°, for the MA (a + d), the BO (b + e) and the RA (c + f) approach. The upper line shows the first model, the lower line the second model, including assumptions about vegetation.

A wind direction dependent comparison of in situ and modelled r_h values revealed, that all three methods could reproduce the general directional pattern measured by in situ instrumentation induced by different surface roughness.

The spatial analysis finally showed that extended areas with no surface elements produce probably unrealistically values. It is therefore recommended to insert a minimum roughness in extended open areas. The inclusion of vegetation in the model also solved this problem. Generally high r_h values are found in areas with a high roughness, which could be induced by high buildings or a higher building density. Only in some of the very high density areas the three methods didn't agree in their results.

2.4.6 Acknowledgements

This work was supported by the Swiss National Science Foundation (grant number 200020–120080/1).

2.4.7 Literature

Bottema M. 1997. Urban roughness modelling in relation to pollutant dispersion. *Atmospheric Environment* **31**: 3059-3075.

Brutsaert W. 1982. Evaporation into the Atmosphere. Theory, History and Applications. Kluwer Academic Publishers, Dordrecht: 264.

Burian SJ, Michael JB, Linger SP. 2002. Morphological analyses using 3D building databases: Los Angeles, California. *Los Alamos National Laboratory*: 74.

Chehbouni G, Nouvellon Y, Lhomme JP, Watts C, Boulet G, Kerr YH, Moran MS, Goodrich DC. 2001. Estimation of surface sensible heat flux using dual angle observations of radiative surface temperature. *Agriculture and Forest Meteorology* **108**: 55–65.

Frey CM, Parlow E. Flux measurements in Cairo. Part 2: On the determination of the spatial radiation and energy balance using ASTER satellite data. *International Journal of Climatology*. Submitted.

Frey CM, Parlow E, Vogt R, Abdel Wahab M, Harhash M. 2010. Flux measurements in Cairo. Part 1: In situ measurements and their applicability for comparison with satellite data. *International Journal of Climatology*. Accepted.

Gál T, Sümeghy Z. 2007. Mapping the roughness parameters in a large urban area for urban climate applications. *Acta*

Climatologica et Chorologica. Universitatis Szegediensis, Tomus **40-41**: 27-36.

Grimmond CSB, Oke TR. 1999. Aerodynamic properties of urban areas derived from analysis of surface form. *Journal of Applied Meteorology* **38:** 1262-1292.

Goossens R, Tack FMR, Devriendt D, Ateya O, Parlow E. DEM-generation from SPOT 5 across-track imagery. A case study over CAIRO and surroundings. 28th EARSeL Symposium: Remote Sensing for a Changing Europe. Istanbul, Turkey, 2. June - 5. Juni 2008

Ioannilli M, Rocchi E. 2008. Urban Roughness Parameters Calculation in the City of Rome by Applying Analytical and Simplified Formulations: Comparison of Results. *Lecture Notes in Computer Science* **5072**: 284-299.

Kanda M, Kanega M, Kawai T, Moriwaki R, Sugawara H. 2007. Roughness lengths for momentum and heat derived from outdoor urban scale models. *Journal of Applied Meteorology and Climatology* **46**: 1067−1079.

Kawai T, Ridwan MK and Kanda M, 2009: Evaluation of the simple urban energy balance model using selected data from a 1-yr flux observation at two cities. Journal of Applied Meteorology and Climatology 48: 693-715

Kormann R, Meixner FX. 2001. An analytic footprint model for neutral stratification. *Boundary-Layer Meteorology* **99**: 207–224.

Liu G, Sun, J, Jiang W. 2008. Observational verification of urban surface roughness parameters derived from morphological models. *Meteorological Applications* **16**: 205–213.

Liu S, Lu L, Mao D, Jia L, 2007. Evaluating parameterizations of aerodynamic resistance to heat transfer using field measurements. *Hydrology and Earth System Science* **11**: 769-783.

Loridan, T, Grimmond CSB, Grossman-Clarke S, Chen F, Tewari M, Manning K, Martilli A, Kusaka H, and Best M, 2010: Trade-offs and responsiveness of the single-layer urban canopy parameterization in WRF: an offline evaluation using the MOSCEM optimization algorithm and field observations. Quarterly Journal of the Royal Meteorological Society 136: 997–1019

Macdonald RW, Griffiths RF, Hall DJ. 1998. An improved method for the estimation of surface roughness of obstacle arrays, *Atmospheric Environment* **32(11)**: 1857–1864.

Ratti C, Di Sabatino S, Britter R, Brown M, Caton F, Burian S. 2002. Analysis of 3-D Urban Databases with Respect to Pollution Dispersion for a Number of European and American Cities. *Water, Air and Soil Pollution: Focus* **2(5-6)**: 459-469.

Raupach MR. 1994. Simplified expressions for vegetation roughness length and zero-plane displacement as functions of canopy height and area index. *Boundary Layer Meteorology* **71**: 211–216.

Raupach MR. 1995. Corrigenda. *Boundary Layer Meteorology* **76**: 303–304.

Verma SB. 1989. Aerodynamic resistances to transfer of heat, mass and momentum in estimation of areal evaporation. *IAHS Publications* **177**: 13-20.

Xu W, Wooster MJ, Grimmond CSB. 2008. Modelling of urban sensible heat flux at multiple spatial scales: A demonstration using airborne hyperspectral imagery of Shanghai and a temperature–emissivity separation approach, *Remote Sensing of Environment* **112**: 3493-3510.

3 Estimation of band reflectance using data from remote sensors

The estimation of the reflectance from a rough surface from a remote position is not straightforward. As soon as a surface is not completely smooth, and this is the majority of all surfaces, roughness elements arouse directional effects in the measurement of the reflectance. These effects are triggered by different illumination and shade patterns caused by roughness elements and different transmission grades of the surface or the surface cover. Such effects are present on various spatial scales. A rough acre for example will pose similar effects like a rough urban surface, just on a different spatial scale. The illumination pattern is directly dependent on the position of the sun. Low altitude induces long, high altitude short shadows. Further the pattern is dependent on the percentage of diffuse irradiance of the global irradiance, as diffuse irradiance is the main source of illumination in shaded areas. Multiple reflections from neighbouring rough elements further diversify the pattern. Given this ever-changing illumination pattern, the spatial scale is deciding on the resulting measurement value. A medium-scale radiometer with a spatial resolution of about 100 m sensing an urban surface will depict a mixture of differently illuminated roads, walls and roofs. A high-resolution sensor with a spatial resolution of 1 m in turn will depict only the single elements and therefore sense various different albedos.

Furthermore, sensing the same surface from different angles will automatically result in different reflectances: The surface is not isotropic. The concept describing this phenomenon is the BRDF (Bi-Directional Reflectance Distribution Function). While much work has been invested in describing the BRDF from natural surfaces with small-scale roughness elements, the urban surface is underrepresented in literature. Following two chapters highlight the phenomenon. Chapter 3.1 describes a study where different illumination patterns were modelled in an urban area and their effect on remotely sensed reflectances was analyzed. The study area of this research is the city of Basel, Switzerland. The structure of the city is comparable to some upper middle-class quarters of Cairo, like Mohandiseen. The reason for this choice was the unavailability of a extended high-resolution city model of Cairo. Chapter 3.2 describes the BRF (Bi-Directional Reflectance Function) of urban surfaces in Cairo using CHRIS/PROBA data.

3.1 Geometry effect on the estimation of band reflectance in an urban area

Corinne Frey, Eberhard Parlow, E.

Published in Theoretical and Applied Climatology 96: 395-406

ABSTRACT: *Reflectance of the urban surface is an important factor for urban climate studies and can be assessed using standard remote sensing applications. However, no application considers the three-dimensional structure of the city surface and its resulting shading patterns or the inclined roof surfaces. To determine the effect of these factors on the estimation of urban surface reflectance, a high-resolution raster-based city-surface model was used to estimate the spatial solar irradiance in an example city, namely Basel in Switzerland. Eight times daily for 1 year, the solar irradiance was calculated using MODTRAN and the illumination geometry of the city. Subsequently, the spatial distribution of the solar irradiance, as well as the error in assumed reflectance values were analysed. The error in estimation of reflectance increased with lower solar elevation angle, so its maxima were found in winter. Higher visibility of the assumed atmosphere also increased the estimated error due to the lower proportion of diffuse irradiance. The error decreased with coarser spatial resolution of the pixel.*

3.1.1 Introduction

The albedo is an important parameter for urban climate studies. It determines how much incoming solar irradiation is absorbed by the surface and is made available for other energy fluxes. It is often assessed using remote-sensing methods (Brest 1987; Sailor 1995; Taha 1997). In this context, among the most commonly used satellites are the ASTER (Advanced Spaceborne Thermal Emission and Reflection Radiometer), the LANDSAT TM and ETM+ and also the SPOT sensor (Satellite Pour l'Observation de la Terre) (Chrysoulakis 2003; Frey et al. 2007; Hafner and Kidder 1999; Small 2005; Soler and Ruiz 1994). Singleband albedos are often directly derived from top of the atmosphere radiances using look up tables (LUTs) containing information about the composition of the atmosphere, which is done, for example, for the ASTER surface reflectance product (NASA 2007a). Elsewhere, the albedos are calculated by building a ratio between otherwise corrected image radiances and the modelled solar irradiance, as proposed in the LANDSAT handbook (NASA 2007b). Some groups used digital elevation models for the correction of the spatial irradiance due to topographic effects of the terrain (Parlow 1996; Rigo and Parlow 2007).

Estimating the albedo from space always means compromising, as the spatial resolution of the sensor is too large to optimally resolve the observed features in many cases. The pixels are a mixture between different features and surface materials. Therefore, the albedo of urban areas is strongly determined by the urban setting. Urban areas can be characterised by their geometrical structure. They consist of a mixture of houses, blocks and streets of different forms and sizes on one hand, and of diverse surface materials on the other hand. In between, urban vegetation occurs, modifying the urban climate through its altered surface characteristics. Additionally to this effect the three-dimensional geometry of cities has an impact on the estimation of the urban albedo. Solar irradiation impinges on various surface inclinations, defined by the roof's slopes and aspects. Shading effects lead to very dark surfaces, lowering the satellite estimated albedo considerably. Neither of the approaches accounts for the effect of these urban settings.

A literature survey shows that some research has been conducted in this field already. Aida (1982a) analysed the relation between urban albedo and the solar zenith angle using a model experiment with concrete blocks in cubic form. Aida and Gotoh (1982b) deepened their understanding using a two-dimensional urban block-canyon array model. They showed that the urban albedo is low when the solar zenith angle is also low. Kondo et al. (2001) showed the same, using a modelling approach with simplified three dimensional buildings of equal size, arranged in a regular lattice. Both groups modelled the albedo very accurately and described its behaviour with changing environmental parameters. However, they did not analyse the resulting magnitude of the error in albedo estimation, while ignoring the fact of the urban setting. Finally, Sailor and Fan (2002) used Monte Carlo style simulations with different urban land-use classes for describing the diurnal variability of the effective albedo for cities and they included the effects of shading. Analysing their computed transects of reflectance, they found that the nadir-view-albedo underestimates daily solar radiative loads by 11–22%.

From the discussion of shadows in the urban setting, it seems to be reasonable to distinguish between 'local' and 'regional' albedo. Local albedo on one hand means the reflectivity of the surface as it is. It is the reflectivity from a single-surface material. The regional albedo on the other hand includes effects from a broader environment and may include different surface materials and forms, as well as shading effects (compare Schwander et al. 1999).

This analysis shall be a further step in the understanding of the urban albedo pattern. It aims to analyse if there is a significant geometry effect on the reflectance estimation for the sample urban area, Basel. Mainly the effect of shading from buildings and constructions at different solar

elevation angles and different atmospheric states shall be analysed. To this end, several scenarios are modelled using a radiative transfer model and simple geometric relations as discussed in section Estimation of spatial irradiance and single-band albedo. The results of this pure modelling study are statistically analysed and presented. The results are also aggregated towards increasingly coarser spatial resolutions to see at which ground resolution the pixel shading effects cease to have influence. All the modelling assumes that the satellite acquisition would be only nadir-viewing.

3.1.2 Study area

Study area is Basel, a city with about 200'000 inhabitants. Basel is situated in the north-western corner of Switzerland at the bend of the River Rhine. The River Rhine is the natural border to Germany (Baden-Württemberg) in the north. In the west, the city of Basel is bordered by France (Alsace). Basel is a typical European mid-latitude city with building types ranging from detached houses to blocks and skyscrapers. It includes an old commercial inner city, modern business districts, industrial areas as well as various residential areas on different socio-economic levels.

Basel area was chosen, because it is a representative urban site in the centre of Europe and the urban climate project BUBBLE, the Basel-Urban-Boundary-Layer-Experiment, an internatio-nal joint research activity, was carried out in Basel offering a unique archive of measured micrometeorological data (Rotach et al. 2005). Basel features typical mid-European urban characteristics; therefore, the approach used in this research can be used also for other mid-European cities.

3.1.3 Data

A digital city surface model of Basel was used. The model was obtained from the authorities of the Grundbuch- und Vermessungsamt in Basel, Switzerland. A vector-to-raster conversion had to be performed, before using the model. The resulting raster model has a spatial resolution of 1 m and depicts the buildings of the inner city of Basel without vegetation. The model height is absolute; the Earth surface is considered to be zero. The vertical step height of the model is 1 m.

Furthermore, a QUICKBIRD image was used for the discrimination of urban vegetation. QUICKBIRD is a commercial satellite for Earth observation from Digital- Globe that is operated in the panchromatic with 60-cm spatial resolution and in the multispectral mode with 2.4 m spatial resolution. Four spectral channels (blue, green, red and near-infrared) are available in the multispectral mode. The city surface model was geo-located with this QUICKBIRD image of the same area to enable joint analysis.

3.1.4 Estimation of spatial irradiance and single-band albedo

In the following section, the methods of this analysis are presented. The albedo is defined in the first subsection, while the second section contains the equations for the geometric relations that use various irradiance terms. Finally, in the third section, the modelling of these single irradiance terms is explained and some comparisons with real measured data are made.

3.1.4.1 Definition of albedo

The spatial surface single-band albedo in the wavelength range from λ_1 to λ_2 is defined as a measure of the fraction of radiance reflected from a surface compared to the solar irradiance within the same wavelength range:

$$\boldsymbol{\rho}(\Delta\boldsymbol{\lambda}) = \frac{\boldsymbol{L_r}(\Delta\boldsymbol{\lambda})}{\boldsymbol{L_g}(\Delta\boldsymbol{\lambda})} \qquad (56)$$

ρ = Single-band surface albedo from λ_1 to λ_2

L_r = Irradiance reflected from the Earth surface and integrated from wavelength λ_1 to λ_2 [$Wm^{-2}sr^{-1}\mu m^{-1}$]

L_g = Global irradiance, integrated from wavelength λ_1 to λ_2 (beam plus diffuse irradiance) [$Wm^{-2}sr^{-1}\mu m^{-1}$]

$\Delta\lambda$ = Wavelength range from λ_1 to λ_2

The estimation of the albedo, using this typically applied approach, is done without considering the spatial heterogeneity of the irradiation. However, the global irradiation is dependent on the sun–surface geometry and considerable variations can be observed, especially in mountainous terrain as well as in urban areas (Parlow 1998). The single-band albedo in the spatial domain is therefore calculated best using spatially distributed irradiance values. In the following, the term single-band albedo is addressed simply as albedo.

It is important to find out at what height the involved irradiance terms are modelled or measured. If the considered heights are just above the surface, then the resulting albedo belongs to the local surface type and the albedo can be referred to as a local albedo (Christen and Vogt 2004). However, if the measurement is high enough to "see" different local surface types, then one may address the resulting albedo as regional albedo.

3.1.4.2 Geometric relations

The solar irradiance of a spectral band is given as the sum of beam irradiance, diffuse irradiance, and irradiance reflected from the environment (adjacency effects) of this spectral band.

$$L_{g\_sunlit}(x,y) = L_b \cdot \cos\alpha(x,y) + L_d \cdot svf(x,y) + L_r(x,y) \quad (57)$$

α = Illumination angle [º]

$L_{g\_sunlit/shaded}$ = Global irradiance in sunlit or shaded area, integrated from wavelength λ_1 to λ_2 [$Wm^{-2}sr^{-1}\mu m^{-1}$]

L_b = Beam irradiance, integrated from wavelength λ_1 to λ_2 [$Wm^{-2}sr^{-1}\mu m^{-1}$]

L_d = Diffuse irradiance, integrated from wavelength λ_1 to λ_2 [$Wm^{-2}sr^{-1}\mu m^{-1}$]

L_r = Irradiance reflected from the environment, integrated from wavelength λ_1 to λ_2 [$Wm^{-2}sr^{-1}\mu m^{-1}$]

svf = Sky view factor (0-1)

In shaded areas the beam radiation is dismissed and the equation writes:

$$L_{g\_shaded}(x,y,\alpha) = L_d \cdot svf(x,y) + L_r(x,y) \quad (58)$$

The expression of the diffuse irradiance was taken from Liu & Jordan (1963) and Hofierka & Šúri (2002).

The global irradiance is dependent on the illumination angle (the solar zenith relative to the Earth surface and azimuth angle relative to a given direction, here east of north) as seen in Equation (57). In case of horizontal surface this angle is simply the solar zenith angle. In case of an inclined surface, the illumination angle can be calculated as (Liu and Jordan 1963; Iqbal 1983; Chrysoulakis et al. 2004):

$$\cos\alpha(x,y) = \cos\Theta_s \cdot \cos\Theta_n(x,y) + \sin\Theta_s \cdot \sin\Theta_n(x,y) \cdot \cos\{\Phi_s - \Phi_n(x,y)\} \quad (59)$$

Θ_s = Solar zenith angle [º]

Θ_n = Terrain slope [º]

Φ_s = Solar azimuth angle [º], (East of North)

Φ_n = Aspect or topographic azimuth [º], (East of North)

The terrain slope (Θ_n) and the topographic azimuth (Φ_n) have to be calculated separately. The topographic azimuth was estimated using a routine in the topographic modelling menu of the digital image analysis software package ENVI. The terrain slope could also be calculated in this menu; however, for the city surface model, the ENVI routine is not applicable, as it includes the building walls in its calculations and it does not consider small-scale changes. Therefore, a separate routine was developed, which accounts only for the slopes on the rooftops.

The irradiance reflected from the environment is calculated using following parameterisation:

$$L_r(x,y) = L_g(x,y) \cdot \rho_s(x,y) \cdot \left(1 - svf_{x,y}\right) \quad (60)$$

ρ_s = Smoothed albedo of the Earth surface

L_g = Global irradiance, integrated from wavelength λ_1 to λ_2 [$Wm^{-2}sr^{-1}\mu m^{-1}$]. Corresponds to the term $L_{g\_sunlit/shaded}$ of Equation 57.

The reflected irradiance term stands for the radiation that is reflected by the environment of the pixel and is calculated iteratively. A first estimate of the global irradiance (equations 57 and 58) is used to calculate the reflected irradiance, which is then used to update the global irradiance. This process is repeated several times. The used albedo (the top of the atmosphere albedo) was smoothed first for usage in the adjacency-effects estimation.

The sky view factor describes the proportion of the upper hemisphere that is 'seen' from a pixel. The sky view factor ranges from 0 to 1. It is calculated by a routine, which is adapted from Dozier et al. (1981). First, the routine searches the limiting horizon angle for each pixel and for a given set of directions (36 directions resulting in degree steps of 10°). The angle is determined by simple trigonometry between the corresponding two pixels. For each pixel, a set of n angles, representing the circular horizon, is determined via this process. This dataset, consisting of number of pixels multiplied by the number of directions elements, is used later for the computation of shaded pixels. Secondly, the routine averages the horizon angles of each pixel. This average represents the horizon view factor (*hvf*), from which the sky view factor can easily be derived.

Shaded areas have to be determined firstly to calculate the irradiance in the spatial domain. This is done comparing the horizon angle in the direction of the sun azimuth to the solar elevation angle pixel by pixel. If the solar elevation angle is lower than the horizon angle, the pixel is marked as shaded.

3.1.4.3 Estimation of the irradiance terms

The estimation of the diffuse irradiance can be done using a parameterisation linking the clearness index c (global irradiance/exo-atmospheric irradiance) with the diffuse fraction (diffuse irradiance/global irradiance). For example the parameterisation from Erbs et al. (1982) is

For c < 0.22

$$L_d = (1.0 - 0.09 \cdot c) \cdot L_g$$

For c >= 0.22 and for c < 0.8

$$L_d = (0.9511 - 0.1604 \cdot c + 4.388 \cdot c2 - 16.638 \cdot c3 + 12.336 \cdot c4) \cdot L_g$$

For c > 0.8

$$L_d = 0.165 \cdot L_g \quad (61)$$

The beam and diffuse irradiance can then be computed following:

$$L_b = L_g - L_d \quad (62)$$

L_d = Diffuse radiance, integrated from wavelength λ1 to λ2 [$Wm^{-2}sr^{-1}\mu m^{-1}$]

L_b = Beam radiance, integrated from wavelength λ1 to λ2 [$Wm^{-2}sr^{-1}\mu m^{-1}$]

This parameterisation works well around noon but failed in the case of very low sun elevation angle, since in the early morning and the late afternoon the percentage of diffuse irradiance of the global irradiance is very high. Another parameterisation that works similar is from Maxwell (1987). What is more straightforward, is to take the diffuse irradiance values directly produced by the atmospheric transfer code, in this case MODTRAN (MODerate spectral resolution atmospheric TRANSmittance algorithm and computer model). MODTRAN was developed by AFRL/ VS (The Air Force Research Laboratory, Space Vehicles Directorate) in collaboration with Spectral Sciences, Inc. (Berk et al. 1999). It calculates atmospheric transmission, atmospheric background irradiance, single-scattered solar and lunar irradiance, direct solar and lunar irradiation, and multiple-scattered solar and thermal radiance for any point in the atmosphere and for any path within the atmosphere for frequencies from 0 to 50,000 cm−1.

However, recently the question arose as to whether MODTRAN overestimates the diffuse irradiance (see Halthore and Schwartz 2000; Henzing et al. 2004). Both studies compare in situ measurements of clear sky beam and diffuse irradiation with MODTRAN results, using accurate aerosol surface measurements for model input. While the beam irradiation was modelled well in both studies, the diffuse irradiation was overestimated, in average 25 Wm−2 (Henzing et al. 2004). Despite this, MODTRAN results were used for this study. The conclusions from a comparison of MODTRAN results and in situ measured radiances presented in the following explain this choice. Figure 37a shows the global and the diffuse irradiation, measured at the MeteoSuisse station 'Davos' (an alpine station at 1,590 m asl) and 'Payerne' (a lowland station at 491 m asl) by CM21 sensor from Kipp and Zonen on 14 December 2001.

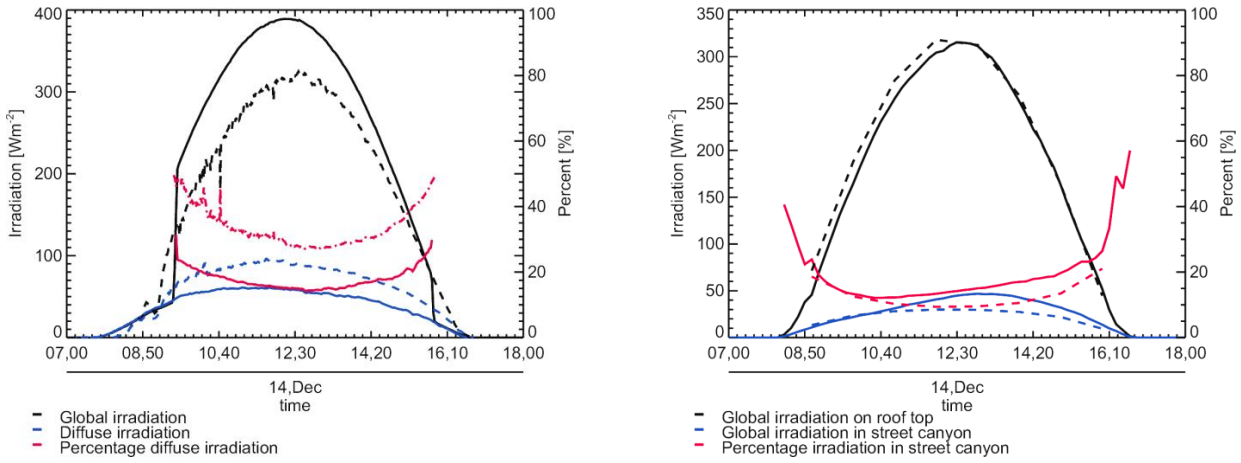

a) b)

Figure 37 a) Global and diffuse radiation measurement at Davos (solid line) and Payerne (dashed line) (source MeteoSwiss) b) Global irradiance during the course of a day. The solid line shows the results of the measurement using a CNR. The dashed line shows the modelling results using a mid-latitude winter atmosphere with no aerosol attenuation. In both figures the blue line shows the percentage of the diffuse irradiation or the irradiation in the street canyon versus the global irradiation

The solid line shows data of the station 'Davos' on a clear and bright day. In Payerne, there must have been a few translucent clouds, reducing the solar irradiation. The diffuse irradiation amounts for 15, respectively 30% of the global irradiation at noon. This example points out that the diffuse irradiation is highly variable, depending on, besides altitudinal effects, the possible atmospheric compositions. The solid lines of Figure 37b show irradiation values measured by the Institute of Meteorology, Climatology and Remote Sensing of the University of Basel at the urban site 'Sperrstrasse', which is located inside the area of interest of this analysis (Rotach et al. 2005; Christen and Vogt 2004). Two radiation sensors were used for the measurements: a CNR1 from Kipp and Zonen on top of a tower, seeing only the upper hemisphere and a CM11 also from Kipp and Zonen, which was installed inside the street canyon and was shaded during the whole day on 14 December 2001. The dashed lines depict the modelled values, using the already-described procedures and MODTRAN at the same spots where the sensors were installed during the measurements. The MODTRAN standard winter mid-latitude atmospheric profile was used together with the 'no aerosol attenuation' option. The curves of course do not agree perfectly as the actual atmospheric profile is not known. However, they show that the parameterisation of the irradiation of the shaded areas lies in an acceptable range. Attention should be paid to the fact that the percentage of diffuse irradiance increases strongly with very low sun elevation angles.

In this paper, diffuse irradiances from MODTRAN are used despite the already-mentioned restrictions, as, firstly, MODTRAN considers the variable percentage of the diffuse part of the global radiation, and, secondly, the modelling does not reproduce real annual patterns, but does, however, assume a fixed standard atmosphere with no clouds. This assumption is necessary, as in optical remote sensing only clear and bright days can be used to estimate the surface albedo. To account for different states of the atmosphere the runs were performed fourfold with different aerosol models (option IHAZE in the MODTRAN model):

1. Urban aerosols, visibility 5 km
2. Rural aerosols, visibility 23 km
3. Only tropospheric aerosols, visibility 50 km
4. No aerosol attenuation

The first assumption stands for a very heavy loaded atmosphere, where the diffuse part of the global irradiance is very high. The third assumption represents extremely clear days with the diffuse part being very small. The second assumption is midway between the other two extremes and may account for most clear and sunny days in Basel. The fourth assumption assumes that there is no attenuation by aerosols. The modelled radiances are applied then to equations 57–60 to distribute them in the spatial domain as described in the section Geometric relations.

The already-described approach of calculating spatial irradiance values is simple and applicable in large areas without requiring much CPU computing time. The spatial irradiance can be calculated easily for large areas to get input data for the modelling of the surface albedo. However, the simplifications of the reflection term may not be optimally suited for urban areas. The reflection term assumes that the surrounding pixels are all equally illuminated. Of course this is not the case as, on the contrary, there might be extremely illuminated and completely shaded walls, contributing to the intensity of the irradiation and therefore also influencing satellite derived albedo products. Their contribution is dependent on the pixel location. A better estimation can be given by ray-tracing models, which are far more complex and elaborate. The disadvantage of these models is the computing time. For large areas like the city of Basel, such an approach is not feasible yet.

In this paper, firstly the spatial distribution of irradiance in the urban area of Basel is analysed for a whole year and 8 times a day at 09:00, 10:00,

11:00, 12:00, 13:00, 14:00, 15:00, and 16:00 hours. For each time slot, the atmospheric transfer code MODTRAN was run and the global irradiance per wave number was extracted, which is the standard output of MODTRAN. Often satellite data are integrated irradiances per micron [$Wm^{-2}sr^{-1}\mu m^{-1}$], like, for example, the ASTER images, which are dependent on the spectral response of the sensor. Therefore, the MODTRAN output irradiances were initially converted from irradiances per wave number into irradiances per micron using the following relationship (Schläpfer and Odermatt 2006):

$$L_\lambda[Wm^{-2}sr^{-1}\mu m^{-1}] = \nu^2[(cm^{-1})^2] \cdot L_\nu[Wcm^{-2}sr^{-1}cm] = \nu^2 \cdot L_\nu[Wm^{-2}sr^{-1}\mu m^{-1}] \quad (63)$$

Then the irradiances belonging to band *i* (here ASTER band 1) were convolved with the spectral response *r* of the sensor for band *i*, according to the following expression:

$$L_i = \frac{\int L(\lambda)\cdot r_i(\lambda)d\lambda}{\int r_i(\lambda)d\lambda} \approx \frac{\sum_{n=\lambda_1}^{\lambda_2} L(\lambda_n)\cdot r_i(\lambda_n)\Delta\lambda_n}{\sum_{n=\lambda_1}^{\lambda_2} r_i(\lambda_n)\Delta\lambda_n} \quad (64)$$

The spectral response for the ASTER band 1 was first interpolated for each wave number using the values available from the ASTER homepage to fit them to the MODTRAN irradiance output. Secondly, an image with local albedos was created. The albedos were determined according to the land use of the pixel. The classes 'roof', 'street', 'vegetation' and 'water' were determined using the city-surface model and the *NDVI* (normalised difference vegetation index) from the QUICKBIRD image. This image refers to the local albedos as measured at the ground surface. For the roof class, the value of 0.15 was applied; for street, 0.07; for 'vegetation', 0.1; and for 'water', 0.05. Using this image, the reflected irradiance was estimated using the spatial irradiance and the local albedos. This reflected irradiance was later used for the assessment of the error in albedo estimation. The *NDVI* was calculated using band 3 and band 4 from QUICKBIRD. Attention should be paid to the fact, that the local albedos consider only the surfaces seen from nadir view. Other parts, which also form part of the city surface, like walls, are not included in this analysis.

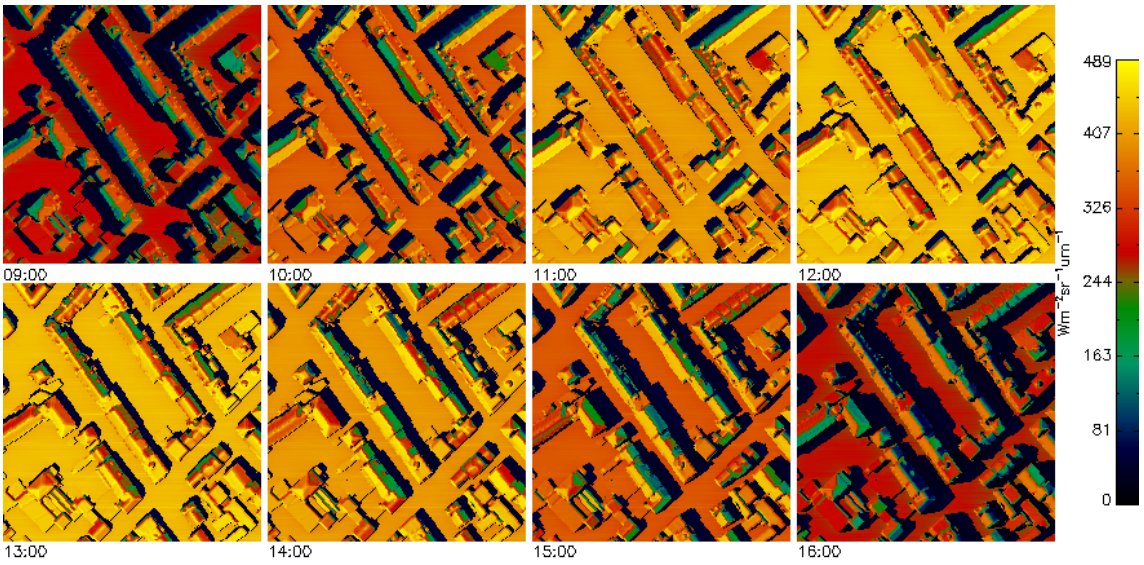

Figure 38 Small section of the city surface model. It shows the incoming irradiance [$Wm^{-2}sr^{-1}\mu m^{-1}$] from 12th June 2001, convolved for ASTER band 1. The model was run with the rural standard atmosphere, 23km visibility.

The estimated albedos were computed as the ratio between the before mentioned reflected irradiances and one single value for the global irradiance: the irradiance on a horizontal plane. These modelled 'regional' albedos stand for the albedo as calculated using satellite images for input - not taking into account the spatial structure of the city.

3.1.5 Results

The results of this analysis are presented in two ways: first, the results of the spatial irradiance modelling is examined; and, secondly, the consequences of this modelling on the albedo estimation are presented.

3.1.5.1 Modelling of spatial irradiance

The spatial irradiance shows very strong spatial patterns in the urban area. The irradiance of shaded pixels consists only of the reflected and diffuse part, which is quite low, compared to fully sunlit pixels. Highest absolute differences between the pixels of the image are found on summer days, as the solar irradiation is very strong during this time. Very high differences are also found in winter when the sun altitude is very low and shadows are the largest. Figure 38 shows the spatial irradiance of a part of the city surface model on 12 June 2001 at the 8 time steps of modelling using the rural aerosol model of MODTRAN with visibility of 23 km. While the scenes around midday are very bright with only small parts shaded, the morning and early evening scene features long dark shadows. The images highlight the effect of inclined rooftops. Rooftops facing the sun are the brightest spots in the images, while the opposite rooftops have much lower irradiance values, even if they are not shaded. The average differences of the whole area of the city surface model depend on the time and day of the year.

Figure 39 shows the average differences of the modelled irradiance to the irradiance incident on a horizontal plane in a rural atmosphere, 23 km visibility - in percentage of the irradiance incident on a horizontal plane. The differences are defined as the absolute mean difference (*MAD*) and are calculated as follows:

$$MAD = \frac{1}{n}\sum_{I=1}^{n}\left(\left|L_{g\_i} - L_{g\_horizontal}\right|\right) \qquad (65)$$

MAD = Mean absolute difference

L_{g_I} = Global irradiance at ith pixel, integrated from wavelength λ_1 to λ_2 [Wm^{-2}sr^{-1}µm^{-1}]

$L_{g\_horizontal}$ = Global irradiance on a horizontal plane, integrated from wavelength λ_1 to λ_2 [Wm^{-2}sr^{-1}µm^{-1}]

The strong annual dependency of the differences has the shape of a modified sinuous curve. In winter, in the hours around noon, the differences are highest, produced by a lower sun altitude and the long shadows. In summer, the differences are much smaller. Only in the morning and the evening hours (09:00 and 16:00), when the sun is even lower, the differences are lowest in winter. This is due to the strong increase in the percentage of diffuse radiation at very low sun altitudes as can be seen in Figure 38.

The differences are lowest in winter which is due to the strong increase in the percentage of diffuse radiation at very low sun altitudes. At all times, the annual courses show a faint zigzag pattern. This pattern is produced by the 1-m resolution of the city surface model. Each time, the curve slightly drops or rises, the modelled shadows from the buildings were extended or shortened about one pixel. Figure 39a shows the absolute mean difference (*MAD*) in percentage for the whole available city model, Figure 39b shows the error for a selected area of Basel (500×500 m), which is characterised by its dense housing. It is a larger area than the example in Figure 38, and shall document how the results are changing for a specific type of urban buildings. For these figures, the rural aerosol model, visibility 23 km, was used.

The magnitude of the *MAD* strongly depends on the applied aerosol model. While the *MAD* is minimal for the urban 5-km visibility model, it is maximal for highest visibility (no aerosol attenuation).

Table XV shows the annual *MAD* for the three models for each hour. Input for the data is the whole city model. For the densely built up area, the values are 1.2–1.3 times higher than for the whole city area.

The strong spatial pattern of the urban fabrics produces a high standard deviation for the already-mentioned *MAD*s. The standard deviations of the *MAD* in irradiation estimation have similar magnitudes to the averages. For example, the two annual courses of 09:00 and 16:00 show highest standard deviations in summer but lower values in winter. All other curves have two peak maximums in spring and autumn and show a little depression in summer. All curves stay below 29.1% for the whole area and below 30.2% for the densely built-up urban area during the whole year (rural aerosol model, visibility 23 km). In the case of the 'no aerosol attenuation model', the numbers are 69.0%, and 67.0% respectively.

Table XVI addresses the different results produced by the four aerosol models. The lowest standard deviations are found at the lowest visibility (5 km), the highest at the highest visibility (no aerosol attenuation); however, here the differences between the small densely built up area and the whole city model are very low, only the values for the whole city model are given.

In the preceding tables and figures, the absolute mean is considered for the estimation of the error. This means that negative differences are treated as positive values in the calculation of the mean. There are two main sectors, where highest differences occur. The first sector is where shaded pixels appear. There, the modelled irradiance is much lower than the irradiance on a horizontal plane. A second much smaller sector includes the inclined rooftops, which are almost perpendicular to an imaginary roof-sun line. There, very high intensities occur which are higher than the irradiance on a horizontal plane. A major part of the pixels show only very small differences. They include horizontal areas like unshaded streets, horizontal roofs and green parks.

The normal means of the differences (*MD*), including positive and negative pixels, are lower than the absolute means over the whole course of the year. The two extreme sectors already-mentioned in the preceding paragraph partly cancel out each other. The *MD* range, in the case of 23-km visibility ranges from 11.1% (12.00) to 13.2% (15:00) for the whole area and from 23.9% (12.00) to 28.0% (15:00) for the densely built-up urban area. The standard deviations range from 23.3 to 25.0% for the whole area and from 28.4 to 32.3% for the densely built-up urban area. These lower mean errors imply that if the area that represents a pixel is large enough, even though the standard deviations are higher, the differences might be small enough to be ignored.

The *MD* is calculated as follows:

$$MD = \frac{1}{n}\sum_{i=1}^{n}\left(L_{g\_i} - L_{g\_horizontal}\right) \qquad (66)$$

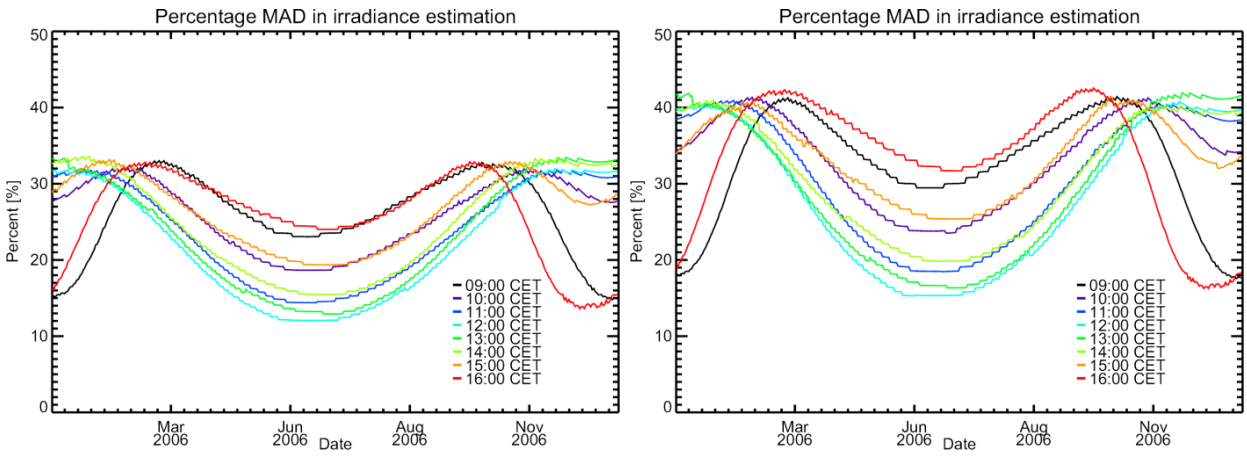

a) **b)**

Figure 39 Percentage of absolute mean error in irradiance estimation of the irradiance on a horizontal plane with the rural aerosol model, visibility 23 km. a) From the whole city surface model, b) from a selected densely built-up area

Table XV Absolute mean error (MAD) in irradiation [%] estimation using the four different aerosol models for the whole urban area. Annual mean values are given.

Time/Visibility	09:00	10:00	11:00	12:00	13:00	14:00	15:00	16:00
5 km	16.6	16.7	16.3	15.8	16.4	16.9	17.0	16.9
23 km	26.1	26.0	23.8	22.2	23.3	25.0	26.5	26.0
50 km	34.2	32.0	28.1	25.8	27.1	29.6	32.7	33.7
No aerosol attenuation	49.0	40.6	34.3	31.0	32.6	36.2	41.8	49.0

Table XVI Standard deviation of MAD in irradiation estimation [%] using the three different aerosol models for the whole urban area. Annual mean values are given.

Time/Visibility	09:00	10:00	11:00	12:00	13:00	14:00	15:00	16:00
5 km	13.4	14.8	15.4	15.4	15.9	15.7	14.9	13.5
23 km	22.2	25.0	25.5	25.1	25.8	25.8	24.9	22.1
50 km	29.7	31.8	31.3	30.4	31.1	31.6	31.6	29.3
No aerosol attenuation	44.7	40.8	38.4	36.7	37.4	38.6	40.7	45.3

This consideration leads to the next step of this analysis: a spatial aggregation series was produced to find the error, which is dependent on the pixel resolution. The spatial resolution of the original image is 1 m. Only integer multiples of the original resolution were used for the aggregation procedure. The aggregated images were downscaled in 1-m steps up to 100-m resolution. No effects of nonlinearity were considered in this process.

The *MD* (not the *MAD*) of the whole city surface model does of course not change with decreasing resolution. Figure 40 shows the *MD* averaged for the whole year at 11:00, 12:00, 13:00 and 14:00 hours. These are the hours where the sun position is still high enough that the diffuse part of the incoming solar radiation stays small. The *MD* stays at 23% for all the resolutions for the atmosphere with a visibility of 23 km. The standard deviation of the annual mean is higher and ranges from 27.9% at 2-m resolution to 5.0% at 100-m resolution. It decreases continuously while the pixel resolution gets coarser; however, the rate of decrease also gets lower with coarser pixel resolution. The annual course of the standard deviations of the *MD* reflects the position of the sun towards the houses. While in summer and winter the standard deviations are relatively small, they increase in spring and autumn. Similarly, the standard deviations decrease towards noon.

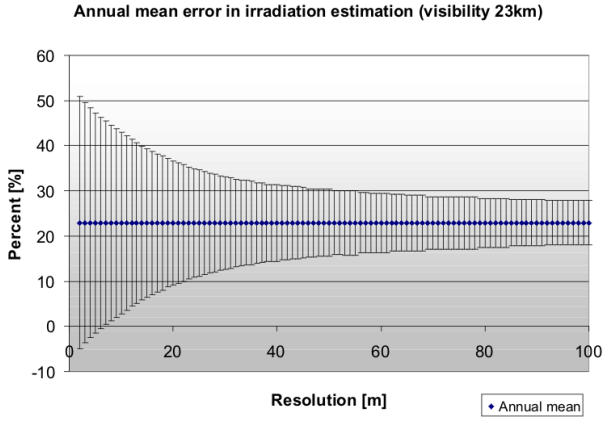

Figure 40 MD of irradiation estimation in percent [%] of the irradiance on a horizontal plane (Mean from the hours from 11:00 to 14:00). Visibility is 23 km.

Figure 41 shows the standard deviation of the *MD* in irradiation estimation in percent of the irradiance on a horizontal plane during the annual course for all calculated points in time from 11:00 to 14:00 and for different resolutions for the rural aerosol model, 50 km visibility.

As already discussed, the standard deviations decrease with the spatial resolution getting coarser. The standard deviations level off at a spatial resolution of about 50 m. Resolutions coarser than 50 m cease to decrease in any significant amount.

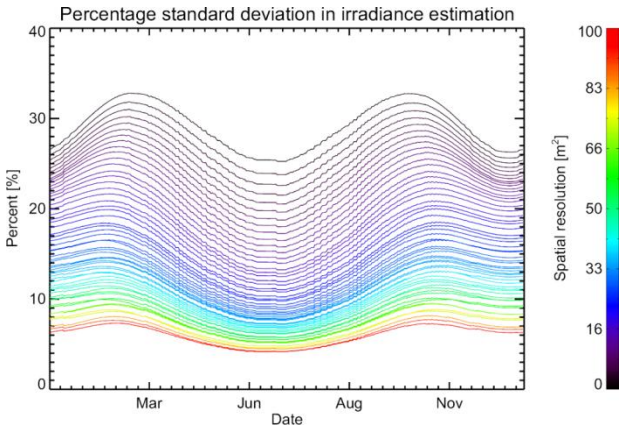

Figure 41 Standard deviation of the MD in irradiation estimation in percent [%] of the irradiance on a horizontal plane of the small densely built-up urban area. (Mean from the hours from 11:00 to 14:00). Visibility is 50 km.

3.1.5.2 Estimation of urban reflectance

Furthermore, the local albedos from the land use classes were compared to modelled regional albedos. These regional albedos were computed reversing the process of creating the reflection image; they are the ratio between the calculated reflected irradiance and one single value for the global irradiance - the irradiance on a horizontal plane. By computing the difference between the two albedos - local albedo minus modelled albedo - the error in albedo estimation can be evaluated.

It was found, that the *MAD* in albedo estimation ranges from 1.5 to 4.1% for the whole area and 1.7

to 5.3% for the densely built-up urban area, calculated for all times and days of the year and for all four atmospheric models. These values are relatively high, as the average albedo of the area of the city model is only 10.3%. This means that in the worst case scenario, the shading effect reduces the urban albedo by almost half of its value. It has to be considered that these percentages are albedo values, and not percentages of the original albedo - otherwise they would be considerably higher. Figure 42 shows the *MAD* in albedo estimation for the whole city surface model and from the selected densely built-up area for the rural model, 23 km visibility.

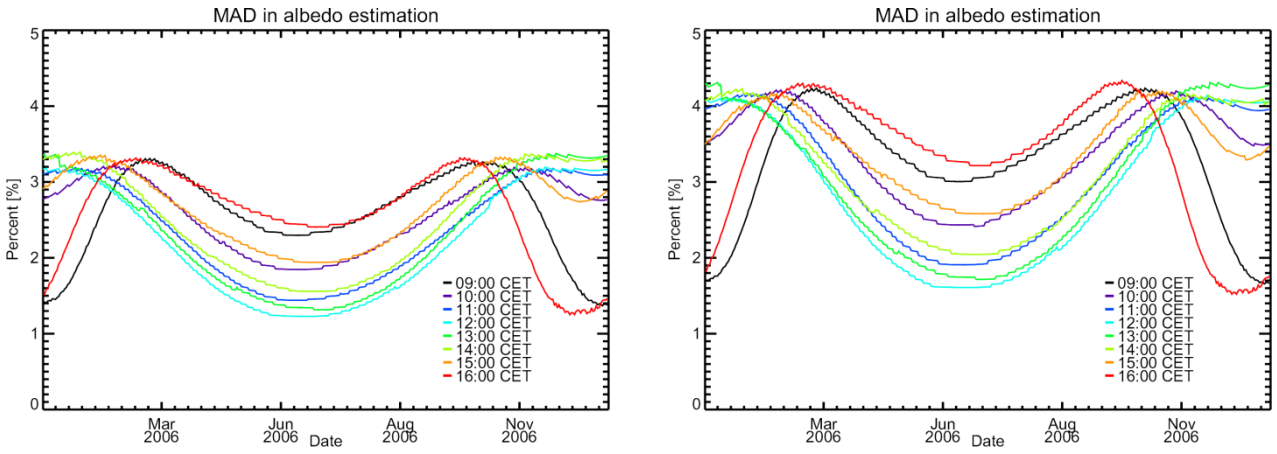

a) b)

Figure 42 MAD in albedo estimation a) from the whole city surface model, b) from a selected densely built-up area. Visibility is 23 km.

Table XVII MAD in albedo estimation [%] using the four different aerosol models for the whole urban area. Annual mean values are given.

Time/Visibility		09:00	10:00	11:00	12:00	13:00	14:00	15:00	16:00
5 km	*MAD*	1.54	1.55	1.52	1.48	1.55	1.60	1.61	1.59
23 km	*MAD*	2.59	2.59	2.36	2.21	2.34	2.51	2.67	2.59
50 km	*MAD*	3.50	3.26	2.85	2.62	2.77	3.03	3.36	3.46
No aerosol attenuation	*MAD*	5.2	4.2	3.5	3.2	3.4	3.8	4.4	5.2
5 km	*Std Dev*	1.26	1.39	1.45	1.46	1.55	1.53	1.45	1.31
23 km	*Std Dev*	2.35	2.63	2.61	2.55	2.66	2.71	2.68	2.38
50 km	*Std Dev*	3.44	3.48	3.29	3.15	3.27	3.38	3.53	3.41
No aerosol attenuation	*Std Dev*	5.6	4.6	4.1	3.9	4.0	4.2	4.7	5.7

Table XVIII Absolute mean error in albedo estimation [%] using the four different aerosol models for the densely built-up urban area. Annual mean values are given.

Time/Visibility		09:00	10:00	11:00	12:00	13:00	14:00	15:00	16:00
5 km	*MAD*	1.93	1.97	1.95	1.90	1.98	2.02	2.04	2.02
23 km	*MAD*	3.32	3.39	3.14	2.90	3.02	3.02	3.42	3.37
50 km	*MAD*	4.5	4.3	3.8	3.5	3.6	3.9	4.3	4.5
No aerosol attenuation	*MAD*	6.6	5.6	4.7	4.2	4.8	4.8	5.6	6.6
5 km	*Std Dev*	1.25	1.42	1.51	1.52	1.59	1.58	1.50	1.31
23 km	*Std Dev*	2.34	2.65	2.69	2.63	2.74	2.79	2.72	2.32
50 km	*Std Dev*	3.5	3.5	3.4	3.3	3.4	3.5	3.6	3.3
No aerosol attenuation	*Std Dev*	5.9	4.7	4.3	4.0	4.1	4.4	4.8	5.7

The annual means of the *MAD* in albedo estimation are given in Table XVII and Table XVIII. They reflect the same pattern as the *MAD* of the irradiance calculation: the better the visibility, the higher the error in the albedo estimation. In the small densely built-up area, the errors are again higher compared to the whole city area.

The standard deviations, also in Table XVII and Table XVIII, are almost as high as the *MAD* and reflect the high spatial variability of the urban fabrics. The *MD*s, including positive and negative pixels, over the whole course of the year are much lower. In the case of the 23-km visibility model, they range from 1.68% (12:00) to 1.91% (16:00) for the whole city area and 2.20% (12:00) to 2.59% (17:00) for the densely built-up area. However, standard deviations of *MD* show a significant annual and daily course as found for the *MD* of the irradiances.

Both the *MAD* and most of all the standard deviations decrease with a coarser resolution. The behaviour of the *MAD* over the course of the year is dependent on the aerosol model. While the urban model (visibility 5 km) shows a two-peak maximum in early spring and late autumn, the other models have highest differences in winter. The lower differences in winter in the urban aerosol model are due to the high proportion in diffuse irradiance. It diminishes the distinction between sunlit and shaded pixels. This high proportion is maximal in winter and superimposes the effect of shading. Also, the differences between the various resolutions are almost zero for the urban aerosol model, while it is maximal for the 'no aerosol attenuation' model (see Figure 43). In summer, when the *MAD* is lowest in all cases, it stabilizes at around 2%. The smoothing effect of the decreasing pixel resolution is best visible in wintertime.

The standard deviations show an undulating pattern, with maximum differences in spring and autumn, except for the 'no aerosol attenuation' model, where the highest differences occur in winter. All models show lower differences with coarser resolution, whereas this effect is as expected to be the lowest for the urban aerosol model (visibility 5 km). For the resolution of 100 m, the standard deviations are lower than 1% in all cases (Figure 44).

3.1.6 Summary and conclusions

Errors in the estimation of irradiance and albedo in an urban area were estimated based on a raster city model and MODTRAN runs. It was found, that the urban fabrics impose a great obstacle in estimating urban albedo from space, due to its diversification in global irradiance. A densely built-up urban area exhibits higher possible errors in the estimation of irradiance and albedo than a general urban area. Therefore, automatically an error arises when estimating the albedo from satellite images with a methodology that does not include any correction for the spatial distribution of the global irradiance.

Furthermore, it was found that the percentage of diffuse irradiance of the global irradiance plays an important role in the magnitude of the error. The higher the part of the diffuse irradiance, the lower is the projected error in the calculation of the albedo. Disregarding the difficulties in correcting satellite images for the atmospheric effects (modelling of path irradiance and transmissivity), it is preferable to estimate the urban albedo on a less clear, but still sunny day, as the diffuse irradiances dilute the sharp contrasts of the shadings.

Due to the shading, resulting from the urban geometry, it is optimal to use images, acquired at a time of highest possible sun-elevation angles. Therefore, the remaining error in albedo estimation in summer is much lower than in winter. In the basic case of 1-m resolution, the *MAD* (mean absolute difference) in albedo estimation was found to be in the range of 1.5 to 7.9% for the densely built-up urban area, as calculated from 11:00 to 14:00 hours each day of the year for all four atmospheric models.

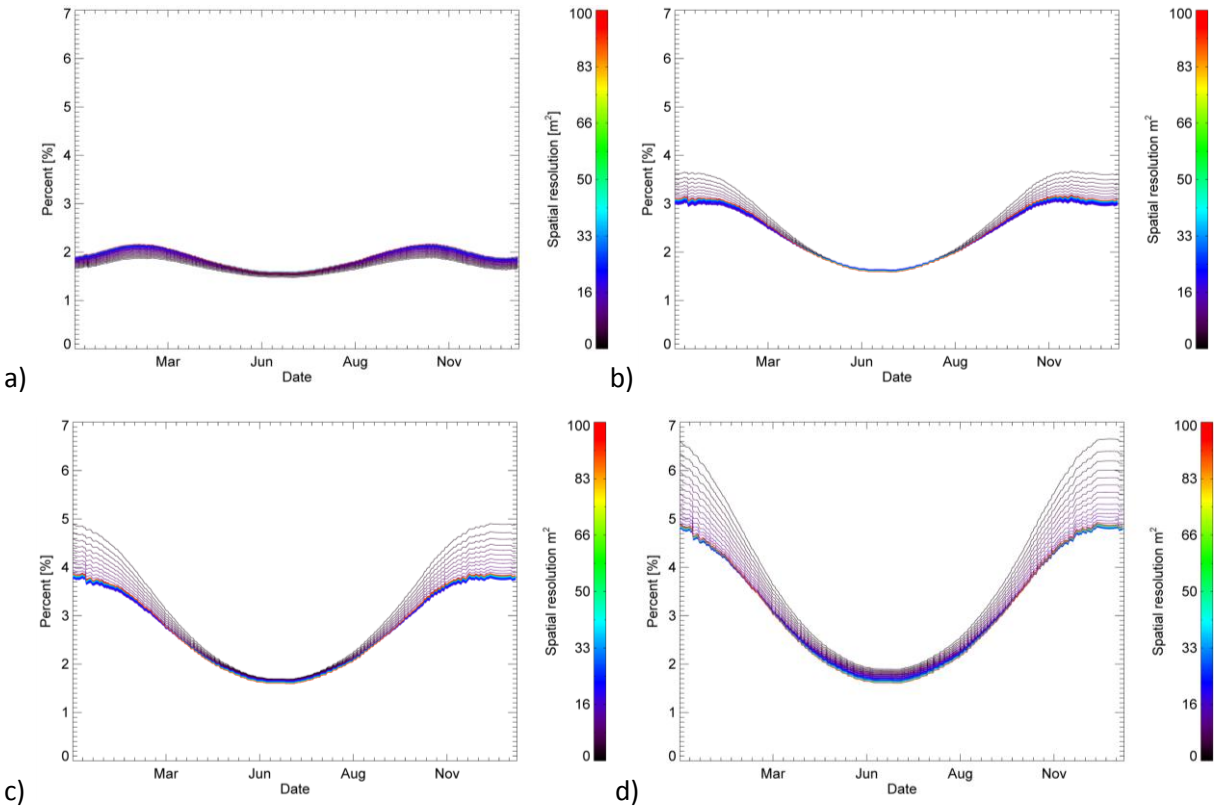

Figure 43 MAD in albedo estimation from a selected densely built-up area. a) Urban aerosols, visibility 5km, b) rural aerosol, visibility 23km, c) only tropospheric aerosols, visibility 50km, d) no aerosol attenuation

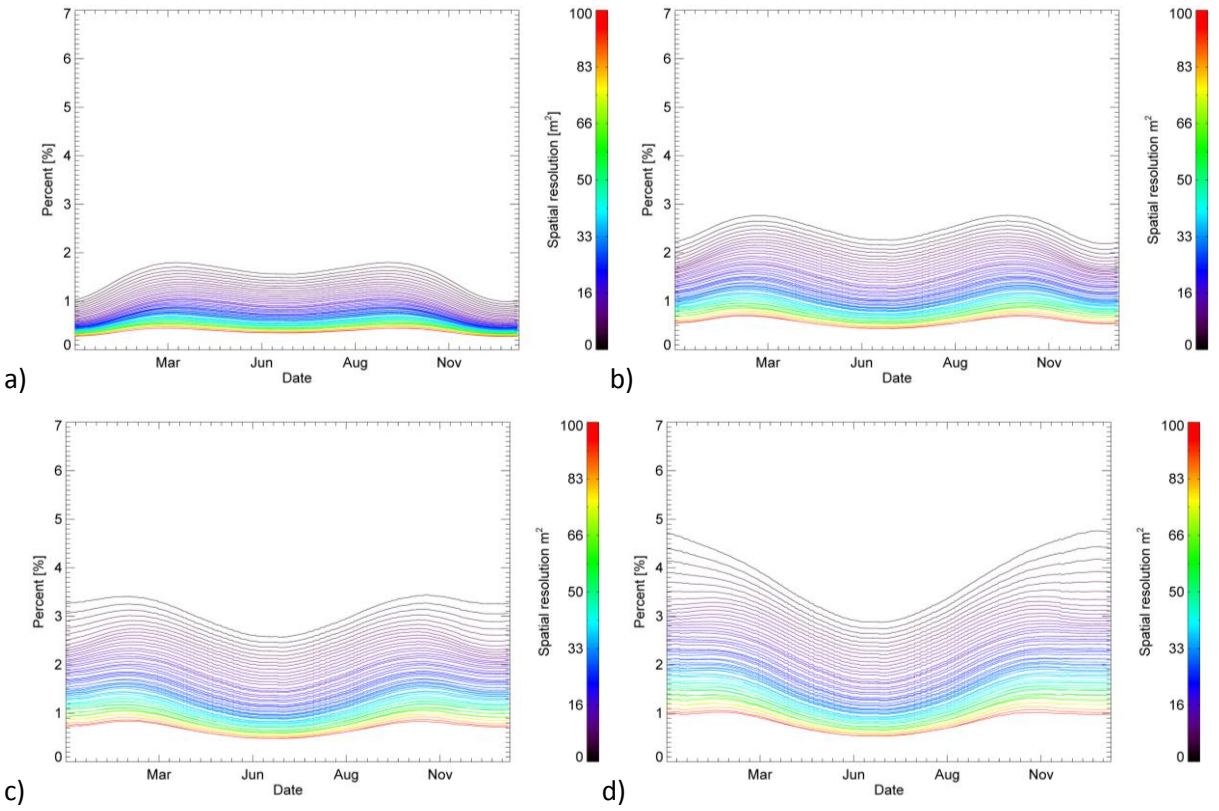

Figure 44 Standard deviation of MAD in albedo estimation from a selected densely built-up area. . a) Urban aerosols, visibility 5km, b) rural aerosol, visibility 23km, c) only tropospheric aerosols, visibility 50km, d) no aerosol attenuation

Considering that the assumed average albedo is 10.3% only, the *MAD* can be higher than half of the albedo value itself.

These differences decrease with coarser spatial resolution, as very strong illuminated surfaces such as sun-direction declined roofs compensate for part of the error resulting from the shaded surfaces. In an area where only flat roofs occur, this effect would not be present. In the case of the 100-m aggregated pixels, the *MAD* in albedo estimation in the densely builtup urban area was found to be much lower - in the range of 0.4 to 4.2% from 11:00 to 14:00 hours each day of the year for all four atmospheric models.

3.1.7 Acknowledgements

We thank the Federal Office of Meteorology and Climatology (MeteoSwiss) for providing us the irradiation data of the stations Davos and Payerne, Switzerland. This research was conducted partly at ESA-ESTEC, Noordwijk, The Netherlands. The authors appreciate the kind support of Michael Berger. This project was funded by the Swiss Science Foundation with grant No. 200021-109472.

3.1.8 References

Aida M. 1982a. Urban albedo as a function of the urban structure - A model experiment. *Boundary-Layer Meteorology* **23**: 405–413.

Aida M, Gotoh M. 1982b. Urban albedo as a function of the urban structure - A two-dimensional numerical simulation. *Boundary-Layer Meteorology* **23**: 416–424.

Berk A, Anderson GP, Bernstein LS, Acharya PK, Doethe H, Matthew M.W, Adler-Golden SM, Chetwynd JH, Richtsmeister SC, Pukall B, Allred CL, Jeong LS, Hoke ML. 1999. MODTRAN 4 radiative transfer modeling for atmospheric correction. *Proceeding, Optical Spectroscopic Techniques and Instrumentation for Atmospheric and Space Research III* **3756**, Denver CO, July 1999, SPIE, Bellingham, WA, USA: 6.

Brest CL. 1987. Seasonal albedo of an urban/rural landscape from satellite observations. *Journal of Applied Meteorology* **26**: 1169–187.

Christen A, Vogt R. 2004. Energy and radiation balance of a central European city. *International Journal of Climatology* **24** 1395–1421.

Chrysoulakis N. 2003. Estimation of the all-wave urban surface radiation balance by use of ASTER multispectral imagery and in situ spatial data. *Journal of Geophysical Research* **108**: 10.

Chrysoulakis N, Diamandakis M, Prastacos P. 2004. GIS based estimation and mapping of local level daily irradiation on inclined surfaces. In: Toppen F, Prastacos P (eds) *Proceedings of the 7th AGILE Conference on Geographic Information Science*, 587–597.

Dozier J, Bruno J, Downey P. 1981. A faster solution to the horizon problem. *Computers and Geosciences* **7**: 145–151.

Erbs DG, Klein SA, Duffie JA. 1982. Estimation of the diffuse radiation fraction for hourly, daily and monthly average global radiation. *Solar Energy* **28**: 293–304.

Frey C, Rigo G, Parlow E. 2007. Urban radiation balance of two coastal cities in a hot and dry environment. *International Journal of Remote Sensing* **28**: 2695–2712.

Hafner J, Kidder SQ. 1999. Urban heat island modeling in conjunction with satellite–derived surface/soil parameters. *Journal of Applied Meteorology* **38**: 448–465.

Halthore RN, Schwartz SE. 2000. Comparison of model-estimated and measured diffuse downward irradiance at surface in cloud-free skies. *Journal of Geophysical Research* **105**: 20165–20177.

Henzing JS, Knap WH, Stammes P, Apituley A, Bergwerff JB, Swart DPJ, Kos GPA, ten Brink HM. 2004. Effect of aerosols on the downward shortwave irradiances at the surface: Measurements versus calculations with MODTRAN4.1. *Journal of Geophysical Research*, **109**: 19.

Hofierka J, Šúri M. 2002. The solar radiation model for Open source GIS: implementation and applications. In: *Proceedings of the Open source GIS - GRASS users conference 2002 – Trento, Italy*: 11–13.

Iqbal M. 1983. An introduction to solar radiation. Academic Press, New York.

Kondo A, Ueno M, Kaga A, Yamaguchi K. 2001. The influence of urban canopy configuration on urban albedo. *Boundary-Layer Meteorology*, **100**: 225–242.

Liu BYH, Jordan RC. 1963. The long-term average performance of flatplate solar energy collectors. *Solar Energy* **7**: 53.

Maxwell EL. 1987. A quasi-physical model for converting hourly global horizontal to direct normal insolation. *SERI (Solar Energy Research Institute). Colorado*

NASA. 2007a. Jet Propulsion Laboratory, California Institute of Technology, ASTER Surface Reflectance/ Radiance VNIR/SWIR Product http://asterweb.jpl.nasa.gov/content/03_data/01_Data_Products/release_aster_surface_reflectance.htm Cited 15 June 2007

NASA. 2007b. Landsat 7 Science Data Users Handbook http://landsathandbook.gsfc.nasa.gov/handbook.html. Cited 15 Jun 2007

Parlow E. 1996. Correction of terrain controlled illumination effects in satellite data. In: Parlow, E (ed) *Progress in Environmental Research and Applications*, Balkema Publishers, Rotterdam: 139–145

Parlow E. 1998. Net radiation of urban areas. In: Gudmandsen, P. (ed) *Future trends in remote sensing*. Balkema Publishers, Rotterdam: 221–226.

Rigo G, Parlow E. 2007. Modelling the ground heat flux of an urban area using remote sensing data, *Theoretical and Applied Climatology* **90**, 185-199.

Rotach MW, Vogt R, Bernhofer C, Batchvarova E, Christen A, Clappier A, Feddersen B, Gryning S-E, Martucci G, Mayer H, Mitev V, Oke TR, Parlow E, Richner H, Roth M, Roulet YA, Ruffieux D, Salmond J, Schatzmann M, Voogt JA. 2005. BUBBLE-an urban boundary layer meteorology project. *Theoretical and Applied Climatology* **81**: 231–261.

Sailor DJ. 1995. Simulated urban response to modifications in surface albedo and vegetative cover. *Journal of Applied Meteorology* **34**: 1694–1704.

Sailor DJ, Fan H. 2002. Modeling the diurnal variability of effective albedo for cities. *Atmospheric Environment* **36**: 713–725.

Schläpfer D, Odermatt D. 2006. MODO User Manual, Version 3. Wil (SG), Switzerland.

Schwander H, Mayer B, Ruggaber A, Albold A, Seckmeyer G, Koepke P. 1999. Method to determine snow albedo values in the ultraviolet for radiative transfer modelling. *Applied Optics* **38**, 3869–3875.

Small C. 2005. A global analysis of urban reflectance. *International Journal of Remote Sensing* **26**: 661–681.

Soler MR, Ruiz C. 1994. Urban albedo derived from direct measurements and Landsat 4 TM satellite data. *International Journal of Climatology* **14**: 925–931.

Taha H. 1997. Urban climates and heat islands: albedo, evapotranspiration, and anthropogenic heat. *Energy and Buildings* **25**: 99–103.

3.2 Measurement of multispectral BRF effects of the megacity Cairo, Egypt using CHRIS/PROBA data

Corinne Frey, Eberhard Parlow

Published in the conference proceedings of 28th EARSeL Symposium and Workshops. Remote Sensing for a Changing Europe, 2-7 June, 2008, Istanbul / Turkey

ABSTRACT*: In this analysis, a series of images from the ESA imaging spectrometer CHRIS on the technology demonstration satellite PROBA, taken in a row over Cairo on 17 February 2007 and 24 March 2008 at each five different viewing zenith and azimuth angles are analyzed to find the BRF (bidirectional reflection function) which is typical for urban areas in a developing Arab country. The results are only valid for these sun-sensor constellations, since only two scenes were analyzed. CHRIS/PROBA features 18 bands in the shortwave range. All bands were first destriped and then corrected for atmospheric influences using the radiative transfer model MODTRAN. Furthermore the images were geo-referenced using manually set pass points. The accuracy of the geolocation varies across the image. Generally pixels match well; however, in some areas there is a shift of one or two pixels. There is a clear dependency in the reflectances on the viewing geometry of the sensor. The regression coefficients r^2 from the regression between the reflectance and the viewing geometry are high for all bands in all urban areas. No distinct difference was found for high or medium dense housing.*

3.2.1 Introduction

Urban surfaces differ from natural environments not only in their surface materials, but also in their diverse geometric forms, presented by blocks, houses, streets and open spaces. Measuring the reflected radiance of an urban area from space, the values of the resulting pixels are probably a mixture between variously illuminated surfaces and possible shading. Additionally, the albedo of roofs is mostly different from the albedo of walls. A side looking sensor is therefore measuring a different surface property than a nadir-viewing sensor. Considering pixel sizes in the mesoscale - like for example LANDSAT or ASTER data - these effects combine to an angular dependent reflection, referred to as 'bidirectional reflection distribution function' (BRDF). This function is not constant, but changes according to the sun zenith and azimuth angle. The BRDF effect was addressed for natural surfaces by many authors: Nicodemus (1970) described the bidirectional reflectance of diffusely scattering, homogenous surfaces. As the BRDF cannot be measured directly in practice (Schiefer et al. 2006), the bidirectional reflectance factor (BRF) is measured over finite solid angles.

Urban areas consist of a variety of materials and structures and don't fulfil the criterion to be homogeneous. A direct measurement of the urban BRF is only possible in the microscale and was done for selected surface materials by Meister et al. (1996, 1998). Schiefer et al. (2006) deducted BRF functions for four pure urban classes from 4 m resolution HyMap images of Berlin. They stress the difficulties with mixed pixels in the classification and their interference in the correction of the brightness gradient. On the macroscale it is assumed that for an urban class with similar characteristics in type of construction and vegetation ratio a large-scale BRF might converge. Meister et al. (1999) analyzed this topic using up scaled airborne data over the city of Nuremberg, Germany and deducted BRDFs for the city of Nuremberg.

In this study the total reflectance and the large-scale BRF effect of Cairo shall be examined to determine the influence of the sensor's view-angle and -direction and the illumination geometry to the urban reflectance.

3.2.2 Study area

The study area is located in Cairo, Egypt. Cairo is a strongly growing megacity, facing manifold problems like traffic congestion and air pollution (Robaa 2000). Housing in Cairo can be roughly divided into three classes. Firstly there are the very high density housing areas, where the spaces between the houses often just allow pedestrian walking. The houses are often of bad quality. Further there are other quarters which are built more spacious and belong to the richer parts of the population. Finally, there are huge areas of newly built houses in the outer quarters of Cairo, where the percentage of buildings in construction is high. In this study, only the first two classes will be considered.

3.2.3 Data

For this study, two scenes from the CHRIS (Compact High Resolution Imaging Spectrometer) instrument were used. CHRIS is a hyperspectral instrument on the technology demonstration satellite PROBA from ESA. Its objective is the collection of BRDF (Bidirectional Reflectance Distribution Function) data. PROBA was launched on 22 October 2001 from Sriharikota Island, India. It flies on an altitude between 570 and 670 km in a sun synchronous orbit. Its inclination is 97.9°. In Mode 1 (land) CHRIS features 18 bands between 400 and 1050 nm with a spatial resolution of 17 m at perigee. The swath width at nadir is 13 km. Main characteristic of the CHRIS data sets are the multi-angular acquisitions. The five targeted viewing angles are -55°, -36°, 0°, +36° and +55° (Cutter & Johns 2003, Guanter et al. 2005). Figure 45 shows the actual acquisition geometry of the two used scenes of 17 February 2007 and 24 March 2008 as extracted from the header information of the scenes.

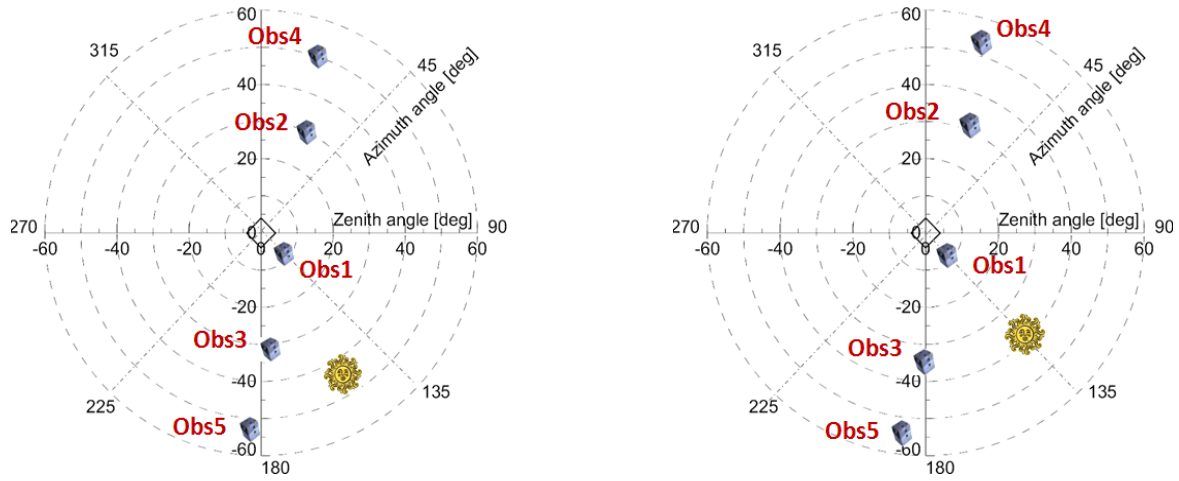

Figure 45 Actual acquisition geometry of the CHRIS/PROBA scenes. Left: February 17, 2007. Right: March 24, 2008

All data were provided from the European Space Agency. Unfortunately CHRIS data are affected by horizontal and vertical striping due to errors in the alignment of the sensors in the construction of the instrument and thermal fluctuations during the orbit (Garcia & Moreno 2004). ESA provides a software tool for the correction of these effects (HDFclean V2). However, a faint vertical stripping remains after the usage of the tool in most of the nadir-looking bands.

3.2.4 Methods

3.2.4.1 Atmospheric correction

Before analyzing the images, two correction steps were performed. Firstly, an atmospheric correction was performed on all bands using the radiative transfer model MODTRAN (MODerate resolution atmospheric TRANsmission (Berk et al. 1999)). As it is very difficult to obtain an exact estimation of the input atmosphere, the correction procedure was coupled with a statistical approach. Firstly, the path radiance and the transmissivity were estimated using radiosonde data from Helwan, which is south of Cairo, and the standard urban aerosol option as input atmosphere. The output was then convolved for each band width. The obtained path radiance and transmissivity were used to calculate the radiance at surface (L_{BOA}) according to formula (67) (Liang 2000).

$$L_{TOA}(\lambda) = L_P(\lambda) + \tau(\lambda) \cdot \rho(\lambda) \cdot L_{BOA}(\lambda) \quad (67)$$

L_{toa} = At-sensor radiance [$Wm^{-2}sr^{-1}\mu m^{-1}$]

L_p = Path radiance [$Wm^{-2}sr^{-1}\mu m^{-1}$]

L_{BOA} = Bottom of the atmosphere radiance [$Wm^{-2}sr^{-1}\mu m^{-1}$]

τ = Average atmospheric transmissivity

λ = Band width

The path radiance is almost linear dependent on the reflectance of the Earth surface; therefore a reflectance-dependent path radiance was used for the correction of the image. This term was estimated from a linear relation obtained from two MODTRAN runs with the albedo being 0.1 and 0.3. This linear relation was then applied to a slightly modified top-of-the-atmosphere reflectance.

Subsequently, the surface reflectance was calculated from the radiance at surface and the global irradiance, which was also convolved for each band, using formula (68) (Wang et al. 2000).

$$\rho(\lambda) = \frac{L_{BOA}(\lambda)}{L_G(\lambda)} \quad (68)$$

ρ = Reflectance

L_G = Global irradiance [$Wm^{-2}sr^{-1}\mu m^{-1}$]

Adjacency effects were corrected iteratively using formula 69 and 70 (Del Frate 2007):

$$\rho^{(2)}(\lambda,x,y) = \rho^{(1)}(\lambda,x,y) + \frac{L_{P(\lambda,x,y)}}{L_{G(\lambda,x,y)}}\left(\rho^{(1)}(\lambda,x,y)\right) - \bar{\rho}(\lambda,x,y) \quad (69)$$

$$\bar{\rho}(\lambda,x,y) = \frac{1}{n^2}\sum_{i,j=0}^{n}\rho_{i,j}^{(1)}(\lambda,x,y) \quad (70)$$

This procedure resulted in slightly too low reflectances. Therefore, the first guess of aerosol optical depth was itineratively reduced until only a small number of negative pixels were detected in the image. Figure 46 shows the spectral lines of three arbitrary chosen pixels of the scene of 17 February 2007 together with spectral lines from the ASTER JPL spectral library of similar land use (http://speclib.jpl.nasa.gov). The lines show a good agreement, considering, that only "similar" materials are compared. However, band 17 shows an overcorrection which might be due to radiometric calibration problems (Guanter et al. 2005). The scene of 24 March 2008 shows an analogue agreement, with exception of the vegetation curve that reaches only 30-40% reflectance in the near infrared. This lower reflection might be due to a different crop or a different growth phase of the crop.

3.2.4.2 Georeferencing

After the atmospheric correction, the images were georeferenced to the nadir viewing image with polynomial equations using ground control points. Table XIX shows the RMS (Root Mean Square) and the grade of the polynomials used. RMS is the distance of the georeferenced control point from the specified coordinate. While these RMS values correspond to the whole scene, only a subset of the scenes was used for the analysis. The agreement in the sub scene was even better.

3.2.4.3 Definition of land use classes

The analysis was done separately for five different land use classes: 'high density housing', 'low density housing', 'agricultural fields', 'Nile water' and 'desert'. The classification was done manual, including only 'known' areas.

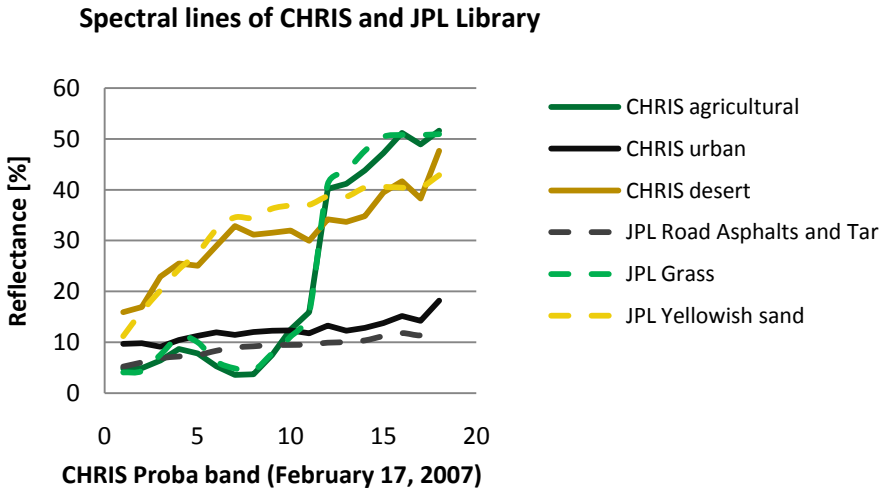

Figure 46 Spectral curves of three example pixels of the CHRIS scene of 17 February 2007 (nadir viewing)

Table XIX RMS values and grade of the polynomials used for the georeferencing

	February 17, 2007		March 24, 2008	
Observation	**RMS**	**Grade**	**RMS**	**Grade**
Obs 1	-	1	0.42	1
Obs 2	0.755	1	0.584	2
Obs 3	0.597	1	0.639	1
Obs 4	1.226	2	1.077	2
Obs 5	0.861	2	0.933	2

Even though the georeferencing showed a good agreement, it was not possible to do a pixel-to-pixel comparison. Therefore, the analysis was done using a running average of each pixel. The running average was calculated with a kernel of 9x9 pixels, whereas only pixels with a surrounding of at least 65 valid pixels were considered. For the class 'low density housing', this resulted in 126/126 valid values for both scenes. For the class 'high density housing' the numbers were 137/80. The class 'agricultural fields' showed only 9/9 values, the class 'Nile water' 20/8 values and the class 'desert' 14/4 values. The main purpose of this study was laid on the urban classes, the others were included only for comparison.

3.2.5 Results

A clear dependence of the reflectance on the viewing geometry of the sensor was found. Figure 47 shows the mean reflectances of three cuts from the classes 'high density housing' and 'medium density housing' of all bands for the different viewing geometries. Observations 3 and 5 have the highest values, which can be explained by their close angular position towards the sun ("hot spot" effect). Lowest values are found for observation 2 and 4, being opposite to the sun. This finding is consistent with Begiebing & Bach (2004). The nadir viewing observation (obs 1) shows similar values like observation 2 and 4.

The class 'Nile water' only shows a slight angular dependence in the first few bands; afterwards the reflectances conform to each other. Furthermore the water spectra are almost flat. This is in agreement with Gatebeck et al. (2005), who analyzed sea water BRDF and found only weak BRDF effects. In case of the agricultural class, the observations almost merge in the red bands. This is the region where the chlorophyll has its absorption maximum. Begiebing & Bach (2004) found a similar behaviour for maize. Figure 48 shows band 3 (531.2 nm) of all land use classes for the different viewing angles on February 17, 2007. The yellow arrow depicts the sun zenith angle. Here again it becomes clear that reflectances are highest, when the sun is "in the back" of the sensor.

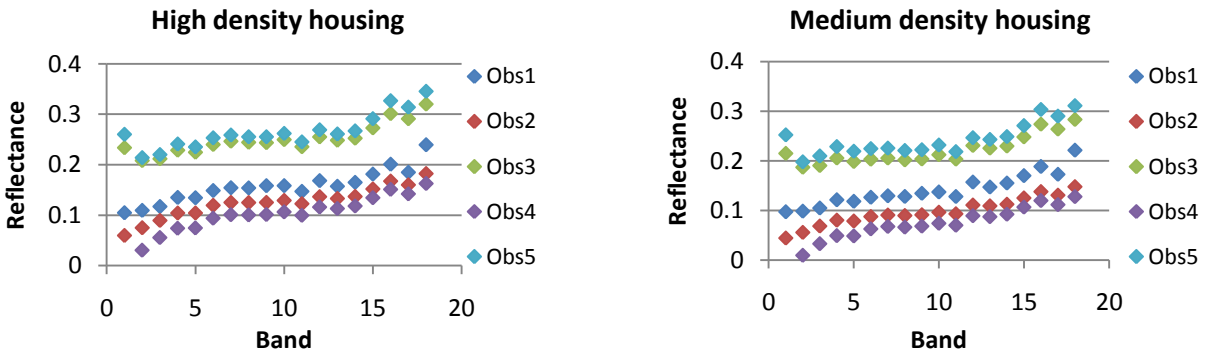

Figure 47 Angular reflectances of the scene of February 17, 2007

The running average reflectances, as explained in the last chapter, were compared to the zenith and azimuth angles of each acquisition and high correlations were found for both zenith and azimuth angles for both urban classes. The correlation coefficients r^2 range between 0.80 and 0.94 for the zenith angle and between 0.82 and 0.90 for the azimuth angle with the class 'high density housing' having slightly higher values than the class 'medium density housing'. The class 'desert' shows similar good correlations like the urban classes. As expected, the class 'Nile water' shows in all cases decreasing r^2 values with increasing wavelength. Also the class 'agricultural fields' fails to show good correlations on 24 March 2008, especially in the red bands, where the reflectances almost merge. Due to this merging of values, no slope can be detected and the regression must fail. In case of the scene of 17 February 2008 a good correlation is found for the class 'agricultural fields' for all bands. Figure 49 shows these correlations with the zenith angle. However, the results of the class 'desert', 'Nile water' and 'Agricultural fields' must be treated carefully, as the basic sets for these classes are not big enough to deduct robust statistic. Figure 49 shows the r^2 values for the zenith and azimuth angles for both scenes.

3.2.6 Discussion

In this analysis, the angular reflectances of two CHRIS Proba scenes were analyzed regarding their dependence on the sensor view geometry. After the necessary atmospheric correction and georeferencing, selected pixels of different land use classes ('high density housing', 'medium density housing', 'agricultural fields', 'desert' and 'Nile water') were compared and regressions with the sensor zenith and azimuth angle performed.

For both urban classes, high correlation coefficients were found. But surprisingly the difference between the two classes was negligible, even though the geometry of the houses differed notably. The class 'high density housing' showed a slightly higher correlation than the class 'medium density housing'. This might be due to the higher proportion of walls visible to the sensor. Walls are variously illuminated according to their exposition towards the sun. The desert class showed similar high correlation coefficients, whereas the classes 'agricultural fields' and 'water' showed weak correlations.

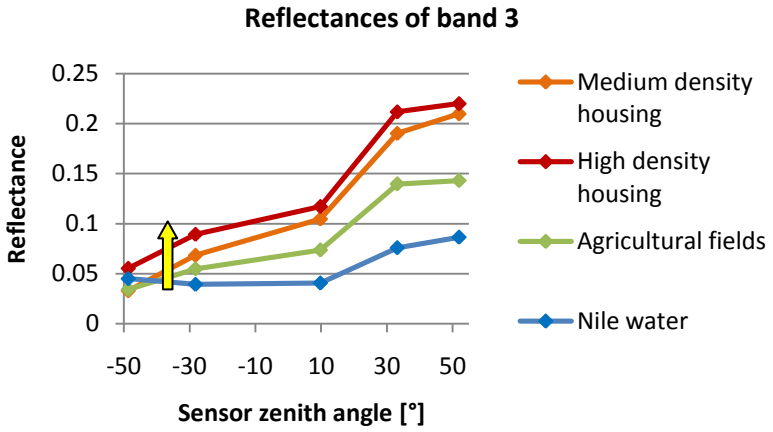

Figure 48 All land use classes for the different viewing angles on 17 February 2007 (band 3)

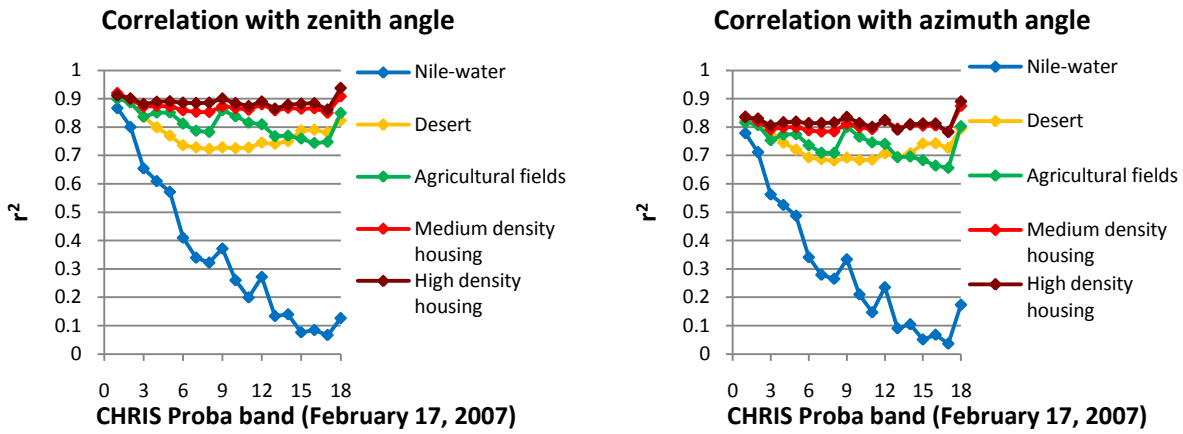

Figure 49 Correlation of surface reflectance with sensor zenith and sensor azimuth angle for the different land use classes.

Two limiting factors might limit partly the quality of the results. The first factor is the limited accuracy of the georeferencing process. Even though a running average was used, the results might be skewed slightly. The second factor applies only for the classes 'agricultural fields' and 'Nile water', where the basic set was not big enough to deduct a proper statistic.

3.2.7 References

Berk A, Anderson GP, Bernstein LS, Acharya PK, Doethe H, Matthew MW, Adler-Golden SM, Chetwynd JH, Richtsmeister SC, Pukall B, Allred CL, Jeong LS, Hoke LS. 1999. MODTRAN 4 radiative transfer modeling for atmospheric correction. *SPIE Proceeding, Optical Spectroscopic Techniques and Instrumentation for Atmospheric and Space Research III* **3756**: 6.

Cutter M, Johns L. 2005. CHRIS Data Products - Latest Issue. *Third CHRIS/Proba Workshop, ESRIN, Frascati, Italy*: 6.

Del Frate F, Duca R, Solimini D. 2007. Urban feature retrieved by hyperspectral multi-angle CHRIS Proba images. *2007 Urban Remote Sensing Joint Event, Paris, France*: 5.

Garcia JC, Moreno J. 2004. Removal of Noises in Chris/proba Images: Application to the Sparc Campaign Data. *Second Chris Proba Workshop, ESA-ESRIN, Frascati, Italy*: 5.

Gatebeck CK, King MD, Lyapustin A, Arnold GT, Redemann J. 2005. Airborne spectral measurements of ocean directional reflectance. *Journal of the atmospheric sciences* **62**: 1072–1092.

Guanter L, Alonso L, Moreno J. 2005. A method for the surface reflectance retrieval from PROBA/CHRIS data over land: application to ESA SPARC campaigns. *IEEE Transactions on Geoscience & Remote Sensing* **43**: 2908–2917.

Liang S. 2000. Narrowband to broadband conversions of land surface albedo I Algorithms. *Remote sensing of environment* **76**: 213–238.

Meister G, Lucht W, Rothkirch A, Spitzer H. 1999. Large Scale Multispectral BRDF of an Urban Area. *IEEE International Geoscience and Remote Sensing Symposium, IGARSS'99, Hamburg* **2**: 821– 823.

Meister G, Rothkirch A, Wiemker R, Bienlein J, Spitzer H. 1998. Modeling the directional reflectance (BRDF) of a corrugated roof and experimental verification. *IEEE International Geoscience and Remote Sensing Symposium, IGARSS'98, Seattle* **3**: 1487–1489.

Meister G, Wiemker R, Bienlein J, Spitzer H. 1996. In Situ BRDF Measurements of Selected Surface Materials to Improve Analysis of Remotely Sensed Multispectral Imagery. *Proceedings of the XVIII. Congress of the International Society for Photogrammetry and Remote Sensing ISPRS 1996, Vienna:* 493–498.

Nicodemus F. 1970. Reflectance nomenclature and directional reflectance and emissivity. *Applied Optics* **4**: 767–773.

Robaa SM. 2000. Giza monuments and local climate change. *ICEHM2000, 2000, Cairo University, Egypt*: 187–200.

Schiefer S, Damm A, Hostert P. 2006. Correcting brightness gradients in hyperspectral data from urban areas. *Remote Sensing of Environment* **101**: 25–37.

Wang J, White K, Robinson GJ. 2000. Estimating surface net solar radiation by use of Landsat-5 TM and digital elevation models. *International Journal of Remote Sensing* **21**: 31–43.

4 Summary and conclusions

4.1 Flux measurements in Cairo

The aim of this thesis was to estimate the surface energy budget of a remote city with highly contrasting surface features using satellite data, and determine the possibilities and constraints of such a remote sensing approach. Data from the high resolution radiometer ASTER on the sun-synchronous satellite TERRA were used in combination with other optical satellite data (MISR) and radar data as well (SRTM, ASAR). After a sophisticated atmospheric correction with MODTRAN and the estimation of the radiation budget, different approaches were used to determine the soil and turbulent heat fluxes for the times of over flights. The results of these calculations were compared to in situ measurements of three ground stations in Greater Cairo that were operated parallel to the acquisition window of ASTER from November 2007 to February 2008 (CAPAC field campaign). All components of the energy balance were measured along with wind direction and speed, air and soil temperatures and sampled as 30 minute, and one minute averages respectively. Additional to this work a study on the determination of the aerodynamic resistance to heat in an urban area using morphometric methods was done, supplementing the surface flux research using satellite images.

Further, two remote sensing studies on the determination of surface reflectance were conducted. Surface reflectance is probably the most important term in the radiation balance and was therefore thoroughly analyzed. The first study was dealing with the geometry effect on the albedo in urban areas; the second study analyzed directional effects over urban Cairo.

Besides the work on the surface energy balance, an additional study dealing with CO_2 fluxes and concentrations at an urban location was presented. The study used in situ data which were also taken in Cairo during the CAPAC field campaign. The study was conducted by Susanne Burri, a master student of the University of Basel. The resulting paper is included in this thesis to cover all aspects of CAPAC.

The analysis of the in situ measurements showed that the three stations differed in many measured variables. Due to diverse surface covers, high variations in roughness, surface albedo and soil moisture occurred. Even the incoming irradiation varied due to spatially changing levels of air pollution. All these contrasts led to different radiation budgets, soil and turbulent heat fluxes.

The solar irradiation showed highest values at the desert station, which was about 50 km away from central Cairo. This spoke for a less contaminated atmosphere outside the city. The agricultural station, at the rim of the suburban Cairo showed lower values. Lowest values however were found at the urban station, where the urban smog plume was probably most distinctive. This finding had a consequence on the atmospheric correction of the satellite images, where the absorbing and scattering effect of aerosols had to be considered. Assuming that the aerosol load and composition was not spatially homogeneous over the area, correction parameters had to be defined for each pixel separately.

It was found further that Cairo features a nocturnal urban heat island (UHI), with typically higher air and radiative surface temperatures in the city than in the surrounding stations. These nocturnal differences disappeared when south to southwest wind situations occurred. Probably the UHI was shifted to north. The UHI was much stronger, when radiative temperatures were used instead of air temperatures. The generally accepted finding, that urban areas better store heat than the rural surroundings was affirmed also in this study, even in the case of the dry, sandy desert surroundings.

The net radiation of the suburban-agricultural station was highest, while the suburban-desert station had the lowest values. This finding was caused by high differences found in the surface albedo. Mean surface albedo at the urban station was 0.21, at the suburban-agricultural station 0.15 and at the suburban-desert

station 0.33. The surface albedo showed a slight diurnal pattern due to the measurement setup. Besides this common known feature, surface albedo changed also over the campaign time. While some features could be explained by rain and irrigation, a general dropping over the 3 month period could not be explained finally. As the surface albedo is the most prominent term in the net radiation, this finding suggests, that surface albedo should be regularly updated, when modelling the net radiation with or also without use of remote sensing data.

The measured soil heat flux consisted of two terms: the soil heat flux at depth z and the heat storage above z. Latter was found to be a major contributor, showing extreme short-term fluctuations owing to rapid radiative surface temperature changes. Such changes cannot be observed by a remote sensing image and a soil heat flux retrieved from space can only represent some averaged flux as was shown in the successive remote sensing study.

In turn, the in situ measured turbulent heat fluxes are time-averages (here 30 minutes), which again cannot be observed by remote sensing approaches using an instant multispectral scene. As the in situ data are normally used for the calibration of the remote sensing methods, the remote sensing approach will always keep an error-level due to the different temporal resolution.

While at the urban and the suburban-desert station most of the available energy was going into the sensible heat flux, the latent heat flux dominated at the suburban-agricultural station. The Bowen ratio had a high daytime temporal variation, which suggests that a Bowen ratio method for the determination of turbulent fluxes from remote sensing images is only useful when calculating daily, weekly or even monthly means. The turbulent heat fluxes showed certain directionality, especially at the suburban-agricultural station. This directionality promotes the definition of source areas for the comparison with remote sensing data. When determining the energy balance with state of the art eddy covariance technique, the sum of the heat fluxes does not equal the net radiation, i.e. sometimes a considerable residual remains, as it did in the CAPAC campaign. The magnitude of this residual was too high to be ignored and had therefore to be redistributed on the other terms. Due to the uncertainty of this redistribution, an exact determination of heat fluxes is difficult and any comparison with such data must consider this fact.

As supposed from the findings of the field campaign, the atmospheric correction proved to be crucial for a successful estimation of the radiation and energy balance from the ASTER satellite images. A ‘best guess’ scenario estimated the albedo with 15.4% accuracy only, averaging all comparison points, while the ‘best fit’ scenario improved it to 9.8 %. Especially the estimation of the shortwave irradiance and irradiation was strongly influenced by varying levels of aerosol optical depth in the image. The longwave terms did not show such a high dependency on the atmospheric correction. The net radiation was estimated with 11.6% accuracy in the ‘best guess’ case and with 6.9 % in the ‘best fit’ case. These results are considered to be good and fit into the accuracy of the in situ instrument. However, in single cases the accuracy was less.

The soil heat flux was modelled as a product mainly from the net radiation and vegetation indices. Three approaches gave satisfactory results, when comparing the values to 30 minute averages of in situ measured data.

Using the LUMPS approach, the turbulent heat fluxes were calculated using different methodological combinations, including the two above mentioned scenarios of atmospheric correction, the different methods for the soil heat flux, and LUMPS parameter from literature or empirically retrieved from the field campaign data. All in all 17 possible combinations were used. The comparison with the in situ measured data included further three footprint models. Overall *MAD* of the sensible heat flux of the urban station was 40 Wm^{-2} which is 21% of the mean in situ measured flux. At the agricultural station the overall *MAD* was 33 Wm^{-2} (28%) and at the desert station it was 21 Wm^{-2} (14%). The respective values for the latent heat flux

were 28 Wm^{-2} (58%), 65 Wm^{-2} (35%) and 16 Wm^{-2} (63%). The degree of homogeneousness seemed to influence the quality of the products, resulting in the desert station to show the best absolute agreement. But considering the relative high uncertainty of the in situ measurements themselves the general agreement of the satellite products and the in situ measurements is acceptable.

The 'best fit' option performed better than the 'best guess' scenario which is easily explained by the nature of the calculation approach of the 'best fit' option. The influence of the different methods for the soil heat flux was not clearly visible in the data, as probably other factors produced errors higher than their influence was. However, spatial analysis revealed that most reasonable results were given by the 'Parlow/urban' method or the two new approaches. Generally the literature parameters showed lower agreement than the empirically retrieved ones, while the spatial analysis showed, that only the 'sectoral' approach was able to reproduce expected spatial pattern. The latent heat flux was modelled better than the sensible heat flux in both empirical cases, which might be due to the fact, that the empirical parameters were retrieved from the formula for the latent heat flux. The application of the footprint models finally did not improve the agreement in most cases and is therefore not encouraged when comparing measurements with high uncertainty. Even though the LUMPS approach is promising, more research must be undertaken to determine accurate parameters, depending for example on the vegetation density, soil moisture and roughness.

The ARM approach was not calculated with all possible soil heat fluxes, but only with the 'Parlow/urban' method and the in situ measured values. But the two cases of atmospheric correction were applied and also there were two versions of spatial air temperatures. Overall *MAD* of the sensible heat flux of the urban station was 49 Wm^{-2} which is 26% of the mean in situ measured flux. At the agricultural station the overall *MAD* was 10 Wm^{-2} (8.6%) and at the desert station it was 52 Wm^{-2} (33%). The respective values for the latent heat flux were 45 Wm^{-2} (93%), 46 Wm^{-2} (25%) and 49 Wm^{-2} (215%). Naturally, the 'best fit' option performed better than the 'best' guess' option and the application of the footprint model worsened the agreement. However, the spatial pattern of the ARM approach was realistic and probably better than the pattern produced by the LUMPS approach. The estimation of air temperature using the formula of Xu et al. (2008) however, lead to unrealistic spatial pattern.

The S-SEBI approach proved to be not suitable in the study area due to a detected high range of surface temperatures in the desert areas. Therefore this approach was not pursued further and no comparison was done with in situ measured values.

The analysis of CO_2 fluxes and concentrations revealed that despite of its high traffic density and its considerable share of old cars and other CO_2 emitters measured values were not as high as expected. The distance of the measurement instruments to the main CO_2 sources might explain this result. Average peak values of the CO_2 flux were around 15 $\mu molm^{-2}s^{-1}$ and average peak concentrations in the morning were around 420 ppm. The CO_2 concentrations showed an average diurnal course with the maximum in the early morning as a result of the nocturnal stable boundary layer. The average diurnal course of CO_2 fluxes showed a single maximum peak between 1 and 3 pm, which is different from most previous studies, where often two rush-our peaks were observed. However, the single maximum peak fits to the observation of the main author of increasing traffic density until the afternoon. The influence of the traffic became evident on Fridays (Sabbath in Cairo), when the fluxes were considerably lower compared to the other weekdays. The investigation of different urban surfaces showed, that the vegetated area close to the measurement tower was able to reduce the CO_2 fluxes. Possible negative fluxes induced by photosynthesis, however, were superimposed by the overall CO_2 source of the city, and the CO_2 fluxes resulted therefore positive on

average. Regarding the CO_2 concentrations, the morning peak and the daily concentrations were considerably lower over the vegetated area.

Getting back to the ARM approach for calculating the sensible heat flux, an alternative way of determining the aerodynamic resistance for heat was investigated in a separate study. While in the main study the aerodynamic resistance was estimated from radar data, it was retrieved in this study from a digital surface model using morphometric methods. It was found, that the aerodynamic resistance can be modelled satisfactorily when using an empirical factor of -0.7 to -0.8 for α which is used for the calculation of the roughness length of heat. Three different morphometric methods for the calculation of the roughness length were compared (MA, BO and RA). While BO and RA delivered similar spatial aerodynamic resistances, the MA method yielded lower values in very dense areas. All three methods worked only, when a minimum roughness length of at least 0.02 was given. This study showed, that it is possible to determine satisfactorily the aerodynamic resistance over an urban area. Precondition is, however, the availability of a digital surface model, which limits the approach mostly to cities in developed countries to date.

4.2 Estimation of band reflectance using data from remote sensors

Two separate studies shed light on various aspects of the measurement of the urban albedo. In the first study, it was analyzed what impact the urban roughness imposes on the irradiance and the surface albedo, using a digital surface model of the city of Basel and radiative transfer modelling. It was shown, that the omission of a surface model induces a considerable error in the determination of the two terms, mainly due to shadow effects. The error found was in the range of 0.015 to 0.079 for a densely built-up urban area, calculated for the hours 11:00 to 14:00, for all days of the year and for four different atmospheric models and 1 m pixel resolution. The error was not only dependent on the sun altitude, but also on the compactness of the urban elements. In densely-built quarters the error was higher than in less dense areas. Further the composition of the atmosphere influences the accuracy. In highly contaminated atmospheres, the percentage of diffuse irradiance is high, leading to lower contrasts between shaded and sunlit pixels and therefore to a lesser impact of the casted shadows. It was further shown, that the error decreased when increasing the pixel size. With a 100 m pixel resolution, the above mentioned error would range from 0.004 to 0.042 only. The geometry effect certainly played a role in the determination of the urban surface albedo estimated from the ASTER data. However, due to the high level of air pollution the effect must have been minimized for the given sun altitude and housing density. A maximum error of 0.02 is estimated for the urban station. Also the in situ measurement is composed of a mixture of differently illuminated surfaces, but the weighting of the single surfaces is different due to different pixel sizes and viewing angles. The comparison of remote sensing pixels with in situ measurements is certainly biased, but probably will be less than 0.02.

Besides this geometry effect remotely sensed surface reflectances are subject to a dependency on the acquisition angle (BRDF effect). To show this effect for Cairo, two CHRIS Proba scenes were analyzed to show differences in the urban reflectance of different viewing angles. Surface reflectances from scenes with an angular position close to the sun had the highest values (“hot spot” effect). Scenes that were taken opposite the sun direction were lowest. The highest difference of two such extreme observations for the mean reflectances of all bands is 0.17 for the urban test cases. The almost nadir viewing observation had medium reflectances in comparison with all scenes. This effect was found for all bands of CHRIS Proba, but to be almost independent on the housing density. The mean reflectance of all observations was higher than the almost nadir viewing observation. The difference of the mean reflectance of all observations and the reflectance of the almost nadir viewing observation is 0.01 and 0.02 for the urban test cases. As the ASTER

satellite is acquiring almost nadir-viewing, it is supposed that the resulting albedo is slightly underestimated. The albedo is used for the estimation of the net radiation, determining the part of the irradiation which is reflected back to space. Thereby mainly the direction of the incoming irradiation is important, where the reflectance was shown to be higher than that of the nadir-viewing observation. The difference between the almost nadir-viewing reflectance and those sensed with zenith and azimuth angles close to the sun's angles was 0.09. This relatively high number would imply, that the reflected radiation in the ASTER analysis was underestimated and consequently net radiation overestimated. In fact the urban net radiation was overestimated in the 'best guess' case in two of three cases. However, the study on the geometry effect has shown, that this effect is highly dependent on the percentage of diffuse radiation. Therefore it is difficult to give a correct estimate of the overestimation in net radiation for the used ASTER scenes.

4.3 Concluding remarks

The work on the energy balance in Cairo, Egypt has shown many interesting aspects of a megacity in a heterogeneous landscape. While the in situ measurements provided insight in three respective microclimates, the remote sensing approach examined spatial aspects. The heterogeneity of the landscape proved to be the major challenge for the used approaches and indicated the thematic areas, where more research is needed. Amongst these areas is the spatial distribution of atmospheric parameters for a better atmospheric correction, more accurate ways of determining the LUMPS parameter and the provision of digital surface models in developing countries for better estimates of urban albedo and aerodynamic resistance using morphometric methods.

5 Cited and additional useful references

Abrams M. 2000 The Advanced Spaceborne Thermal Emission and Reflection Radiometer (ASTER): Data Products for the High Spatial Resolution Imager on NASA's Terra Platform. *International Journal of Remote Sensing* **21**: 847–859.

Abu–Allaban M, Gertler AW, Lowenthal DH. 2002. A preliminary apportionment of the sources of ambient PM10, PM2.5 and VOCs in Cairo. *Atmospheric Environment* **36**: 5549–5557.

Abu–Hamdeh NH, Reeder RC. 2000. Soil thermal conductivity. Effects of density, moisture, salt concentration, and organic matter. *Soil Science Society of America Journal* **64**: 1285–1290.

Aida M, Gotoh M. 1982. Urban albedo as a function of the urban structure – A two–dimensional numerical simulation. *Boundary–Layer Meteorology*, **23**: 416–424.

Aida M. 1982 Urban albedo as a function of the urban structure – A model experiment. *Boundary–Layer Meteorology*, **23**: 405–413.

Baker LA, Brazel AJ, Selover N, Martin C, McIntyre N, Steiner FR, Nelson A, Musacchio L. 2002. Urbanisation and warming of Phoenix (Arizona, USA): Impacts, feedbacks and mitigation. *Urban Ecosystems* **6**: 183–203.

Barradas VL, Tejeda–Martínez A, Jáuregui E. 1999. Energy balance measurements in a suburban vegetated area in Mexico City. *Atmospheric Environment* **33**: 4109–4113.

Bastiaanssen WGM, Menenti M, Feddes RA, Holtslag AAM. 1998. A remote sensing surface energy balance algorithm for land (SEBAL). 1. Formulation. *Journal of Hydrology* **212–213**: 198–212.

Bastiaanssen WGM, Noordman EJM, Pelgrum H, Davids G, Thoreson BT, Allen RG. 2005. SEBAL Model with Remotely Sensed Data to Improve Water-Resources Management under Actual Field Conditions. *Journal of Irrigation and Drainage Engineering* **131(1)**: 85–93.

Berk A, Anderson GP, Bernstein LS, Acharya PK, Doethe H, Matthew M.W, Adler-Golden SM, Chetwynd JH, Richtsmeister SC, Pukall B, Allred CL, Jeong LS, Hoke ML. 1999. MODTRAN 4 radiative transfer modeling for atmospheric correction. *Proceeding, Optical Spectroscopic Techniques and Instrumentation for Atmospheric and Space Research III* **3756**, Denver CO, July 1999, SPIE, Bellingham, WA, USA: 6.

Blumberg DG, Greeley R. 1993. Field studies of aerodynamic roughness length. *Journal of Arid Environments* **25**: 39–48.

Bottema M. 1997. Urban roughness modelling in relation to pollutant dispersion. *Atmospheric Environment* **31**: 3059-3075.

Brest CL. 1987 Seasonal albedo of an urban/rural landscape from satellite observations. *Journal of Applied Meteorology*, **26**: 1169–187.

Brutsaert W. 1982. Evaporation into the Atmosphere. Theory, History and Applications. Kluwer Academic Publishers, Dordrecht: 264.

Burian SJ, Michael JB, Linger SP. 2002. Morphological analyses using 3D building databases: Los Angeles, California. *Los Alamos National Laboratory*: 74.

Carlson TN, Ripley DA. 1997. On the relation between NDVI, fractional vegetation cover and leaf area index. *Remote Sensing and Environment* **62**:241–252.

Chehbouni A, Seen DL, Njoku EG, Lhomme J-P, Monteny B, Kerr YH. 1997. Estimation of sensible heat flux over sparsely vegetated surfaces. *Journal of Hydrology* **188–189**: 855–868.

Chehbouni G, Nouvellon Y, Lhomme JP, Watts C, Boulet G, Kerr YH, Moran MS, Goodrich DC. 2001. Estimation of surface sensible heat flux using dual angle observations of radiative surface temperature. *Agriculture and Forest Meteorology* **108**: 55–65.

Chen B, Black TA, Coops NC, Hilker T, Trofymow JAT, Morgenstern K. 2009. Assessing tower flux footprint climatology and scaling between remotely sensed and eddy covariance measurements. *Boundary-Layer Meteorology* **130**: 137–167.

Choudhury BJ, Idso SB, Reginato RJ. 1987. Analysis of an empirical model for soil heat flux under a growing wheat crop for estimating evaporation by an infrared-temperature based energy balance equation. *Agricultural and Forest Meteorology* **39**: 283–297.

Chow WTL, Roth M. 2006. Temporal dynamics of the urban heat island of Singapore. *International Journal of Climatology* **26**: 2243–2260.

Christen A, Vogt R. 2004. Energy and radiation balance of a central European city. *International Journal of Climatology* **24**: 1395–1421.

Chrysoulakis N, Diamandakis M, Prastacos P. 2004. GIS based estimation and mapping of local level daily irradiation on inclined surfaces. In: Toppen F, Prastacos P (eds) *Proceedings of the 7th AGILE Conference on Geographic Information Science*, 587–597.

Chrysoulakis N. 2003. Estimation of the all-wave urban surface radiation balance by use of ASTER multispectral imagery and in situ spatial data. *Journal of Geophysical Research*, **108**: 10.

Churkina G. 2008. Modeling the carbon cycle of urban systems. *Ecological Modelling* **216**: 107-113.

Coutts AM, Beringer J, Tapper NJ. 2007. Characteristics influencing the variability of urban CO_2 fluxes in Melbourne, Australia. *Atmospheric Environment* **41**: 51-62.

Cutter M, Johns L. 2005. CHRIS Data Products - Latest Issue. *Third CHRIS/Proba Workshop 21–23 March, ESRIN, Frascati, Italy*, 6.

Dash P, Göttsche F-M, Olesen F-S, Fischer H. 2002. Land surface temperature and emissivity estimation from passive sensor data: theory and practice - current trends. *International Journal of Remote Sensing* **23**: 2563–2594.

de Bruin HAR, Holtslag AAM. 1982: A simple parameterization of surface fluxes of sensible and latent heat during daytime compared with the Penman-Monteith concept. *Journal of Applied Meteorology* **21**: 1610–1621.

De Ridder K, Mensink C. 2003. Surface fluxes and atmospheric stability obtained from a surface energy balance model with parameters estimated from satellite remote sensing. *International Journal of Environment and Pollution* **19(1)**: 22–31.

Del Frate F, Duca R, Solimini D. 2007. Urban feature retrieved by hyperspectral multi-angle CHRIS Proba images. *2007 Urban Remote Sensing Joint Event, 11–13 April 2007, Paris, France*, 5.

Denman KL, Brasseur G, Chidthaisong P, Ciais P, Cox PM, Dickinson RE, Hauglustaine C, Heinze C, Holland E, Jacob D, Lohmann U, Ramachandran S, da Silva Dias PL, Wofsy SC, Zhang X. 2007. Couplings Between Changes in the Climate System and Biogeochemistry. In: *Climate Change 2007: The Physical Science Basis. Contribution of Working Group I to the Fourth Assessment Report of the Intergovernmental Panel on Climate Change* [Solomon S, Qin D, Manning M, Chen Z, Marquis M, Averyt KB, Tignor M, Miller HL (eds.)]. Cambridge University Press, Cambridge, United Kingdom and New York, NY, USA.

Diner DJ, Martonchick JV, Kahn RA, Pinty B, Gobron N, Nelson DL, Holben BN. 2005. Using angular and spectral shape similarity constraints to improve MISR aerosol and surface retrievals over land. *Remote Sensing of Environment* **94**: 155–171.

Dozier J, Bruno J, Downey P. 1981. A faster solution to the horizon problem. *Computers and Geosciences* **7**: 145–151.

El-Khattib HM, El-Mowelhi NM, Hawela F. 1996. Monitoring land cover of the desert fringes of the eastern Nile Delta, Egypt. *Geoscience and Remote Sensing Symposium, 1996 (IGARSS '96). Remote Sensing for a Sustainable Future* **3**: 1756–1758.

El-Metwally M. 2004. Simple new methods to estimate global solar radiation based on meteorological data in Egypt. *Atmospheric Research* **69**: 217–239.

El-Sebaii AA, Trabea AA. 2003. Estimation of horizontal diffuse solar radiation in Egypt. *Energy Conversion and Management* **44**: 2471–2482.

El-Sebaii AA, Trabea AA. 2005. Estimation of global solar radiation on horizontal surfaces over Egypt. *Egyptian Journal of Solids* **28**: 163–175.

Erbs DG, Klein SA, Duffie JA. 1982. Estimation of the diffuse radiation fraction for hourly, daily and monthly average global radiation. *Solar Energy* **28**: 293-304.

Fahmi W, Sutton K. 2007. Greater Cairo's housing crisis: contested spaces from inner city areas to new communities. *Cities* **25**: 277–297.

Favez O, Cachier H, Sciare J, Alfaro SC, El-Araby TM, Harhash MA, Abdelwahab MM. 2008. Seasonality of major aerosol species and their transformations in Cairo megacity. *Atmospheric Environment* **42**: 1502–1516.

Feigenwinter C, Bernhofer C, Eichelmann U, Heinesch B, Her tel M, Janous D, Kolle O, Lagergren F, Lindroth A, Minerbi S, Moderow U, Mölder M, Montagnani L, Queck R, Rebmann C, Vestin P, Yernaux M, Zeri M, Ziegler W, Aubinet M. 2008. Comparison of horizontal and vertical advective CO_2 fluxes at three forest sites. *Agricultural and Forest Meteorology* **148**: 12–24.

Foken T. 2008. The energy balance closure problem: an overview. *Ecological Applications* **18**: 1351–1367.

French AN, Jacob F, Anderson MC, Kustas WP, Timmermans W, Gieske A, Su Z, McCabe MF, Li F, Prueger J, Brunsell N. 2005. Surface energy fluxes with the advanced spaceborne thermal emission and reflection radiometer (ASTER) at the Iowa 2002 SMACEX site (USA). *Remote Sensing of Environment* **99**: 55–65.

Frey C, Rigo G, Parlow E. 2007. Urban radiation balance of two coastal cities in a hot and dry environment. *International Journal of Remote Sensing* **28**: 2695–2712.

Frey CM, Parlow E, Vogt R, Abdel Wahab M, Harhash M. 2010. Flux measurements in Cairo. Part 1: In situ measurements and their applicability for comparison with satellite data. *International Journal of Climatology*. Accepted.

Frey CM, Parlow E. 2009. Geometry effect on the estimation of band reflectance in an urban area. *Theoretical and Applied Climatology* **96**: 395–406.

Frey CM, Parlow E. Flux measurements in Cairo. Part 2: On the determination of the spatial radiation and energy balance using ASTER satellite data. *International Journal of Climatology*. Submitted.

Gaffin SR, Rosenzweig C, Khanbilvardi R, Parshall L, Mahani S, Glickman H, Goldberg R, Blake R, Slosberg RB, Hillel D. 2008. Variations in New York city's urban heat island strength over time and space. *Theoretical and Applied Climatology* **94**: 1–11.

Gál T, Sümeghy Z. 2007. Mapping the roughness parameters in a large urban area for urban climate applications. *Acta Climatologica et Chorologica. Universitatis Szegediensis, Tomus* **40-41**: 27-36.

Garcia, J.C., Moreno, J. 2004. Removal of Noises in Chris/proba Images: Application to the Sparc Campaign Data. *Second Chris Proba Workshop, 28–30 April 2004, ESA-ESRIN, Frascati, Italy*, 5.

Garcia-Cueto OR, Jauregui-Ostos E, Toudert D, Tejeda-Martinez A. 2007. Detection of the urban heat island in Mexicali, B.C., Mexico and its relationship with land use. *Atmosfera* **20**: 111–131.

Garcia-Moreno TF, Fargant G, Guerin F, Israbian C, Mathieu JC, Michaud J, Bardoux A, Hagolle O, Lagouarde JP. 2009. MISTIGRI instrumental concept for high-resolution thermal infrared imaging. Infrared Spaceborne Remote Sensing and Instrumentation XVII. Eds: Garcia-Moreno TF, Fargant G, Guerin F, Israbian C, Mathieu JC, Michaud J, Bardoux A, Hagolle O, Lagouarde JP. *Proceedings of the SPIE* **7453**: 745307-745307-12.

Gatebeck, C.K., King, M.D., Lyapustin, A., Arnold, G.T., Redemann, J. 2005. Airborne spectral measurements of ocean directional reflectance. *Journal of the atmospheric sciences* **62**: 1072–1092.

Gillespie A, Rokugawa S, Matsunaga T, Cothern JS, Hook S, Kahle AB. 1998: A Temperature and Emissivity Separation Algorithm for Advanced Spaceborne Thermal Emission and Reflection Radiometer (ASTER) Images. *IEEE Transactions on Geoscience and Remote Sensing* **36**: 1113–1126.

Goossens R, Tack FMR, Devriendt D, Ateya O, Parlow E. DEM-generation from SPOT 5 across-track imagery. A case study over CAIRO and surroundings. 28th EARSeL Symposium: Remote Sensing for a Changing Europe. Istanbul, Turkey, 2. June - 5. June 2008

Gowda PH, Chávez JL, Colaizzi PD, Evett SR, Howell TA, Tolk JA. 2007. Remote sensing based energy balance algorithms for mapping ET: current status and future challenges, *Transactions of the ASABE* **50(5)**: 1639–1644.

Greeley R, Blumberg DG, McHone JF, Dobrovolskis A, Iversen JD, Lancaster N, Rasmussen KR, Wall SD, White BR. 1997. Applications of spaceborne radar laboratory data to the study of aeolian processes. *Journal of Geophysical Research* **102(E5)**: 10,971–10,983.

Grimmond CSB, King TS, Cropley FD, Nowak DJ, Souch C. 2002. Local-scale fluxes of carbon dioxide in urban environments: methodological challenges and results from Chicago. *Environmental Pollution* **116**: 243-254.

Grimmond CSB, Oke TR 2002. Turbulent heat fluxes in urban areas: observations and a local-scale urban meteorological parameterization scheme (LUMPS). *Journal of Applied Meteorology* **41**: 792–810.

Grimmond CSB, Oke TR, Cleugh HA. 1993. "The role of "rural" in comparisons of observed suburban-rural flux differences", *International Association of Scientific Hydrology* **212**: 165–174.

Grimmond CSB, Oke TR. 1995. Comparison of heat fluxes from summertime observations in the suburbs of four North American cities. *Journal of Applied Meteorology* **34**: 873–889.

Grimmond CSB, Oke TR. 1999. Aerodynamic properties of urban areas derived from analysis of surface form. *Journal of Applied Meteorology* **38:** 1262-1292.

Grimmond CSB, Oke TR. 2002. Turbulent heat fluxes in urban areas: Observations and a local-scale urban meteorological parameterization scheme (LUMPS). *Journal of Applied Meteorology and Climatology* **41(7)**: 792–810.

Grimmond CSB, Salmond JA, Oke TR, Offerle B, Lemonsu A. 2004. Flux and turbulence measurements at a densely built-up site in Marseille: Heat, mass (water and carbon dioxide), and momentum. *Journal of Geophysical Research* **109**: D24101 1-19.

Guanter L, Alonso L, Moreno, J. 2005. A method for the surface reflectance retrieval from PROBA/CHRIS data over land: application to ESA SPARC campaigns. *IEEE Transactions on Geoscience, Remote Sensing* **43**: 2908–2917.

Hafner J, Kidder SQ. 1999. Urban heat island modeling in conjunction with satellite-derived surface/soil parameters. *Journal of Applied Meteorology* **38**: 448–465.

Halthore RN, Schwartz SE. 2000 Comparison of model-estimated and measured diffuse downward irradiance at surface in cloud-free skies. *Journal of Geophysical Research* **105**: 20165–20177.

Harhash M. 2009. Origin and characteristics of some dust events in Cairo using Sigma-2 passive samplers. *Master thesis*. Cairo University, Egypt: 99.

Hasanean HM, Abdel Basset H. 2006. Variability of summer temperature over Egypt. *International Journal of Climatology* **26**: 1619–1634.

Hasanean HM. 2004. Wintertime surface temperature in Egypt in relation to the associated atmospheric circulation. *International Journal of Climatology* **24**: 985–999.

Henzing JS, Knap WH, Stammes P, Apituley A, Bergwerff JB, Swart DPJ, Kos GPA, ten Brink HM. 2004. Effect of aerosols on the downward shortwave irradiances at the surface: Measurements versus calculations with MODTRAN4.1. *Journal of Geophysical Research*, **109**: 19.

Hofierka J, Šúri M. 2002. The solar radiation model for Open source GIS: implementation and applications. *Proceedings of the Open source GIS - GRASS users conference 2002 - Trento, Italy*: 11–13.

Holtslag AAM, AP van Ulden. 1983. A simple scheme for daytime estimates of the surface fluxes from routine weather data. *Journal of Climate and Applied Meteorol*ogy **22**: 517–529.

Hsieh CI, Katul G, Chi T. 2000. An approximate analytical model for footprint estimation of scalar fluxes in thermally stratified atmospheric flows. *Advances in Water Resources* **23**: 765-772.

Hsu NC, Tsay S-C, King MD, Herman JR. 2004. Aerosol properties over bright-reflecting source regions. *IEEE Transactions on Geoscience and Remote Sensing* **42**: 557–569.

Hung T, Uchihama D, Ochi S, Yasuoka Y. 2006. Assessment with satellite data of the urban heat island effects in Asian mega cities. *International Journal of Applied Earth Observation and Geoinformation* **8**: 34–48.

Ibrahim FN, Ibrahim B. 2006. *Ägypten*. Wissenschaftliche Buchgesellschaft (WBG): Darmstadt.

Ioannilli M, Rocchi E. 2008. Urban Roughness Parameters Calculation in the City of Rome by Applying Analytical and Simplified Formulations: Comparison of Results. *Lecture Notes in Computer Science* **5072**: 284-299.

Iqbal M. 1983. An introduction to solar radiation. Academic Press, New York

Jeyachandran I, Burian SJ, Stetson SW. 2009. Estimating Urban Canopy Parameters Using Synthetic Aperture Radar Data. *Journal of Applied Meteorology and Climatology* **49**: 732-747

Jia L, Su Z, van den Hurk B, Menenti M, Moene AF, de Bruin HAR, Baselga Yrisarry JJ, Ibanez M, Cuesta A. 2003. Estimation of sensible heat flux using the Surface Energy Balance System (SEBS) and ATSR measurements. *Physics and Chemistry of the Earth* **28**: 75–88.

Jusuf SK, Wong NH, Hagen E, Anggoro R, Hong Y. 2007. The influence of land use on the urban heat island in Singapore. *Habitat International* **31**: 232–242.

Kaimal JC, Gaynor JE. 1991. Another look at sonic thermometry. *Boundary-Layer Meteorology* **56**: 401–410.

Kanda M, Kanega M, Kawai T, Moriwaki R, Sugawara H. 2007. Roughness lengths for momentum and heat derived from outdoor urban scale models. *Journal of Applied Meteorology and Climatology* **46**: 1067−1079.

Kanda M, Moriwaki R, Kasamatsu F. 2006. Spatial variability of both turbulent fluxes and temperature profiles in an urban roughness layer. *Boundary-Layer Meteorology* **121**: 339–350.

Kanda M, Moriwaki R, Kimoto Y. 2005. Temperature profiles within and above an urban canopy. *Boundary-Layer Meteorology* **115**: 499–506.

Kato S, Yamaguchi Y. 2007. Estimation of storage heat flux in an urban area using ASTER data. *Remote Sensing of Environment* **110**: 1–17.

Kaufman YJ, Tanré D, Remer LA, Vermote EF, Chu A, Holben BN. 1997. Operational remote sensing of tropospheric aerosol over land from EOS moderate resolution imaging spectro-radiometer. *Journal of Geophysical Research* **102**: 17 051–17 068.

Keller J, Bojinski S, Prevot ASH. 2007. Simultaneous retrieval of aerosol and surface optical properties using data of the Multi-angle Imaging SpectroRadiometer (MISR). *Remote Sensing of Environment* **107**: 120–137.

Kondo A, Ueno M, Kaga A, Yamaguchi K. 2001. The influence of urban canopy configuration on urban albedo. *Boundary-Layer Meteorology*, **100**: 225–242.

Kormann R, Meixner FX. 2001. An analytic footprint model for neutral stratification. *Boundary-Layer Meteorology* **99**: 207–224.

Kustas WP, Choudhury BJ, Moran MS, Reginato RJ, Jackson RD, Gay LW, Weaver HL. 1989. Determination of sensible heat flux over sparse canopy using thermal infrared data. *Agricultural and Forest Meteorology* **44**: 197–216.

Kustas WP, Daughtry CST. 1990: Estimation of the soil heat flux/net radiation from spectral data. *Agricultural and Forest Meteorology* **49**: 405-223.

Kustas WP, Li F, Jackson TJ, Prueger JH, MacPherson JI, Wolde M. 2004. Effects of remote sensing pixel resolution on modeled energy flux variability of croplands in Iowa. *Remote Sensing of Environment* **92**: 535–547.

Li F, Kustas WP, Anderson MC, Prueger JH, Scott RL. 2008. Effect of remote sensing spatial resolution on interpreting tower-based flux observations. *Remote Sensing of Environment* **112**: 337–349.

Liang S. 2000. Narrowband to broadband conversions of land surface albedo. I Algorithms. *Remote Sensing of Environment* **76**: 213–238.

Liang S. 2004. *Quantitative Remote Sensing of Land Surfaces*. Wiley Series in Remote Sensing.-(Series Editor): Jin Au Kong. Hoboken, New Jersey: 534

Liu BYH, Jordan RC. 1963. The long-term average performance of flatplate solar energy collectors. *Solar Energy*, **7**: 53.

Liu G, Sun J, Jiang W. 2008. Observational verification of urban surface roughness parameters derived from morphological models. *Meteorological Applications* **16**: 205–213.

Liu S, Lu L, Mao D, Jia L, 2007. Evaluating parameterizations of aerodynamic resistance to heat transfer using field measurements. *Hydrology and Earth System Science* **11**: 769-783.

Livada I, Santamouris M, Niachou K, Papanikolaou N, Mihalakakou G. 2002. Determination of places in the great Athens area where the heat island effect is observed. *Theoretical and Applied Climatology* **71**: 219–230.

Macdonald RW, Griffiths RF, Hall DJ. 1998. An improved method for the estimation of surface roughness of obstacle arrays. *Atmospheric Environment* **32**: 1857–1864.

Mahmoud KF, Alfaro SC, Favez O, Abdel Wahab MM, Sciare J. 2008. Origin of black carbon concentration peaks in Cairo (Egypt). *Atmospheric Research* **89**: 161–169.

Malek E, Bingham GE. 1997. Partitioning of radiation and energy balance components in an inhomogeneous desert valley. *Journal of Arid Environments* **37**: 193–207.

Martonchik JV, Diner DJ, Kahn RA, Ackerman TP, Verstraete MM, Pinty B, Gordon HR. 1998. Techniques for the retrieval of aerosol properties over land and ocean using multiangle imaging. *IEEE Transactions on Geoscience and Remote Sensing* **36**: 1212–1227.

Massman WJ, Lee X. 2002. Eddy covariance flux corrections and uncertainties in long-term studies of carbon and energy exchanges. *Agricultural and Forest Meteorology* **113**: 121–144.

Maxwell EL. 1987. A quasi-physical model for converting hourly global horizontal to direct normal insolation. *SERI (Solar Energy Research Institute). Colorado.*

Meister G, Lucht W, Rothkirch A, Spitzer H. 1999. Large Scale Multispectral BRDF of an Urban Area. *IEEE International Geoscience and Remote Sensing Symposium, IGARSS'99, Hamburg* **2**: 821– 823.

Meister, G., Rothkirch, A., Wiemker, R., Bienlein, J., Spitzer, H. 1998. Modeling the directional reflectance (BRDF) of a corrugated roof and experimental verification. IEEE International Geoscience and Remote Sensing Symposium, *IGARSS'98, Seattle* **3**: 1487–1489.

Meister, G., Wiemker, R., Bienlein, J., Spitzer, H. 1996. In Situ BRDF Measurements of Selected Surface Materials to Improve Analysis of Remotely Sensed Multispectral Imagery. *Proceedings of the XVIII. Congress of the International Society for Photogrammetry and Remote Sensing ISPRS 1996, Vienna*: 493–498.

Menenti M, Choudhury BJ. 1993. Parameterization of land surface evaporation using a location dependent potential evaporation and surface temperature range. In: H.J. Bolle *et al. Exchange Processes at the Land Surface for a Range of Space and Time Scales. IAHS Publication* **21:** 561–568.

Moderow U, Aubinet M, Feigenwinter C, Kolle O, Lindroth A, Mölder M, Montagnani L, Rebmann C, Bernhofer C. 2009. Available energy and energy balance closure at four coniferous forest sites across Europe. *Theoretical and Applied Climatology* **98**: 397–412.

Monteith JL, Unsworth MH. 1990. Principles of environmental physics, 2nd ed. Edward Arnold, London, United Kingdom.

Moore CJ. 1986. Frequency response corrections for eddy correlation systems. *Boundary-Layer Meteorology* **37**: 17–35.

Moriwaki R, Kanda M, Nitta H. 2006. Carbon dioxide build-up within a suburban canopy layer in winter night. *Atmospheric Environment* **40**: 1394-1407.

Moriwaki R, Kanda M. 2004. Seasonal and diurnal fluxes of radiation, heat, water vapor, and carbon dioxide over a suburban area. *Journal of Applied Meteorology* **43**: 1700–1710.

Mortensen NG, Hansen JC, Badger J, Jørgensen BH, Hasager CB, Paulsen US, Hansen OF, Enevoldsen K, Youssef LG, Said US, El-Salam Moussa AA, Mahmoud MA, El Sayed Yousef A, Awas AM, Abd-El Raheem Ahmed M, Sayed MAM, Korany MH, Abd-El Baky Tarad M. 2006. Wind atlas for Egypt: Measurements, micro- and mesoscale modelling. *Proceedings of the 2006 European Wind Energy Conference and Exhibition, Athens, Greece:* 10.

NASA. 2007a. Jet Propulsion Laboratory, California Institute of Technology, ASTER Surface Reflectance/ Radiance VNIR/SWIR Product http://asterweb.jpl.nasa.gov/content/03_data/01_Data_Products/release_aster_surface_reflectance.htm
Cited 15 June 2007

NASA. 2007b. Landsat 7 Science Data Users Handbook
http://landsathandbook.gsfc.nasa.gov/handbook.html.
Cited 15 Jun 2007

Neftel A, Spirig C, Ammann C. 2008. Application and test of a simple tool for operational footprint evaluations. *Environmental Pollution* **152**: 644–652.

Nemitz E, Hargreaves KJ, McDonald AG, Dorsey JR, Fowler D. 2002. Micrometeorological measurements of the urban heat budget and CO_2 emissions on a city scale. *Environmental Science & Technology* **36**: 3139–3146.

Nicodemus F. 1970. Reflectance nomenclature and directional reflectance and emissivity. *Applied Optics* **4**: 767–773.

Norman JM, Becker F. 1995. Terminology in thermal infrared remote sensing of natural surfaces. *Agricultural and Forest Meteorology* **77**: 153–166.

Norman JM, Kustas WP, Humes KS. 1995. Source approach for estimating soil and vegetation energy fluxes in observations of directional radiometric surface temperatures. *Agricultural and Forest Meteorology* **77(3–4)**: 263–293. (Erratum: *Agricultural and Forest Meteorology* **80(2–4)**: 297.

Ochsner TE, Sauer TJ, Horton R. 2007. Soil heat storage measurements in energy balance studies. *Agronomy Journal* **99**: 311–319.

Offerle B, Jonsson P, Eliasson I, GRIMMOND CSB. 2005. Urban modification of the surface energy balance in the west African Sahel: Ouagadougou, Burkina Faso. *Journal of Climate* **18**: 3983–3995.

Offerle BD. 2003. The energy balance of an urban area: examining temporal and spatial variability through measurements, remote sensing and modelling, *PhD*, Indiana University, Bloomington USA.

Ogawa K, Schmugge T, Jacob F, French A. 2002. Estimation of broadband emissivity from satellite multi-channel thermal infrared data using spectral libraries. *Proc. IGARSS Toronto, ON, Canada* **6**: 3234–3236.

Oke TR, Spronken-Smith RA, Jauregui E, Grimmond CSB. 1999. The energy balance of central Mexico City during the dry season. *Atmospheric Environment* **33**: 3919–3930.

Oke TR. 2007. Siting and exposure of meteorological instruments at urban sites. In *Air Pollution Modeling and its Application XVII*, Borrego C, Norman A-L (eds). Springer: New York, USA: 615–632.

Oncley SP, Foken T, Vogt R, Kohsiek W, de Bruin H, Bernhofer C, Christen A, Grantz D, Lehner E, Liebethal C, Liu HP, Mauder M, Pitacco A, Ribeiro L, Weidinger T. 2007. The energy balance experiment EBEX-2000. Part I: overview and energy balance. *Boundary-Layer Meteorology* **123**: 1–28.

Parlow E. 1996. Correction of terrain controlled illumination effects in satellite data. In: Parlow E. (ed) *Progress in Environmental Research and Applications*, Balkema Publishers, Rotterdam: 139–145

Parlow E. 1998. Net radiation of urban areas. In: Gudmandsen, P. (ed) *Future trends in remote sensing*. Balkema Publishers, Rotterdam: 221–226

Parlow E. 2007. Stadtklima. Gebhardt H, Glaser R, Radtke U, Reuber P (eds) *Geographie. Physische Geographie und Humangeographie*. Elsevier Publishers: München: 56–60.

Pasquill F, Smith FB. 1983: Atmospheric Diffusion. 3rd edn. Wiley, New York, 437.

Philip JR. 1961. The theory of heat flux meters. *Journal of Geophysical Research* **66**: 571–579.

Potchter O, Goldman D, Kadish D, Iluz D. 2008. The oasis effect in an extremely hot and arid climate: The case of southern Israel. *Journal of Arid Environments* **72**: 1721–1733.

Prigent C, Tegen I, Aires F, Marticorena B, Zribi M. 2005. Estimation of the aerodynamic roughness length in arid and semi-arid regions over the globe with the ERS scatterometer. *Journal of Geophysical Research* **110(D09205)**: 1–12.

Prihodko L, Goward SN. 1997. Estimation of Air Temperature from Remotely Sensed Surface Oberservations. *Remote Sensing of the Environment* **60**: 335–346.

Qi J, Chehbouni A, Huete AR, Kerr YH, Sorooshian S. 1994. A modified soil adjusted vegetation index. *Remote Sensing of Environment* **48(2)**: 119–126.

Raga GB, Castro T, Baumgardner D. 2001. The impact of megacity pollution on local climate and implications for the regional environment: Mexico City. *Atmospheric Environment* **35(10)**: 1805-1811.

Rashed T, Weeks JR, Saad Gadalla M, Hill AG. 2001. Revealing the Anatomy of Cities through Spectral Mixture Analysis of Multispectral Satellite Imagery: A Case Study of the Greater Cairo Region, Egypt. *Geocarto International* **16**: 7–18.

Ratti C, Di Sabatino S, Britter R, Brown M, Caton F, Burian S. 2002. Analysis of 3-D Urban Databases with Respect to Pollution Dispersion for a Number of European and American Cities. *Water, Air and Soil Pollution: Focus* **2(5-6)**: 459-469.

Raupach MR. 1994. Simplified expressions for vegetation roughness length and zero-plane displacement as functions of canopy height and area index. *Boundary Layer Meteorology* **71**: 211–216.

Raupach MR. 1995. Corrigenda. *Boundary Layer Meteorology* **76**: 303–304.

Remer LA, Kaufman YJ, Tanré D, Mattoo S, Chu DA, Martins JV, Li R-R, Ichoku C, Levy RC, Kleidman RG, Eck TF, Vermote E, Holben BN. 2005. The MODIS Aerosol Algorithm, Products, and Validation. *Journal of the Atmospheric Sciences* **62**: 947–973.

Rigo G, Parlow E, Oesch D. 2006. Validation of satellite observed thermal emission with in-situ measurements over an urban surface. *Remote Sensing of Environment* **104**: 201–210.

Rigo G, Parlow E. 2007. Modelling the ground heat flux of an urban area using remote sensing data. *Theoretical and Applied Climatology* **90**: 185–199.

Rigo G, Parlow E. 2006. Modelling the ground heatflux of an urban area with remote sensing data. *Theoretical and Applied Climatology* **90(3–4)**: 185–199.

Rigo G. 2007. Satellite analysis of radiation and heat fluxes during the Basel Urban Boundary Layer Experiment (BUBBLE). *PhD*. University of Basel, Switzerland

Robaa SM. 2003. Urban-suburban/rural differences over Greater Cairo, Egypt. *Atmosfera* **16**: 157–171.

Robaa SM. 2009. Urban-rural solar radiation loss in the atmosphere of Greater Cairo region, Egypt. *Energy Conversion and Management* **50**: 194–202.

Robaa SM. 2000. Giza monuments and local climate change. *ICEHM2000, September 2000, Cairo University, Egypt*: 187-200.

Roerink GJ, Su z, Menenti M. 2000. S-SEBI: A simple remote sensing algorithm to estimate the surface energy balance. *Physics and Chemistry of the Earth, Part B: Hydrology, Oceans and Atmosphere* **25(2)**: 147–157.

Roerink GJ, Su Z, Menenti M. 2000. S-SEBI: a simple remote sensing algorithm to estimate the surface energy balance. *Physics and Chemistry of the Earth (B)* **25**: 147–157.

Rotach MW, Vogt R, Bernhofer C, Batchvarova E, Christen A, Clappier A, Feddersen B, Gryning S-E, Martucci G, Mayer H, Mitev V, Oke TR, Parlow E, Richner H, Roth M, Roulet YA, Ruffieux D, Salmond J, Schatzmann M, Voogt JA. 2005. BUBBLE-an urban boundary layer meteorology project. *Theoretical and Applied Climatology* **81**: 231–261.

Sailor DJ. 2010. A review of methods for estimating anthropogenic heat and moisture emissions in the urban environment. *International Journal of Climatology*. Published online. 11.

Sailor DJ, Fan H. 2002. Modeling the diurnal variability of effective albedo for cities. *Atmospheric Environment* **36**: 713–725.

Sailor DJ. 1995. Simulated urban response to modifications in surface albedo and vegetative cover. *Journal of Applied Meteorology* **34**: 1694–1704.

Sauer TJ, Meek DW, Ochsner TE, Harris AR, Horton R. 2003. Errors in heat flux measurement by flux plates of contrasting design and thermal conductivity. *Vadose Zone Journal* **2**: 580–588.

Schaepman-Strub G, Schaepman ME, Painter TH, Dangel S, Martonchick JV. Reflectance quantities in optical remote sensing-definitions and case studies. *Remote Sensing of Environment* **103**: 27–42.

Schaudt KJ, Dickinson RE. 2000. An approach to deriving roughness length and zero-plane displacement height from satellite data, prototyped with BOREAS data. *Agricultural and Forest Meteorology* **104**: 143–155.

Schiefer S, Damm A, Hostert, P. 2006: Correcting brightness gradients in hyperspectral data from urban areas. *Remote Sensing of Environment* **101**, 25–37.

Schläpfer D, Odermatt D. 2006. MODO User Manual, Version 3. Wil (SG), Switzerland.

Schlink U, Rehwagen M, Richter M, Herbarth O. 2007. Environmental security in urban areas. Health-relevant VOC exposure in the Greater Cairo Area, Egypt. In: Linkov I, Wenning RJ, Kiker GA (eds.), Managing critical infrastructure risks: decision tools and applications for port security. Springer, Dordrecht: 423–434.

Schotanus P, Nieuwstadt FTM, De Bruin HAR. 1983. Temperature measurement with a sonic anemometer and its application to heat and moisture fluxes. *Boundary-Layer Meteorology* **26**: 81-94.

Schwander H, Mayer B, Ruggaber A, Albold A, Seckmeyer G, Koepke P. 1999. Method to determine snow albedo values in the ultraviolet for radiative transfer modelling. *Applied Optics* **38**, 3869–3875.

Shaltout MA, Hassan AH, Fathy AM. 2001. Total suspended particles and solar radiation over Cairo and Aswan. *Renewable Energy* **23**: 605–619.

Shaltout MAM, Tadros MTY, El-Metwally M. 2000. Studying the extinction coefficient due to aerosol particles at different spectral bands in some regions at great Cairo. *Renewable Energy* **19**: 597–615.

Small C. 2005. A global analysis of urban reflectance. *International Journal of Remote Sensing* **26**: 661–681.

Sobrino JA, Gómes M, Jiménez-Muñoz JC, Olioso A, Chehbouni G. 2005. A simple algorithm to estimate evapotranspiration from DAIS data: Application to the DAISEX campaigns. *Journal of Hydrology* **315(1–4)**: 117–125.

Sobrino JA, Jiménez-Muñoz JC, Balick L, Gillespie AR, Sabol DA, Gustafson WT. 2007. Accuracy of ASTER level-2 thermal-infrared standard products of an agricultural area in Spain. *Remote Sensing of Environment* **106**: 146–153.

Sobrino JA, Jiménez-Muñoz JC, Paolini L. 2004. Land surface temperature retrieval from LANDSAT TM 5. *Remote Sensing of Environment* **90**: 434–440.

Soegaard H, Møller-Jensen L. 2003. Towards a spatial CO_2 budget of a metropolitan region based on textural image classification and flux measurements. *Remote Sensing of Environment* **87**: 283-294.

Sofer M, Potchter O. 2006. The urban heat island of a city in an arid zone: the case of Eilat, Israel. *Theoretical and Applied Climatology* **85**: 81–88.

Soler MR, Ruiz C. 1994. Urban albedo derived from direct measurements and Landsat 4 TM satellite data. *International Journal of Climatology* **14**: 925–931.

Spank U, Bernhofer C. 2008. Another simple method of spectral correction to obtain robust eddy-covariance results. *Boundary-Layer Meteorology* **128**: 403–422.

Spronken-Smith RA. 2002. Comparison of summer- and winter-time suburban energy fluxes in Christchurch, New Zealand. *International Journal of Climatology* **22**: 979–992.

Stathopoulou M, Cartalis C. 2007. Daytime urban heat islands from Landsat ETM+ and Corine land cover data: an application to major cities in Greece. *Solar Energy* **81**: 358–368.

Stathopoulou M, Synnefa A, Cartalis C, Santamouris M, Karlessi T, Akbari H. 2009. A surface heat island study of Athens using high-resolution satellite imagery and measurements of the optical and thermal properties of commonly used building and paving materials. *International Journal of Sustainable Energy* **28**: 59–76.

Streutker DR. 2003. Satellite-measured growth of the urban heat island of Houston, Texas. *Remote Sensing of Environment* **85**: 282–289.

Su Z. 2002. The surface energy balance system (SEBS) for estimation of turbulent heat fluxes. *Hydrology and Earth System Sciences* **6(1)**: 85–99.

Sutton K, Fahmi W. 2001. Cairo's urban growth and strategic master plans in the light of Egypt's 1996 population census results. *Cities* **18**: 135–149.

Taha H. 1997. Urban climates and heat islands: albedo, evapotranspiration, and anthropogenic heat. *Energy and Buildings* **25**: 99–103.

Trabea AA, Shaltout MAM. 2000. Correlation of global solar radiation with meteorological parameters over Egypt. *Renewable Energy* **21**: 297–308.

Tran H, Uchihama D, Ochi S, Yasuoka Y. 2006. Assessment with satellite data of the urban heat island effects in Asia mega cities. *International Journal of Applied Earth Observation and Geoinformation* **8(1)**: 34-48.

Tsoar H. 1990. The ecological background, deterioration and reclamation of desert dune sand. *Agriculture, Ecosystems and Environment* **33**: 147–170.

Twine TE, Kustas WP, Norman JM, Cook DR, Houser PR, Meyers TP, Prueger JH, Starks PJ, Wesely ML. 2000. Correcting eddy-covariance flux underestimates over a grassland. *Agricultural and Forest Meteorology* **103**: 279–300.

Van Dijk A, Kohsiek W, de Bruin HAR. 2003. Oxygen sensitivity of krypton and Lyman-a hygrometers. *Journal of Atmospheric and Oceanic Technology* **20**: 143–151.

van Ulden AP. 1978. Simple estimates for vertical diffusion from sources near the ground. *Atmospheric Environment* **12**: 2125–2129.

Velasco E, Pressley S, Allwine E, Westberg H, Lamb B. 2005. Measurements of CO_2 fluxes from the Mexico City urban landscape. *Atmospheric Environment* **39**: 7433-7446.

Verma SB. 1989. Aerodynamic resistances to transfers of heat, mass and momentum. Estimation of Areal Evapotranspiration. - Black TA, Spittlehouse DL, Novak MD, Price DT (Eds.), *International Association of Hydrological Sciences* **177**: 13–20.

Vesala T, Järvi L, Launiainen S, Sogachev A, Rannik Ü, Mammarella I, Siivola E, Keronen P, Rinne J, Riikonen A, Nikinmaa E. 2008b. Surface-atmosphere interactions over complex urban terrain in Helsinki, Finland. *Tellus*, **60B**: 188-199.

Vesala T, Kljun N, Rannik Ü, Rinne J, Sogachev A, Markkanen T, Sabelfeld K, Foken T, Leclerc MY. 2008a. Flux and concentration footprint modelling: State of the art. *Environmental Pollution* **152**: 653-666.

Vogt R, Christen A, Rotach MW, Roth M, Satyanarayana ANV. 2006. Temporal dynamics of CO_2 fluxes and profiles over a central European city. *Theoretical and Applied Climatology* **84**: 117-126.

Voogt JA, Grimmond CSB. 2000. Modelling surface sensible heat flux using surface radiative temperatures in a simple urban area. *Journal of Applied Meteorology* **39**, 1679–1699.

Voogt JA, Oke TR. 2003. Thermal remote sensing of urban areas. *Remote Sensing of Environment* **86**: 370–384.

Wang J, White K, Robinson GJ. 2000. Estimating surface net solar radiation by use of Landsat-5 TM and digital elevation models. *International Journal of Remote Sensing* **21**: 31 – 43.

Webb EK, Pearman GI, Leuning R. 1980. Correction of flux measurements for density effects due to heat and water vapour transfer. *Quarterly Journal of Royal Meteorological Society* **106**: 85–100.

Weeks JR, Larson D, Fugate D. 2005. Patterns of land use as assessed by satellite imagery: an application to Cairo, Egypt. In Entwisle B, Rindfuss R, Stern P (eds). *Population, Land Use, Environment: Research Directions*, National Academy Press: Washington, DC.

Wilson K, Goldstein A, Falge E, Aubinet M, Baldocchi D, Berbigier P, Bernhofer C, Ceulemanns R, Dolman H, Field C, Grelle A, Ibrom A, Law BE, Kowalski A, Meyers T, Moncrieff J, Monson R, Oechel W, Tenhunen J, Valentini R, Verma S. 2002. Energy balance closure at FLUXNET sites. *Agricultural and Forest Meteorology* **113(1–4)**: 223–243.

Xu W, Wooster MJ, Grimmond CSB. 2008. Modelling of urban sensible heat flux at multiple scales: a demonstration using airborne hyperspectral imagery of Shanghai and a temperature- emissivity separation approach. *Remote Sensing of Environment* **112**: 3493–3510.

Zakey AS, Abdel-Wahab MM, Pettersson JBC, Hatari MJ, Hallquist M. 2008. Seasonal and spatial variation of atmospheric particulate matter in a developing megacity, the Greater Cairo, Egypt. *Atmósfera* **21**: 171–189.